

# A Scalable Quantum Neural Network for Approximate SRBB-Based Unitary Synthesis

Giacomo Belli, Marco Mordacci and Michele Amoretti

Quantum Software Laboratory, Department of Engineering and Architecture, University of Parma, 43124 Parma, Italy

November 2024

## Abstract

In this work, scalable quantum neural networks are introduced to approximate unitary evolutions through the *Standard Recursive Block Basis* (SRBB) and, subsequently, redesigned with a reduced number of CNOTs. This algebraic approach to the problem of unitary synthesis exploits Lie algebras and their topological features to obtain scalable parameterizations of unitary operators. First, the recursive algorithm that builds the SRBB is presented, framed in the original scalability scheme already known to the literature only from a theoretical point of view. Unexpectedly, 2-qubit systems emerge as a special case outside this scheme. Furthermore, an algorithm to reduce the number of CNOTs is proposed, thus deriving a new implementable scaling scheme that requires one single layer of approximation. From the mathematical algorithm, the scalable CNOT-reduced quantum neural network is implemented and its performance is assessed with a variety of different unitary matrices, both sparse and dense, up to 6 qubits via the PennyLane library. The effectiveness of the approximation is measured with different metrics in relation to two optimizers: a gradient-based method and the Nelder-Mead method. The approximate SRBB-based synthesis algorithm with CNOT-reduction is also tested on real hardware and compared with other valid approximation and decomposition methods available in the literature.

## Contents

<b>1</b>	<b>Introduction</b>	<b>2</b>
<b>2</b>	<b>Unitary approximation via SRBB: the algebraic structure and its properties</b>	<b>4</b>
2.1	Recursive construction and implementation of matrix algebras . . . . .	5
<b>3</b>	<b>Quantum circuit to approximate 2-qubit systems</b>	<b>7</b>
3.1	The permutation group and ZYZ-decompositions . . . . .	9
3.1.1	CNOT sequences . . . . .	10
3.1.2	Properties under permutation . . . . .	10
3.2	Diagonal contributions . . . . .	11
3.3	Even contributions . . . . .	13
3.4	Odd contributions . . . . .	14
3.5	2-qubit circuit to approximate $SU(4)$ . . . . .	15
<b>4</b>	<b>Quantum circuit to approximate 3-qubit systems</b>	<b>16</b>
4.1	Diagonal contributions . . . . .	18
4.2	Even contributions . . . . .	18
4.3	Odd contributions . . . . .	21
4.4	3-qubit circuit to approximate $SU(8)$ . . . . .	22
<b>5</b>	<b>Quantum circuit to approximate 4-qubit systems</b>	<b>23</b>
5.1	Diagonal contributions . . . . .	26
5.2	Even contributions . . . . .	27
5.3	Odd contributions . . . . .	30
5.4	4-qubit circuit to approximate $SU(16)$ . . . . .	32

arXiv:2412.03083v1 [quant-ph] 4 Dec 2024

<b>6</b>	<b>A scalable algorithm for optimizing CNOT-gates in the SRBB-based synthesis framework</b>	<b>33</b>
6.1	Simplifying CNOTs between diagonal contributions . . . . .	34
6.1.1	Gray-Code-based solution . . . . .	37
6.1.2	Solution for $n = 4$ . . . . .	40
6.2	Simplifying CNOTs between even/odd contributions . . . . .	41
6.2.1	Solution for $n = 4$ . . . . .	43
6.3	CNOT-reduced quantum circuit to approximate SU operators with SRBB-decomposition . . . . .	48
6.3.1	Proof of gate count formulas . . . . .	48
6.3.2	Anomaly for $n = 2$ . . . . .	51
<b>7</b>	<b>Implementation and Results</b>	<b>52</b>
7.1	Tests with Quantum Circuit Simulation . . . . .	53
7.2	Tests on Real Quantum Devices . . . . .	56
7.3	Insights on loss functions . . . . .	58
<b>8</b>	<b>Conclusions</b>	<b>59</b>
<b>A</b>	<b>Tested Circuits</b>	<b>62</b>
A.1	List of tested circuits for $n = 2$ . . . . .	62
A.2	List of tested circuits for $n = 3$ . . . . .	63
A.3	List of tested circuits for $n = 4$ . . . . .	64
A.4	List of tested circuits for $n = 5, 6$ . . . . .	65
<b>B</b>	<b>Example of resulting matrices</b>	<b>65</b>
B.1	QFT2 . . . . .	65
B.2	Frobenius loss random matrix . . . . .	65
B.3	Fidelity loss random matrix . . . . .	66
B.4	Trace distance random matrix . . . . .	66

# 1 Introduction

The development of variational quantum algorithms has been driven by the advancements in quantum machine learning (QML), which aims to leverage quantum computing to enhance machine learning outcomes in terms of performance and training efficiency [1, 2, 3]. Central to QML is the concept of Quantum Neural Network (QNN), a hybrid quantum-classical algorithm that consists of three key components: a quantum encoding circuit, a variational quantum circuit (VQC) [4] and an optimization process. The quantum encoding circuit encodes the classical data  $x$  into a quantum state, a task that can be addressed through different methods like basis encoding, amplitude encoding, or angle encoding [1]. The VQC is characterized by a set of parameters  $\theta_i$  (rotation angles) that must be trained to minimize a classical loss function. Lastly, the optimization process consists of using classical gradient descent to update the parameters  $\theta_i$ .

Since quantum information evolves according to unitary operators, it is clear why the parametric representation of dense unitary matrices and the relative decomposition into primitive gate sets of near-term quantum devices, has aroused such great interest among mathematicians, physicists and computer scientists [5, 6, 7, 8, 9, 10]. Designing quantum circuits for unitary evolutions on a multi-qubit system and identifying suitable approximations for a given unitary is known as gate synthesis [11, 12, 13, 14, 15, 16], for which some techniques such as Recursive CS Decomposition [17] and Quantum Shannon Decomposition [18] are well known. The existence of such a construction is validated by the Solovay-Kitaev algorithm [19], the first example of approximate unitary synthesis with only CNOTs and one-qubit (rotation) gates, which represent a universal model for quantum computation [20]. Optimizations of this algorithm followed [21, 22] and then a whole new class of efficient approximate synthesis algorithms based on Number Theory with  $O(\log(1/\epsilon))$  gates opened a new line of research [23, 24, 25, 26, 27].

A few years ago, an approach to gate synthesis based on optimization methods garnered significant interest in approximating a matrix according to a metric criterion and a set of constraints [28, 29]. Along this line of research, and similarly to unitary approximation methods based on Lie geometries [30, 31], an approach to approximate synthesis based on Lie algebras and classical optimization techniques on unitary parameterizations was recently proposed [32]. This new algorithm introduces a Hermitian unitary basis for the  $\mathbb{C}^{2^n \times 2^n}$  algebra, called the *Standard Recursive Block Basis* (SRBB), so as to obtain a scalable parameterized representation for

any unitary operator via a recursive procedure (advantageous compared to the Pauli string basis). The algebraic representation is the core of an approximate gate synthesis algorithm for which a quantum neural network *framework* is applicable and, even better, is able to leverage the topological features of unitary groups in performing the approximation task. Nevertheless, the approximation procedure is not addressed in a pure quantum way, without working with the VQC that represents the QNN and using classical optimization techniques (a hard problem for classical computers). Furthermore, the quantum circuit theoretically proposed in [32] requires several approximation layers for dense matrices and, since the number of gates grows exponentially with the number of qubits  $n$ , its implementation would be quite complicated. Based on the algebraic properties of this new basis, the authors proposed a specific ordering of the algebraic elements in the definition of the approximating matrix such as to minimize the number of CNOTs. However, although a general scaling scheme for circuit construction was provided, these simplifications were not incorporated into a scalable quantum scheme.

This work provides the following contributions.

1. A revised version of the recursive matrix algorithm that builds the SRBB [33] for any  $n$  is provided. Such a revision came out from our effort while implementing a Python library<sup>1</sup> for studying, verifying and manipulating this new type of unitary algebra. The library contains all kinds of useful functions to check all the algebraic properties fundamental for the success of the approximation, like the number and position of diagonal basis elements, hermiticity and grouping properties. Indeed, these mathematical properties concern not only the individual elements of the algebraic bases, but also their sub-groupings and their orderings in the intermediate stages of the approximation algorithm, which is summarized in Section 2. In particular, section 2.1 rigorously defines the SRBB and outlines in detail the steps of its implementation, very useful for handling and manipulating SRBB-type algebras as its elements grow exponentially. The approximation algorithm [33] works only with special unitary operators without losing generality, thanks to the surjective relation that exists between the special unitary group  $SU(2^n)$  and the unitary group  $U(2^n)$ . From Group Theory, it is known that every unitary matrix  $U(d)$  is associated to a set of  $d = 2^n$  special unitary matrices through a phase rescaling, where the phases correspond precisely to the complex roots of  $\det(U)$ . This property implies a certain degree of ambiguity, more precisely a multiplicity of  $d$  solutions, in machine learning approximation processes based on losses defined by density matrices. In fact, by their definition, these losses make use of the square moduli of the amplitudes of the quantum states, canceling the information present in the phases. In Section 2, this topic is presented from a formal point of view, justifying the exclusive consideration of special unitary matrices and deriving a recipe to solve the phase ambiguity problem in the approximation process; its implementation is instead described in Section 7.
2. It is proved that the particular case  $n = 2$  is outside the original scalability scheme proposed in the literature [33] due to its peculiar algebraic properties. It is important to emphasize that the original scaling scheme concerns the ordering and grouping of SRBB elements, without involving the theoretically proposed simplification of CNOTs. 2-qubit systems are described and analyzed in depth step by step in Section 3, through a new reformulation enriched with all the mathematical aspects relevant for the design of the approximating VQC and some useful shortcuts. Furthermore, this simpler reformulation clarifies some typos found in [33].
3. The application of the algorithm to the specific cases for  $n = 3, 4$  is treated in Sections 4 and 5, respectively, following the synopsis of the new reformulation. These concrete examples were never treated in literature before and, in light of the scalable algorithm for CNOT-simplifications proposed in this paper, they show how the simplifications occur and the final scalable features of the simplified circuit. Finally, they represent concrete case studies to handle the increasing complexity of the algebraic basis, in terms of both cardinality and matrix order, exploiting the shortcuts and the scalable algebraic properties of the algorithm.
4. A new scalable algorithm capable of reducing the total number of CNOT gates within the original structure of the approximating VQC is found and described in Section 6. As anticipated in the anomalous case of 2-qubit systems, the  $n = 3$  case is the first for which the simplification algorithm is applicable. This algorithm is perfectly compatible with the original grouping proposed in the literature [33] and, in general, represents a solid starting point to reduce the depth of the associated QNN for approximate synthesis maintaining the scalability property.
5. Starting from the discovered mathematical algorithm, the implementation of a new scalable CNOT-reduced QNN that requires only one single layer of approximation is described in Section 7. Its performance is assessed with a variety of different unitary operators, both sparse and dense, up to 6 qubits via the

---

<sup>1</sup>The library will be made public and shared via Git as soon as possible.

PennyLane library. The QNN is optimized using different loss functions like the Frobenius norm (originally used in [33]), the fidelity and the trace distance, with respect to two different optimizers, a gradient-based method and the Nelder-Mead method (originally used in [33]). Furthermore, to assess the performance, a test set of 500 random quantum states is used to observe the distance (computed through the trace distance) between the state provided by the ideal matrix and the one produced by the approximated matrix. The tests show novel and better results when sparse matrices are used. In particular, when the Nelder-Mead optimizer is used, the network achieves better approximations in less time than the state of the art. Conversely, when the Adam optimizer is employed, the QNN can achieve a coarse approximation (e.g. around  $10^{-3}$  with 2 qubits,  $10^{-2}$  with 3 and 4 qubits, and  $10^{-1}$  with 5 and 6 qubits) in less time than what is achieved with the Nelder-Mead method. Therefore, Adam allows for faster approximations even in configurations that cannot be approximated when using the Nelder-Mead method due to time constraints. Furthermore, novel results with dense random matrices are achieved with just a single layer of the algorithm.

6. The SRBB-based CNOT-reduced approximation algorithm is also tested on real IBM hardware to assess the network usability with 2 qubits and, in this case, the Hellinger distance is computed to compare the ideal probability distribution with the one produced by the network.

The remainder of the paper is organized as follows. In Section 2, the Standard Recursive Block Basis is introduced, providing the main mathematical objects, their formal definitions, the steps for a correct implementation given  $n$  and the approximate unitary synthesis formula. Useful mathematical details of the recursive implementation are also given. In Section 3, the 2-qubit variational quantum circuit for approximate unitary synthesis is proposed, with emphasis on why this particular case falls outside the scalability scheme. In Sections 4 and 5, the 3- and 4-qubit circuits for approximate unitary synthesis are proposed, respectively, with quick shortcuts to derive the correct quantum circuit structure; simplifications of CNOT-gates are showed but not derived in a systematic way. In Section 6, the novel scaling scheme improved with CNOT-simplifications is presented and proved, accompanied by all the diagrammatic schemes necessary to understand and implement it. In Section 7, the implementation of the scalable QNN is explained in detail as well as the testing methodology; at the same time, test results are shown. Finally, Section 8 concludes the paper with a discussion of future work.

## 2 Unitary approximation via SRBB: the algebraic structure and its properties

The *Standard Recursive Block Basis* (SRBB) is the Hermitian unitary basis for the  $\mathbb{C}^{2^n \times 2^n}$  matrix algebra, first introduced in [32] to obtain a scalable parameterized representation of unitary matrices. Accordingly, any unitary operator can be expressed as a product of exponentials of SRBB elements, thanks to the properties of the connected topological space that characterizes the Lie group  $U(2^n)$ . This algebraic basis is defined through a recursive method, starting from a very similar Hermitian unitary basis called *Recursive Block Basis* (RBB), which can be thought of as the generalization of the Pauli basis for complex matrices of higher orders<sup>2</sup>. Below, the fundamental steps of the recursive construction are retraced, so as to clarify some details of the mathematical context and introduce the algebraic objects that will play a key role in the approximate unitary synthesis algorithm and in its implementation with a reduced number of CNOTs.

### Remark 1

Since  $U(d) = U(1) \times SU(d)$ , any unitary matrix is a phase (or unitary) scaling of a special unitary matrix; this result can also be pointed out by the well-known identity:

$$\det(cA) = c^d \det(A) \quad (1)$$

with  $c \in \mathbb{C}$ ,  $A \in GL(d, \mathbb{C})$ . In fact, for any unitary matrix  $U = e^{i\alpha}V$ , where  $\det(V) = 1$ ,

$$\det(U) = \det(e^{i\alpha}V) = e^{i\alpha \cdot d} \det(V) = e^{i\alpha \cdot d} \quad (2)$$

leading the determination of the rescaling phase to the resolution of equations of degree  $d$  on the complex plane. Therefore, for any  $U \in U(d)$ , it holds that:

$$\frac{U}{[\det(U)]^{\frac{1}{d}}} \in SU(d) \quad (3)$$

---

<sup>2</sup>The SRBB differs from the RBB just for a new definition of the diagonal elements of the basis, as explained in Section 3.

This fact allows us, first of all, to work only with special unitary matrices without losing generality and, secondly, to have a precise recipe for correcting the arbitrariness in the choice of the phase that the QNN encounters in its learning process when considering loss functions based on density matrices<sup>3</sup>.

## Remark 2

It is well-known that the set of all special unitary matrices of order  $d$ , denoted by  $SU(d)$ , forms a Lie group of dimension  $d^2 - 1$  and the corresponding Lie algebra is the real vector space of all anti-Hermitian traceless matrices of order  $d$ , which is denoted by  $su(d)$ . However, in physical contexts, it is usual to choose zero-trace *Hermitian* matrices as generators, adding the imaginary unit to the surjective exponential map that constitutes the parametric representation of  $SU(d)$ . Therefore, if SRBB (or RBB) denotes a basis of the  $su(d)$  Lie algebra with elements  $U_j^{(d)}$ , the map  $\psi$  from  $\mathbb{R}^{d^2-1}$  into an open subset of  $SU(d)$  containing the identity element, is an analytic diffeomorphism which generates the entire special Lie group (Corollary 2.9, [34]):

$$\psi : (\theta_1, \dots, \theta_{d^2-1}) \in \mathbb{R}^{d^2-1} \longrightarrow \prod_{j=1}^{d^2-1} \exp\{i\theta_j U_j^{(d)}\} \in SU(d) \quad (4)$$

## 2.1 Recursive construction and implementation of matrix algebras

To implement the recursive algorithm that builds the SRBB with elements  $U_j^{(d)}$ , Corollary 2.3 of [33] is used. In order to clearly understand the algebraic manipulation and the properties of this new promising basis, some examples will be developed in detail. For this reason, it is crucial to construct the elements of the algebraic basis correctly (and in the correct *order*), following the six different building methods that depend on the position  $j$  of the matrix  $B_j^{(d)}$  in the basis<sup>4</sup>.

Starting from the Pauli basis, which describes the matrix algebra of order  $d = 2^n$  with  $n = 1$  (quantum register with a single qubit), the matrix algebras of order  $d \geq 3$  can be derived in a recursive way through the following methods:

**A)** for  $j \in \{1, 2, \dots, (d-1)^2 - 1\}$ ,

$$B_{j,A}^{(d)} = \begin{pmatrix} B_j^{(d-1)} & 0 \\ 0 & (-1)^{d-1} \end{pmatrix};$$

**B)** for  $j = (d-1)^2 + k \bmod (d-1)$ , with  $k \in \{d-1, 1, 2, \dots, d-2\}$ ,

$$B_{j,B}^{(d)} = P_{(k,d-1)} \begin{pmatrix} D & 0 \\ 0 & \sigma_1 \end{pmatrix} P_{(k,d-1)}$$

where  $P_{(k,d-1)}$  is a 2-cycle of order  $d$  and  $D = \text{diag}\{(-1)^{l-1} : 1 \leq l \leq d-2\}$ . The atypical ordering (only partially increasing) of the index  $k$  is fundamental for the correct ordering of the elements in B and C methods. The latter, in fact, depends on the permutation properties of the matrices  $P_{(k,d-1)}$  and the first element must be the one for which  $P_{k,d-1} = \mathbb{I}_d$ , i.e.  $k = d-1$ ;

**C)** for  $j = (d-1)^2 + (d-1) + k \bmod (d-1)$ , with  $k \in \{d-1, 1, 2, \dots, d-2\}$ ,

$$B_{j,C}^{(d)} = P_{(k,d-1)} \begin{pmatrix} D & 0 \\ 0 & \sigma_2 \end{pmatrix} P_{(k,d-1)};$$

**D1)** for  $j = d^2 - 1$  and  $d$  is odd,

$$B_{j,D}^{(d)} = \begin{pmatrix} \mathbb{I}_{\lfloor \frac{d}{2} \rfloor + 1} & 0 \\ 0 & -\mathbb{I}_{\lfloor \frac{d}{2} \rfloor} \end{pmatrix};$$

**D2)** for  $j = d^2 - 1$  and  $d$  is even,

$$B_{j,D}^{(d)} = \begin{pmatrix} \Sigma & 0 \\ 0 & \sigma_3 \end{pmatrix} \quad \text{with} \quad \Sigma = \begin{pmatrix} \mathbb{I}_{\lfloor \frac{d}{2} \rfloor - 1} & 0 \\ 0 & -\mathbb{I}_{\lfloor \frac{d}{2} \rfloor - 1} \end{pmatrix};$$

<sup>3</sup>This topic will be revisited again in Section 7, dedicated to implementation.

<sup>4</sup>The elements of the basis are indicated with  $B_j^{(d)}$  until the redefinition of the diagonal elements, which characterizes the transition from RBB to SRBB.

**E)** for  $j = d^2$ ,  $B_{j,E}^{(d)} = \mathbb{I}_d$ .

In Section 3, an example of this construction is shown for  $d = 3$  and  $d = 4$ . Furthermore, our Python implementation is enriched with useful functions to check the mathematical properties that ensure a correct recursive construction:

- a)  $d^2$  is the basis cardinality, where  $d = 2^n$  is the matrix order and  $n$  is the number of qubits;
- b) for  $1 \leq j \leq d^2 - 1$ ,  $\text{tr}[B_j^{(d)}] = \begin{cases} 1 & \text{if } d \text{ odd} \\ 0 & \text{if } d \text{ even} \end{cases}$  ;
- c)  $[B_j^{(d)}]^2 = \mathbb{I}_d$ ;
- d)  $\{B_j^{(d)} : 1 \leq j \leq d^2 - 1\}$  forms a basis for  $su(d)$  when  $d$  is even;
- e)  $\{B_j^{(d)} : j = m^2 - 1, 2 \leq m \leq d\} \cup \{B_{d^2}^{(d)}\}$  is the set of diagonal basis elements;
- f)  $B_{d^2}^{(d)} = \mathbb{I}_d$ .

The SRBB elements are the building blocks of a scalable approximate unitary synthesis algorithm in which their ordering, arising from their algebraic properties, and their grouping play a fundamental role. In [33], an ordering able to reduce the number of CNOTs is theoretically proposed; nevertheless, the approximate synthesis process occurs in a classical way, using optimization methods like Nelder-Mead and passing the trained parameters to the circuit only at the end, with several layers for dense matrices and without providing an implementable scalability scheme that includes CNOT-simplifications on the quantum circuit design front. Conversely, in this work the algorithm is framed into a quantum context through the scalable design of the corresponding VQC. Furthermore, a new scalability scheme that incorporates the simplifications of the CNOT gates is identified, leading to new gate-count formulas.

Given  $U \in SU(2^n)$ , the unitary synthesis algorithm can approximate  $U$  according to [33]:

$$U_{approx} \equiv \prod_{l=1}^L Z(\Theta_Z^l) \Psi(\Theta_\Psi^l) \Phi(\Theta_\Phi^l) \quad (5)$$

where  $l$  is the layer index<sup>5</sup>. The three main factors are:

$$Z(\Theta_Z^l) = \prod_{j=2}^{2^n} e^{i(\theta_{j^2-1}^l U_{j^2-1}^{(2^n)})} \quad (6)$$

$$\Psi(\Theta_\Psi^l) = \left[ \prod_{j=1}^{2^{n-1}} e^{i(\theta_{(2j-1)^2}^l U_{(2j-1)^2}^{(2^n)})} e^{i(\theta_{4j^2-2j}^l U_{4j^2-2j}^{(2^n)})} \right] \cdot \prod_{x=1}^{2^{n-1}-1} \left( \prod T_x^e \right) M_x^e \left( \prod T_x^e \right) \quad (7)$$

$$\Phi(\Theta_\Phi^l) = \prod_{x=1}^{2^{n-1}-1} \left( \prod T_x^o \right) M_x^o \left( \prod T_x^o \right) \quad (8)$$

in which

$$\prod T_x^{e/o} = \prod_{(\alpha,\beta) \in T_x^{e/o}} P_{(\alpha,\beta)} \quad (9)$$

where  $T_x^{e/o}$  are the sets of  $2^{n-2}$  disjoint transpositions obtained from the sets of permutations

$$P_{2^n}^{e/o} = \{P_{(\alpha,\beta)} \in P_{2^n} \mid \alpha \text{ even}, \beta \text{ even/odd}\} \quad (10)$$

and

$$M_x^{e/o} = \prod T_x^{e/o} \left[ \prod_{(\alpha,\beta) \in T_x^{e/o}} e^{i\theta_1 U_1} e^{i\theta_2 U_2} e^{i\theta_3 U_3} e^{i\theta_4 U_4} \right] \prod T_x^{e/o} \quad (11)$$

---

<sup>5</sup>The layer index  $l$  represents the number of times formula (5) is repeated in the construction of the VQC; our implementation requires only one single layer.

where

$$\begin{aligned} (1, 2, 3, 4)^e &= [h_\beta(\alpha - 1), f_\beta(\alpha - 1), h_{\beta-1}(\alpha), f_{\beta-1}(\alpha)] \\ (1, 2, 3, 4)^o &= [h_\beta(\alpha - 1), f_\beta(\alpha - 1), h_{\beta+1}(\alpha), f_{\beta+1}(\alpha)] \end{aligned} \quad (12)$$

with

$$\begin{aligned} f_p(q) &= (p - 1)^2 + (p - 1) + [q \bmod (p - 1)] \\ h_p(q) &= (p - 1)^2 + [q \bmod (p - 1)] \end{aligned} \quad (13)$$

The following properties are proved [33]:

- i)  $Z(\Theta_Z)$  is the product of exponentials of all diagonal SRBB elements except the last one;
- ii) in the first sub-factor of  $\Psi(\Theta_\Psi)$  enclosed by square brackets, only non-diagonal SRBB elements belonging to  $SU(2^n)$  enter with a  $ZYZ$ -decomposition;
- iii) in the second sub-factor of  $\Psi(\Theta_\Psi)$ , the factors called  $M_x^e \in SU(2^n)$  have a  $ZYZ$ -decomposition too;
- iv) inside  $\Phi(\Theta_\Phi)$ , the factors called  $M_x^o \in SU(2^n)$  are block-diagonal matrices with  $2 \times 2$  unitary blocks, whose implementation derives only in part from a  $ZYZ$ -decomposition;
- v) factors called  $\prod T_x^{e/o}$  can be implemented through CNOT sequences, being permutation matrices.

There is only one exception to this pattern, in particular to property iv (see Proposition 1): for 2-qubit systems,  $M_1^o$  admits a complete  $ZYZ$ -decomposition too, being a  $SU(2)$ -blocks diagonal unitary matrix.

In the following Sections, a detailed description of these three main factors will be provided for  $n = 2, 3, 4$ , from their mathematical definition to their circuit implementation. With reference to equation (5) with  $l = 1$ , the quantum circuit that approximates a general  $n$ -qubit special unitary operator is shown in Figure 1, in which the three main factors are illustrated only macroscopically in the correct logic order.

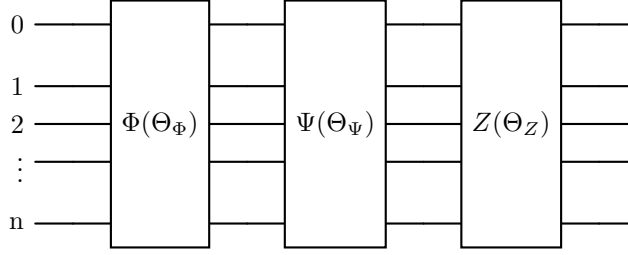


Figure 1: Quantum circuit for approximating  $SU(2^n)$  operators with one single layer.

### 3 Quantum circuit to approximate 2-qubit systems

According to the recursive construction of the SRBB summarized in Section 2.1, the design of the quantum circuit valid for any 2-qubit operator requires the matrix algebra of order 4 and, consequentially, also the algebraic bases of lower order starting from 2. Below, the algebraic basis  $\mathcal{B}^{(4)}$  of interest is briefly reconstructed.

Starting from the Pauli basis  $\mathcal{B}^{(2)}$ ,

$$\sigma_1 = \begin{pmatrix} 0 & 1 \\ 1 & 0 \end{pmatrix} \quad \sigma_2 = \begin{pmatrix} 0 & -i \\ i & 0 \end{pmatrix} \quad \sigma_3 = \begin{pmatrix} 1 & 0 \\ 0 & -1 \end{pmatrix} \quad \sigma_4 = \begin{pmatrix} 1 & 0 \\ 0 & 1 \end{pmatrix} \quad (14)$$

with cardinality  $C = d^2 = 4$ , where  $d = 2^n = 2$  is the matrix order and  $n = 1$  is the number of qubits associated to the corresponding quantum system, it is straightforward to derive the basis  $\mathcal{B}^{(3)}$ :

$$\begin{aligned} B_{1,A}^{(3)} &= \begin{pmatrix} 0 & 1 & 0 \\ 1 & 0 & 0 \\ 0 & 0 & 1 \end{pmatrix} & B_{2,A}^{(3)} &= \begin{pmatrix} 0 & -i & 0 \\ i & 0 & 0 \\ 0 & 0 & 1 \end{pmatrix} & B_{3,A}^{(3)} &= \begin{pmatrix} 1 & 0 & 0 \\ 0 & -1 & 0 \\ 0 & 0 & 1 \end{pmatrix} \\ B_{4,B}^{(3)} &= \begin{pmatrix} 1 & 0 & 0 \\ 0 & 0 & 1 \\ 0 & 1 & 0 \end{pmatrix} & B_{5,B}^{(3)} &= \begin{pmatrix} 0 & 0 & 1 \\ 0 & 1 & 0 \\ 1 & 0 & 0 \end{pmatrix} & B_{6,C}^{(3)} &= \begin{pmatrix} 1 & 0 & 0 \\ 0 & 0 & -i \\ 0 & i & 0 \end{pmatrix} \\ B_{7,C}^{(3)} &= \begin{pmatrix} 0 & 0 & -i \\ 0 & 1 & 0 \\ i & 0 & 0 \end{pmatrix} & B_{8,D}^{(3)} &= \begin{pmatrix} 1 & 0 & 0 \\ 0 & 1 & 0 \\ 0 & 0 & -1 \end{pmatrix} & B_{9,E}^{(3)} &= \begin{pmatrix} 1 & 0 & 0 \\ 0 & 1 & 0 \\ 0 & 0 & 1 \end{pmatrix} \end{aligned} \quad (15)$$

with cardinality  $C = d^2 = 9$ , where  $d = 2^n = 3$  and no integer  $n$  is associated to the quantum register. The recursion property allows to build the basis  $\mathcal{B}^{(4)}$  directly from the previous one, as illustrated in Figure 2, with cardinality  $C = d^2 = 16$ , where  $d = 2^n = 4$  and  $n = 2$  is the register of the quantum system. As pointed out

$$\begin{aligned}
B_{1,A}^{(4)} &= \begin{pmatrix} 0 & 1 & 0 & 0 \\ 1 & 0 & 0 & 0 \\ 0 & 0 & 1 & 0 \\ 0 & 0 & 0 & -1 \end{pmatrix} & B_{2,A}^{(4)} &= \begin{pmatrix} 0 & -i & 0 & 0 \\ i & 0 & 0 & 0 \\ 0 & 0 & 1 & 0 \\ 0 & 0 & 0 & -1 \end{pmatrix} & B_{3,A}^{(4)} &= \begin{pmatrix} 1 & 0 & 0 & 0 \\ 0 & -1 & 0 & 0 \\ 0 & 0 & 1 & 0 \\ 0 & 0 & 0 & -1 \end{pmatrix} \\
B_{4,A}^{(4)} &= \begin{pmatrix} 1 & 0 & 0 & 0 \\ 0 & 0 & 1 & 0 \\ 0 & 1 & 0 & 0 \\ 0 & 0 & 0 & -1 \end{pmatrix} & B_{5,A}^{(4)} &= \begin{pmatrix} 0 & 0 & 1 & 0 \\ 0 & 1 & 0 & 0 \\ 1 & 0 & 0 & 0 \\ 0 & 0 & 0 & -1 \end{pmatrix} & B_{6,A}^{(4)} &= \begin{pmatrix} 1 & 0 & 0 & 0 \\ 0 & 0 & -i & 0 \\ 0 & i & 0 & 0 \\ 0 & 0 & 0 & -1 \end{pmatrix} \\
B_{7,A}^{(4)} &= \begin{pmatrix} 0 & 0 & -i & 0 \\ 0 & 1 & 0 & 0 \\ i & 0 & 0 & 0 \\ 0 & 0 & 0 & -1 \end{pmatrix} & B_{8,A}^{(4)} &= \begin{pmatrix} 1 & 0 & 0 & 0 \\ 0 & 1 & 0 & 0 \\ 0 & 0 & -1 & 0 \\ 0 & 0 & 0 & -1 \end{pmatrix} & B_{9,B}^{(4)} &= \begin{pmatrix} 1 & 0 & 0 & 0 \\ 0 & -1 & 0 & 0 \\ 0 & 0 & 0 & 1 \\ 0 & 0 & 1 & 0 \end{pmatrix} \\
B_{10,B}^{(4)} &= \begin{pmatrix} 0 & 0 & 0 & 1 \\ 0 & -1 & 0 & 0 \\ 0 & 0 & 1 & 0 \\ 1 & 0 & 0 & 0 \end{pmatrix} & B_{11,B}^{(4)} &= \begin{pmatrix} 1 & 0 & 0 & 0 \\ 0 & 0 & 0 & 1 \\ 0 & 0 & -1 & 0 \\ 0 & 1 & 0 & 0 \end{pmatrix} & B_{12,C}^{(4)} &= \begin{pmatrix} 1 & 0 & 0 & 0 \\ 0 & -1 & 0 & 0 \\ 0 & 0 & 0 & -i \\ 0 & 0 & i & 0 \end{pmatrix} \\
B_{13,C}^{(4)} &= \begin{pmatrix} 0 & 0 & 0 & -i \\ 0 & -1 & 0 & 0 \\ 0 & 0 & 1 & 0 \\ i & 0 & 0 & 0 \end{pmatrix} & B_{14,C}^{(4)} &= \begin{pmatrix} 1 & 0 & 0 & 0 \\ 0 & 0 & 0 & -i \\ 0 & 0 & -1 & 0 \\ 0 & i & 0 & 0 \end{pmatrix} & B_{15,D}^{(4)} &= \begin{pmatrix} 1 & 0 & 0 & 0 \\ 0 & -1 & 0 & 0 \\ 0 & 0 & 1 & 0 \\ 0 & 0 & 0 & -1 \end{pmatrix} \\
B_{16,E}^{(4)} &= \begin{pmatrix} 1 & 0 & 0 & 0 \\ 0 & 1 & 0 & 0 \\ 0 & 0 & 1 & 0 \\ 0 & 0 & 0 & 1 \end{pmatrix}
\end{aligned}$$

Figure 2: Complete set of RBB matrix elements  $B_j^{(4)}$  for  $n = 2$ .

in Section 2.1, the set  $\{B_j^{(4)} : 1 \leq j \leq 15\}$  is a basis for the  $su(4)$  matrix algebra whose elements satisfy the properties of hermiticity, unitarity and zero trace:

$$\text{for } 1 \leq j \leq 15, \quad [B_j^{(4)}]^\dagger = B_j^{(4)}, \quad [B_j^{(4)}]^2 = [B_j^{(4)}][B_j^{(4)}]^\dagger = \mathbb{I}_4, \quad \text{tr}[B_j^{(4)}] = 0 \quad (16)$$

The next step concerns the transition to the SRBB and it is crucial to identify the diagonal basis elements and their precise position,

$$B_j^{(4)} \text{ diagonal elements : } j \in \mathcal{J} = \{m^2 - 1, 2 \leq m \leq 4\} \cup \{d^2\} = \{3, 8, 15, 16\} \quad (17)$$

so as to appropriately replace them with Hermitian unitary diagonal matrices generated starting from Pauli strings, specifically Pauli strings with only  $\mathbb{I}_2$  and  $\sigma_3$ . This substitution will return the corresponding SRBB diagonal elements for the considered matrix algebra, absolutely necessary in the construction and implementation of the correct quantum circuit. In Table 1, the replacement criterion is illustrated. Each diagonal element,

Decimal	Binary	String	Matrix	Element	Replaced
0	00	$\mathbb{I}_2 \otimes \mathbb{I}_2$	$\mathbb{I}_4$	16	no
1	01	$\mathbb{I}_2 \otimes \sigma_3$	$\text{diag}(1, -1, 1, -1)$	3	no
2	10	$\sigma_3 \otimes \mathbb{I}_2$	$\text{diag}(1, 1, -1, -1)$	8	no
3	11	$\sigma_3 \otimes \sigma_3$	$\text{diag}(1, -1, -1, 1)$	15	yes

Table 1: The new sequence of diagonal basis elements that marks the transition to SRBB.

whose position  $j$  is known from equation (17), is associated with the binary representation of the numbers from 0 to  $d - 1$ , according to the following recipe: every 0-valued bit of the binary string is replaced with  $\mathbb{I}_2$ , every 1-valued bit is instead replaced with  $\sigma_3$  and the corresponding diagonal element is obtained through the tensor



product of the two bits. Then, the old diagonal elements are compared with the new ones, neglecting the one associated with 0 (which will always be the last), and replaced only if found different.

The complete SRBB of order 4, identified as the set  $\mathcal{U}^{(4)} = \{U_j^{(4)} : 1 \leq j \leq 16\}$ , is defined by

$$U_j^{(4)} = \begin{cases} \text{new diagonal elements if } j \in \mathcal{J} = \{3, 8, 15, 16\} \\ B_j^{(4)} \text{ otherwise} \end{cases} \quad (18)$$

the elements of which are reported for completeness in Figure 3.

$$\begin{aligned} U_1^{(4)} &= \begin{pmatrix} 0 & 1 & 0 & 0 \\ 1 & 0 & 0 & 0 \\ 0 & 0 & 1 & 0 \\ 0 & 0 & 0 & -1 \end{pmatrix} & U_2^{(4)} &= \begin{pmatrix} 0 & -i & 0 & 0 \\ i & 0 & 0 & 0 \\ 0 & 0 & 1 & 0 \\ 0 & 0 & 0 & -1 \end{pmatrix} & U_3^{(4)} &= \begin{pmatrix} 1 & 0 & 0 & 0 \\ 0 & -1 & 0 & 0 \\ 0 & 0 & 1 & 0 \\ 0 & 0 & 0 & -1 \end{pmatrix} \\ U_4^{(4)} &= \begin{pmatrix} 1 & 0 & 0 & 0 \\ 0 & 0 & 1 & 0 \\ 0 & 1 & 0 & 0 \\ 0 & 0 & 0 & -1 \end{pmatrix} & U_5^{(4)} &= \begin{pmatrix} 0 & 0 & 1 & 0 \\ 0 & 1 & 0 & 0 \\ 1 & 0 & 0 & 0 \\ 0 & 0 & 0 & -1 \end{pmatrix} & U_6^{(4)} &= \begin{pmatrix} 1 & 0 & 0 & 0 \\ 0 & 0 & -i & 0 \\ 0 & i & 0 & 0 \\ 0 & 0 & 0 & -1 \end{pmatrix} \\ U_7^{(4)} &= \begin{pmatrix} 0 & 0 & -i & 0 \\ 0 & 1 & 0 & 0 \\ i & 0 & 0 & 0 \\ 0 & 0 & 0 & -1 \end{pmatrix} & U_8^{(4)} &= \begin{pmatrix} 1 & 0 & 0 & 0 \\ 0 & 1 & 0 & 0 \\ 0 & 0 & -1 & 0 \\ 0 & 0 & 0 & -1 \end{pmatrix} & U_9^{(4)} &= \begin{pmatrix} 1 & 0 & 0 & 0 \\ 0 & -1 & 0 & 0 \\ 0 & 0 & 0 & 1 \\ 0 & 0 & 1 & 0 \end{pmatrix} \\ U_{10}^{(4)} &= \begin{pmatrix} 0 & 0 & 0 & 1 \\ 0 & -1 & 0 & 0 \\ 0 & 0 & 1 & 0 \\ 1 & 0 & 0 & 0 \end{pmatrix} & U_{11}^{(4)} &= \begin{pmatrix} 1 & 0 & 0 & 0 \\ 0 & 0 & 0 & 1 \\ 0 & 0 & -1 & 0 \\ 0 & 1 & 0 & 0 \end{pmatrix} & U_{12}^{(4)} &= \begin{pmatrix} 1 & 0 & 0 & 0 \\ 0 & -1 & 0 & 0 \\ 0 & 0 & 0 & -i \\ 0 & 0 & i & 0 \end{pmatrix} \\ U_{13}^{(4)} &= \begin{pmatrix} 0 & 0 & 0 & -i \\ 0 & -1 & 0 & 0 \\ 0 & 0 & 1 & 0 \\ i & 0 & 0 & 0 \end{pmatrix} & U_{14}^{(4)} &= \begin{pmatrix} 1 & 0 & 0 & 0 \\ 0 & 0 & 0 & -i \\ 0 & 0 & -1 & 0 \\ 0 & i & 0 & 0 \end{pmatrix} & U_{15}^{(4)} &= \begin{pmatrix} 1 & 0 & 0 & 0 \\ 0 & -1 & 0 & 0 \\ 0 & 0 & -1 & 0 \\ 0 & 0 & 0 & 1 \end{pmatrix} \\ U_{16}^{(4)} &= \begin{pmatrix} 1 & 0 & 0 & 0 \\ 0 & 1 & 0 & 0 \\ 0 & 0 & 1 & 0 \\ 0 & 0 & 0 & 1 \end{pmatrix} \end{aligned}$$

Figure 3: Complete set of SRBB matrix elements  $U_j^{(4)}$  for  $n = 2$ .

### 3.1 The permutation group and ZYZ-decompositions

Before proceeding further, some algebraic properties need to be analyzed in order to identify  $n = 2$  as a special case outside the general scalability scheme proposed in the literature [33]. Considering the permutation group  $P_4$  as indicated by equation (10), the properties of the algebraic basis under permutation are encoded respectively in its two subsets of even/odd transpositions (or 2-cycles):

$$P_4^{e/o} = \{P_{(\alpha,\beta)} \in P_4 \mid \alpha \text{ even}, \beta \text{ even/odd}\} \quad (19)$$

where  $P_4^e = \{P_{(2,4)}\}$  and  $P_4^o = \{P_{(2,3)}\}$ . In general, it is possible to partition further, identifying the  $2^{n-1} - 1$  sets  $T_x^{e/o}$  of  $2^{n-2}$  disjoint transpositions; instead, for  $n = 2$  there is only one set of disjoint transpositions for both cases ( $x = 1$ ) containing only one permutation<sup>6</sup>:

$$P_4^e = \{P_{(2,4)}\} = T_1^e = \prod T_1^e = \begin{pmatrix} 1 & 0 & 0 & 0 \\ 0 & 0 & 0 & 1 \\ 0 & 0 & 1 & 0 \\ 0 & 1 & 0 & 0 \end{pmatrix} \quad \text{and} \quad P_4^o = \{P_{(2,3)}\} = T_1^o = \prod T_1^o = \begin{pmatrix} 1 & 0 & 0 & 0 \\ 0 & 0 & 1 & 0 \\ 0 & 1 & 0 & 0 \\ 0 & 0 & 0 & 1 \end{pmatrix} \quad (20)$$

<sup>6</sup>See the definition (9) to understand this particular case.

### 3.1.1 CNOT sequences

The permutations considered by definition (9) are called 2-cycles or transpositions and can be implemented through CNOT sequences; there is a precise scheme to follow in order to get the correct sequence (see for instance [32]), which is slightly different between the even and the odd case. In the range  $1 \leq x \leq 2^{n-1} - 1$ , the binary representation of  $x$  is obtained according to the formula  $\sum_{i=1}^{n-1} 2^{n-i-1} x_i$ , thus enumerating all  $\prod T_x^e$  factors. Then, for each  $x$ , a CNOT gate is associated with the control in the  $n$ -th qubit and the target in the  $i$ -th qubit, where  $x_i = 1$ . For the odd case, the same scheme is used with only one variation: the presence of the parameter  $k$ , that is the lowest index for which  $x_k = 1$  in the binary string. Thus,  $\prod T_x^o$  factors correspond to the circuit  $CNOT_{(k,n)} \prod T_x^e CNOT_{(k,n)}$ .

This recipe allows to derive the quantum circuit associated to each  $\prod T_x^{e/o}$  factor, but the link with permutation matrices remains somewhat hidden. Firstly, the binary representation previously described considers only  $n - 1$  qubits, i.e., only the qubits suitable for targets (the control qubit is always the  $n$ -th). In this way, considering the binary representation for each  $x$  is equivalent to considering all possible combinations between target lines and the  $n$ -th qubit. Secondly, from a matrix representation viewpoint, the states of the  $n$ -qubit quantum register are ordered according to the usual sequence of kets:

$$\begin{aligned} |0\dots 00\rangle &= |0\rangle \otimes \dots \otimes |0\rangle \otimes |0\rangle = (1, 0, \dots, 0, 0)^T \\ |0\dots 01\rangle &= |0\rangle \otimes \dots \otimes |0\rangle \otimes |1\rangle = (0, 1, \dots, 0, 0)^T \\ &\dots = \dots \\ |1\dots 11\rangle &= |1\rangle \otimes \dots \otimes |1\rangle \otimes |1\rangle = (0, 0, \dots, 0, 1)^T \end{aligned}$$

in which only the ones ending with a 1-valued qubit activate the CNOT. The latter are exactly half of the total number of states and, thanks to the properties of binary representation, they are always coupled with respect to the only one qubit that changes between each other. See for instance the  $\prod T_1^e$  factor for  $n = 2$  ( $x = 1$ ):

$$\begin{aligned} x = 1 \equiv 2^0 \cdot x_1 \iff x_1 = 1 &\longrightarrow CNOT_{(2,1)} \\ \prod T_1^e = P_{(2,4)} = \begin{pmatrix} 1 & 0 & 0 & 0 \\ 0 & 0 & 0 & 1 \\ 0 & 0 & 1 & 0 \\ 0 & 1 & 0 & 0 \end{pmatrix} &\begin{array}{l} \rightarrow |00\rangle = (1, 0, 0, 0)^T \\ \rightarrow |01\rangle = (0, 1, 0, 0)^T \\ \rightarrow |10\rangle = (0, 0, 1, 0)^T \\ \rightarrow |11\rangle = (0, 0, 0, 1)^T \end{array} \end{aligned}$$

The remaining half of the states, the ones ending with a 0-valued qubit, do not activate the CNOT and represent the so-called fixed points of the transposition or of the 2-cycle. As shown in the example, the pair of indices  $(\alpha, \beta) = (2, 4)$  corresponds to the second and fourth vectors (coupled by the first qubit that represents the two possible values of the target line) that activate the CNOT. Of course, the same link between 2-cycle (or transposition) matrices and CNOT-sequences applies for any value of  $n$ .

### 3.1.2 Properties under permutation

As anticipated in Section 2.1, the decomposition techniques crucially depends on the algebraic properties of each main factor, in turn depending on its sub-groupings. However, for 2-qubit systems an exception appears to the original scalable pattern [33]. In order to highlight this peculiar case, the analysis of the algebraic properties under permutation is mandatory.

**Proposition 1.** *For  $n = 2$ ,  $M_x^o \in SU(2^n)$  are block-diagonal unitary matrices with  $SU(2)$  blocks and admit a  $ZYZ$ -type decomposition.*

*Proof.* Considering a general 2-cycle  $P_{(\alpha, \beta)}$  in the range  $1 \leq \alpha < \beta \leq 2^n$ , the analysis of the permutation properties of SRBB elements can be splitted into four cases based on the parity<sup>7</sup> of indices  $\alpha$  and  $\beta$ :

- i. permutation property  $P_{(\alpha+1, \beta)} \exp\{i\theta_{f_\beta(\alpha)} U_{f_\beta(\alpha)}\} P_{(\alpha+1, \beta)}$  with  $\alpha$  odd and  $\beta$  even  
 $\implies P_{(2,4)}, f_4(1) = 13$
- ii. permutation property  $P_{(\alpha, \beta+1)} \exp\{i\theta_{f_\beta(\alpha)} U_{f_\beta(\alpha)}\} P_{(\alpha, \beta+1)}$  with  $\alpha$  even and  $\beta$  odd  
 $\implies P_{(2,4)}, f_3(2) = 6$
- iii. permutation property  $P_{(\alpha+1, \beta)} \exp\{i\theta_{f_\beta(\alpha)} U_{f_\beta(\alpha)}\} P_{(\alpha+1, \beta)}$  with  $\alpha$  odd and  $\beta$  odd  
 $\implies P_{(2,3)}, f_3(1) = 7$

<sup>7</sup>The function  $h_\beta(\alpha)$  follows the same analysis and the corresponding permutation properties are reported for completeness in Section 3.4.

iv. permutation property  $P_{(\alpha, \beta-1)} \exp\{i\theta_{f_\beta(\alpha)} U_{f_\beta(\alpha)}\} P_{(\alpha, \beta-1)}$  with  $\alpha$  even and  $\beta$  even  
 $\implies P_{(2,3)}, f_4(2) = 14$

The four cases based on the parity of the pair of indices  $(\alpha, \beta)$  are in correspondence with the definition of SRBB elements that build the  $M_x^{e/o}$  factors of equation (12). Following the properties i-iv listed above, it is straightforward to show the membership of these matrices to  $M_2 ZYZ$  after the appropriate permutation:

$$P_{(2,4)} \exp\{i\theta_{13} U_{13}\} P_{(2,4)} = P_{(2,4)} \begin{pmatrix} \cos \theta_{13} & 0 & 0 & \sin \theta_{13} \\ 0 & e^{-i\theta_{13}} & 0 & 0 \\ 0 & 0 & e^{i\theta_{13}} & 0 \\ -\sin \theta_{13} & 0 & 0 & \cos \theta_{13} \end{pmatrix} P_{(2,4)} = \begin{pmatrix} \cos \theta_{13} & \sin \theta_{13} & 0 & 0 \\ -\sin \theta_{13} & \cos \theta_{13} & 0 & 0 \\ 0 & 0 & e^{i\theta_{13}} & 0 \\ 0 & 0 & 0 & e^{-i\theta_{13}} \end{pmatrix} \quad (21)$$

$$P_{(2,4)} \exp\{i\theta_6 U_6\} P_{(2,4)} = P_{(2,4)} \begin{pmatrix} e^{i\theta_6} & 0 & 0 & 0 \\ 0 & \cos \theta_6 & \sin \theta_6 & 0 \\ 0 & -\sin \theta_6 & \cos \theta_6 & 0 \\ 0 & 0 & 0 & e^{-i\theta_6} \end{pmatrix} P_{(2,4)} = \begin{pmatrix} e^{i\theta_6} & 0 & 0 & 0 \\ 0 & e^{-i\theta_6} & 0 & 0 \\ 0 & 0 & \cos \theta_6 & -\sin \theta_6 \\ 0 & 0 & \sin \theta_6 & \cos \theta_6 \end{pmatrix} \quad (22)$$

$$P_{(2,3)} \exp\{i\theta_7 U_7\} P_{(2,3)} = P_{(2,3)} \begin{pmatrix} \cos \theta_7 & 0 & \sin \theta_7 & 0 \\ 0 & e^{i\theta_7} & 0 & 0 \\ -\sin \theta_7 & 0 & \cos \theta_7 & 0 \\ 0 & 0 & 0 & e^{-i\theta_7} \end{pmatrix} P_{(2,3)} = \begin{pmatrix} \cos \theta_7 & \sin \theta_7 & 0 & 0 \\ -\sin \theta_7 & \cos \theta_7 & 0 & 0 \\ 0 & 0 & e^{i\theta_7} & 0 \\ 0 & 0 & 0 & e^{-i\theta_7} \end{pmatrix} \quad (23)$$

$$P_{(2,3)} \exp\{i\theta_{14} U_{14}\} P_{(2,3)} = P_{(2,3)} \begin{pmatrix} e^{i\theta_{14}} & 0 & 0 & 0 \\ 0 & \cos \theta_{14} & 0 & \sin \theta_{14} \\ 0 & 0 & e^{-i\theta_{14}} & 0 \\ 0 & -\sin \theta_{14} & 0 & \cos \theta_{14} \end{pmatrix} P_{(2,3)} = \begin{pmatrix} e^{i\theta_{14}} & 0 & 0 & 0 \\ 0 & e^{-i\theta_{14}} & 0 & 0 \\ 0 & 0 & \cos \theta_{14} & \sin \theta_{14} \\ 0 & 0 & -\sin \theta_{14} & \cos \theta_{14} \end{pmatrix} \quad (24)$$

where  $M_2 ZYZ$  indicates the 2-qubit quantum circuit for a general  $ZYZ$ -decomposition. The analysis is completely identical for the function  $h_\beta(\alpha)$  and does not add any relevant contribution to the proof.  $\square$

With reference to equations (5) and Proposition 1, in Table 2 the shortcut to find out which elements come into play in each main factor and the corresponding decomposition property are outlined. The construction of

Factor	Index	Range	Elements	Property
Z	$j^2 - 1$	$2 \leq j \leq 4$	3, 8, 15	diagonal
$\Psi, 1^\circ$	$(2j - 1)^2(4j^2 - 2j)$	$1 \leq j \leq 2$	1, 2, 9, 12	$ZYZ$ -decomp.
$\Psi, 2^\circ$	$h_\beta(\alpha - 1), f_\beta(\alpha - 1), h_{\beta-1}(\alpha), f_{\beta-1}(\alpha)$	$\alpha = 2, \beta = 4$	10, 13, 4, 6	$ZYZ$ -decomp. after $P_{(2,4)}$
$\Phi$	$h_\beta(\alpha - 1), f_\beta(\alpha - 1), h_{\beta+1}(\alpha), f_{\beta+1}(\alpha)$	$\alpha = 2, \beta = 3$	5, 7, 11, 14	$ZYZ$ -decomp. after $P_{(2,3)}$

Table 2: Shortcut for grouping SRBB elements into the three main factors.

the quantum circuit, as described by the general equation (5) with  $l = 1$ , can then start: the three main factors are shown separately with the corresponding quantum sub-circuits and omitting the layer index for simplicity. Only by composing all the blocks in sequence, in the correct logic order, it will be possible to identify the relevant simplifications that will lead to reduce the number of CNOT gates.

### 3.2 Diagonal contributions

In this subsection, the  $Z$ -factor of equation (5) responsible for diagonal contributions will be analyzed and computed for one single layer<sup>8</sup>:

$$Z(\Theta_Z) = \prod_{j=2}^4 \exp\{i\theta_{j^2-1} U_{j^2-1}\} \quad (25)$$

The elements of the algebraic basis  $\mathcal{U}^{(4)}$  that come into play belong to the set  $\mathcal{J}_Z = \{m^2 - 1, 2 \leq m \leq 4\} = \{3, 8, 15\} = \mathcal{J} - \{16\}$ , which are exactly all the diagonal elements of the basis except the last one. Accordingly,

<sup>8</sup>The superscript  $2^n$  of each algebraic basis element, indicating the matrix order, is omitted for simplicity and can be recovered from the context.

referring to the basis in Figure 3, it is possible to write:

$$\begin{aligned}
 Z(\Theta_Z) &= \exp\{i\theta_3 U_3\} \exp\{i\theta_8 U_8\} \exp\{i\theta_{15} U_{15}\} = \\
 &= \begin{pmatrix} e^{i(\theta_3+\theta_8+\theta_{15})} & 0 & 0 & 0 \\ 0 & e^{i(-\theta_3+\theta_8-\theta_{15})} & 0 & 0 \\ 0 & 0 & e^{i(\theta_3-\theta_8-\theta_{15})} & 0 \\ 0 & 0 & 0 & e^{i(-\theta_3-\theta_8+\theta_{15})} \end{pmatrix} \quad (26)
 \end{aligned}$$

In order to draw the corresponding circuit, Table 1 is useful to associate each diagonal element to the appropriate gate sequence. Of that table, only the rows corresponding to the elements involved in the  $Z$ -factor are relevant, therefore all the rows apart from the first. Then, for each row, the elements of the Pauli string are reported on a line, respecting the order in which they appear in the string, from left to right. The lines are divided into columns, each representing a qubit of the quantum system under consideration, labeled by an integer from left to right which takes into account the numbering of the quantum register  $\{0, 1, 2, \dots\}$ . It is important to have the elements corresponding to the binary units on the right end, aligned with the last qubit. The line diagram therefore does not see the circuit in the usual way (horizontally), but rather as if it was rotated vertically, with the first qubit of the register (the first from the top) now positioned to the left. This step is fundamental to identify the simplification scheme at each order  $n$ , as explained in Section 7. Finally, parameters  $m$  and  $m'$  have to be defined: while  $m$  is the largest integer after which all remaining elements of the string are  $\mathbb{I}_2$  (i.e., it is the integer that corresponds to the rightmost  $\sigma_3$ ),  $m'$  indicates all  $\sigma_3$  elements preceding  $m$ ; Figure 4 below shows this step.

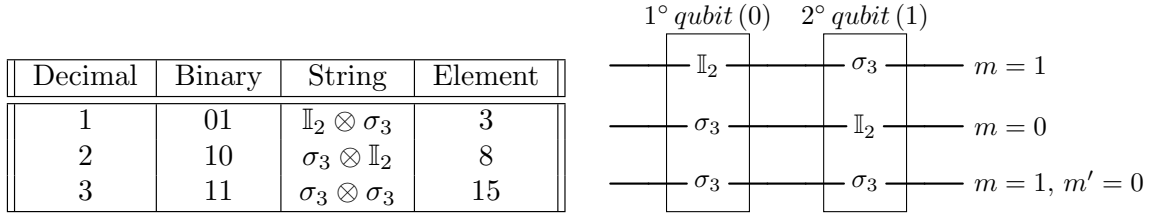


Figure 4: Diagram to find the position of CNOTs and rotation gates.

Finally, the last step consists in associating each line of the previous diagram (and therefore each exponential factor considered) with one or more merged gates, following this scheme: each  $m$  corresponds to the qubit on which to perform a  $z$ -rotation and each  $m'$  corresponds to a pair of CNOTs, before and after the rotation gate, with the target in the  $m$ -th qubit and the control in the  $m'$ -th qubit; Figure 5 below shows this last step. Being

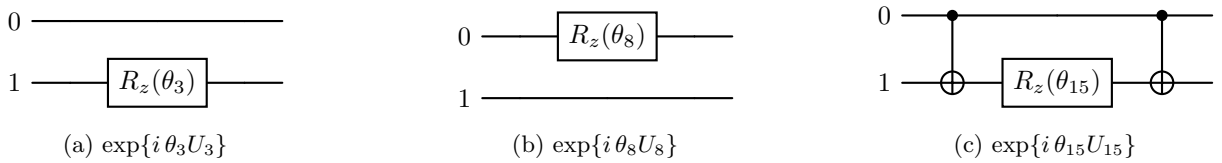


Figure 5: Three little blocks that make up the  $Z$ -factor circuit for  $n = 2$ .

diagonal matrices, the ordering of these little blocks is irrelevant and what is shown in Figure 6 is the ordering that minimizes the number of CNOTs if inserted in the whole circuit<sup>9</sup>.

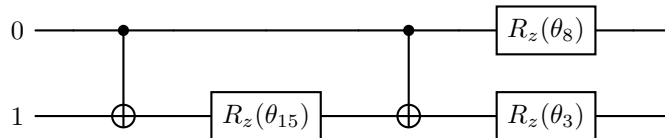


Figure 6: CNOT-optimized quantum circuit for the  $Z$ -factor in the  $n = 2$  case.

<sup>9</sup>As mentioned previously,  $n = 2$  case represents an exception to the scalability scheme; therefore, the motivation behind this particular sorting lies solely in minimizing the number of CNOTs when combined with the remaining circuit, outside of any recursive scheme.

### 3.3 Even contributions

In this subsection, the  $\Psi$ -factor of equation (5) responsible for even contributions, which come from exponentials of SRBB elements (first sub-factor of type  $A$ ) and from permutations of exponentials of SRBB elements (second sub-factor of type  $B$ ), is analyzed and computed for one single layer:

$$\Psi(\Theta_\Psi) = \left[ \prod_{j=1}^2 \exp\{i\theta_{(2j-1)^2} U_{(2j-1)^2}\} \exp\{i\theta_{4j^2-2j} U_{4j^2-2j}\} \right] \left( \prod T_1^e \right) M_1^e \left( \prod T_1^e \right) \quad (27)$$

where  $\prod T_1^e = P_{(2,4)}$  and<sup>10</sup>

$$\begin{aligned} M_1^e &= \prod T_1^e \left[ \prod_{(2,4)} \exp\{i\theta U_{h_\beta(\alpha-1)}\} \exp\{i\theta U_{f_\beta(\alpha-1)}\} \exp\{i\theta U_{h_{\beta-1}(\alpha)}\} \exp\{i\theta U_{f_{\beta-1}(\alpha)}\} \right] \prod T_1^e = \\ &= P_{(2,4)} \left[ \exp\{i\theta_{h_4(1)} U_{h_4(1)}\} \exp\{i\theta_{f_4(1)} U_{f_4(1)}\} \exp\{i\theta_{h_3(2)} U_{h_3(2)}\} \exp\{i\theta_{f_3(2)} U_{f_3(2)}\} \right] P_{(2,4)} \end{aligned} \quad (28)$$

The elements of the algebraic basis  $\mathcal{U}^{(4)}$  that come into play belong to the following sets:

- a set of pairs called  $\mathcal{A}_\Psi$  makes up the first sub-factor of type  $A$ ,

$$\mathcal{A}_\Psi = \{[(2j-1)^2, (4j^2-2j)], 1 \leq j \leq 2\} = \{(1,2), (9,12)\} \quad (29)$$

- a set (one quadruple) called  $\mathcal{B}_\Psi$ , makes up the second sub-factor of type  $B$ ,

$$\mathcal{B}_\Psi = \{h_4(1), f_4(1), h_3(2), f_3(2)\} = \{10, 13, 4, 6\} \quad (30)$$

Accordingly, referring to the basis in Figure 3, the first sub-factor of type  $A$  is a  $2 \times 2$  block diagonal matrix,

$$\exp\{i\theta_1 U_1\} \exp\{i\theta_2 U_2\} \exp\{i\theta_9 U_9\} \exp\{i\theta_{12} U_{12}\} = \begin{pmatrix} A_\Psi^1 & 0 \\ 0 & A_\Psi^2 \end{pmatrix} \quad (31)$$

where each block belongs to  $SU(2)$ , as can be quickly verified,

$$\begin{aligned} A_\Psi^1 &= \begin{pmatrix} e^{i(\theta_9+\theta_{12})} (\cos \theta_1 \cos \theta_2 - i \sin \theta_1 \sin \theta_2) & e^{-i(\theta_9+\theta_{12})} (\cos \theta_1 \sin \theta_2 + i \sin \theta_1 \cos \theta_2) \\ e^{i(\theta_9+\theta_{12})} (i \sin \theta_1 \cos \theta_2 - \cos \theta_1 \sin \theta_2) & e^{-i(\theta_9+\theta_{12})} (i \sin \theta_1 \sin \theta_2 + \cos \theta_1 \cos \theta_2) \end{pmatrix} \\ A_\Psi^2 &= \begin{pmatrix} e^{i(\theta_1+\theta_2)} (\cos \theta_9 \cos \theta_{12} - i \sin \theta_9 \sin \theta_{12}) & e^{i(\theta_1+\theta_2)} (\cos \theta_9 \sin \theta_{12} + i \sin \theta_9 \cos \theta_{12}) \\ e^{-i(\theta_1+\theta_2)} (i \sin \theta_9 \cos \theta_{12} - \cos \theta_9 \sin \theta_{12}) & e^{-i(\theta_1+\theta_2)} (i \sin \theta_9 \sin \theta_{12} + \cos \theta_9 \cos \theta_{12}) \end{pmatrix} \end{aligned} \quad (32)$$

Therefore, the first sub-factor of type  $A$  is a unitary matrix belonging to  $M_2 ZY Z$ , a fundamental building block of the final quantum circuit that can be implemented with  $z$ -rotations and CNOT gates only [32, 18]. Inside the second sub-factor of type  $B$ , its factor  $M_1^e$  is a  $2 \times 2$  block diagonal matrix too,

$$M_1^e = P_{(2,4)} \left[ \exp\{i\theta_{10} U_{10}\} \exp\{i\theta_{13} U_{13}\} \exp\{i\theta_4 U_4\} \exp\{i\theta_6 U_6\} \right] P_{(2,4)} = \begin{pmatrix} B_\Psi^1 & 0 \\ 0 & B_\Psi^2 \end{pmatrix} \quad (33)$$

where each block belongs again to  $SU(2)$ , as can be quickly verified,

$$\begin{aligned} B_\Psi^1 &= \begin{pmatrix} e^{i(\theta_4+\theta_6)} (\cos \theta_{10} \cos \theta_{13} - i \sin \theta_{10} \sin \theta_{13}) & e^{-i(\theta_4+\theta_6)} (\cos \theta_{10} \sin \theta_{13} + i \sin \theta_{10} \cos \theta_{13}) \\ e^{i(\theta_4+\theta_6)} (i \sin \theta_{10} \cos \theta_{13} - \cos \theta_{10} \sin \theta_{13}) & e^{-i(\theta_4+\theta_6)} (i \sin \theta_{10} \sin \theta_{13} + \cos \theta_{10} \cos \theta_{13}) \end{pmatrix} \\ B_\Psi^2 &= \begin{pmatrix} e^{i(\theta_{10}+\theta_{13})} (i \sin \theta_4 \sin \theta_6 + \cos \theta_4 \cos \theta_6) & e^{i(\theta_{10}+\theta_{13})} (i \sin \theta_4 \cos \theta_6 - \cos \theta_4 \sin \theta_6) \\ e^{-i(\theta_{10}+\theta_{13})} (\cos \theta_4 \sin \theta_6 + i \sin \theta_4 \cos \theta_6) & e^{-i(\theta_{10}+\theta_{13})} (\cos \theta_4 \cos \theta_6 - i \sin \theta_4 \sin \theta_6) \end{pmatrix} \end{aligned} \quad (34)$$

Consequentially, also the second sub-factor of type  $B$  is a unitary matrix belonging to  $M_2 ZY Z$ . The decomposition, and therefore the implementation, of  $M_2 ZY Z$ -type matrices is always identical; the only complication lies in the relationship between gate parameters and those of the three multi-controlled rotations that compactly encode a general  $M_n ZY Z$ -type matrix<sup>11</sup> [17]. Figure 7 provides the circuit for the first sub-factor of type  $A$  (the same will be for  $M_1^e$ ). Concerning the  $\Psi$ -factor, only the  $\prod T_1^e$  sub-factor remains to be analyzed; since

<sup>10</sup>To avoid repetitions and write compact formulas, we omit repeating the subscript for the  $\theta_i$  angles, which will still be equal to that of the associated basis element.

<sup>11</sup>Since this work focuses on the implementation aspects of the unitary approximation algorithm via a variational quantum circuit (VQC), this mathematical relationship is superfluous. Specifically, the effectiveness of the approximation will depend on the machine learning process capable of seeing only the parameters of the variational circuit as they were presented to it and not their relationship with abstract mathematical elements of the algebraic basis. For this reason, the rotation parameters of the circuit will be renamed as  $\theta_j^*$ .

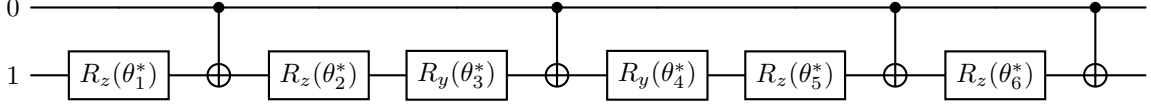


Figure 7: Fully decomposed  $M_2ZYZ$  quantum circuit.

the latter is represented by a permutation matrix, from an implementation viewpoint there are no sorting or decomposition complications. Using the recipe described in Section 3.1.1 with the precaution of labeling the qubits from 0 onwards<sup>12</sup>, it is straightforward to deduce the corresponding quantum circuit (see Figure 8).

Decimal	Bits	Binary	Control-Target
1	$x_0$	1	(1,0)

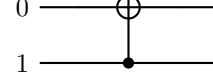


Figure 8: Diagram to find the control-target pair for the CNOT representing  $\prod T_1^e$ .

### 3.4 Odd contributions

In this subsection, the  $\Phi$ -factor of equation (5) responsible for odd contributions, which come only from permutations of exponentials of SRBB elements (sub-factor of type  $B$ ), is analyzed and computed for one single layer:

$$\Phi(\Theta_\Phi) = \left( \prod T_1^o \right) M_1^o \left( \prod T_1^o \right) \quad (35)$$

where  $\prod T_1^o = P_{(2,3)}$  and<sup>13</sup>

$$\begin{aligned} M_1^o &= \prod T_1^o \left[ \prod_{(2,3)} \exp\{i\theta U_{h_\beta(\alpha-1)}\} \exp\{i\theta U_{f_\beta(\alpha-1)}\} \exp\{i\theta U_{h_{\beta+1}(\alpha)}\} \exp\{i\theta U_{f_{\beta+1}(\alpha)}\} \right] \prod T_1^o = \\ &= P_{(2,3)} [\exp\{i\theta_{h_3(1)} U_{h_3(1)}\} \exp\{i\theta_{f_3(1)} U_{f_3(1)}\} \exp\{i\theta_{h_4(2)} U_{h_4(2)}\} \exp\{i\theta_{f_4(2)} U_{f_4(2)}\}] P_{(2,3)} \end{aligned} \quad (36)$$

The elements of the algebraic basis  $\mathcal{U}^{(4)}$  that come into play belong to the following set (one quadruple):

$$\mathcal{B}_\Phi = \{h_3(1), f_3(1), h_4(2), f_4(2)\} = \{5, 7, 11, 14\} \quad (37)$$

Accordingly, referring to the basis of Figure 3, the factor  $M_1^o$  inside the sub-factor of type  $B$  is a  $2 \times 2$  block diagonal matrix as in the even case<sup>14</sup>,

$$M_1^o = P_{(2,3)} [\exp\{i\theta_5 U_5\} \exp\{i\theta_7 U_7\} \exp\{i\theta_{11} U_{11}\} \exp\{i\theta_{14} U_{14}\}] P_{(2,3)} = \begin{pmatrix} B_\Phi^1 & 0 \\ 0 & B_\Phi^2 \end{pmatrix} \quad (38)$$

where each block belongs again to  $SU(2)$ , as can be quickly verified,

$$\begin{aligned} B_\Phi^1 &= \begin{pmatrix} e^{i(\theta_{11}+\theta_{14})}(\cos \theta_5 \cos \theta_7 - i \sin \theta_5 \sin \theta_7) & e^{-i(\theta_{11}+\theta_{14})}(\cos \theta_5 \sin \theta_7 + i \sin \theta_5 \cos \theta_7) \\ e^{i(\theta_{11}+\theta_{14})}(i \sin \theta_5 \cos \theta_7 - \cos \theta_5 \sin \theta_7) & e^{-i(\theta_{11}+\theta_{14})}(i \sin \theta_5 \sin \theta_7 + \cos \theta_5 \cos \theta_7) \end{pmatrix} \\ B_\Phi^2 &= \begin{pmatrix} e^{i(\theta_5+\theta_7)}(\cos \theta_{11} \cos \theta_{14} - i \sin \theta_{11} \sin \theta_{14}) & e^{i(\theta_5+\theta_7)}(\cos \theta_{11} \sin \theta_{14} + i \sin \theta_{11} \cos \theta_{14}) \\ e^{-i(\theta_5+\theta_7)}(i \sin \theta_{11} \cos \theta_{14} - \cos \theta_{11} \sin \theta_{14}) & e^{-i(\theta_5+\theta_7)}(i \sin \theta_{11} \sin \theta_{14} + \cos \theta_{11} \cos \theta_{14}) \end{pmatrix} \end{aligned} \quad (39)$$

Therefore, the sub-factor of type  $B$  produces another unitary matrix belonging to  $M_2ZYZ$  whose circuit is essentially identical to its even counterpart (see Figure 7).

It is clear that for  $n = 2$ , the odd contributions of the  $\Phi$ -factor deviate slightly from the scalability scheme presented in [32], providing a notable simplification of the circuit which only counts  $M_2ZYZ$ -type matrices,

<sup>12</sup>The binary representation of  $x$  is now obtained according to the formula  $\sum_{i=1}^{n-1} 2^{n-i-1} x_{i-1}$ .

<sup>13</sup>To avoid repetitions and write compact formulas, we omit repeating the subscript for the  $\theta_i$  angles, which will still be equal to that of the associated basis element.

<sup>14</sup>Due to permutation properties described in Section 3.1.2, also under odd-index permutations the subset of elements building the  $\Phi$ -factor produce a  $M_2ZYZ$ -type matrix. As clarified in Section 4, this anomalous property holds only for 2-qubit systems.

diagonal elements and CNOT-permutations. The  $\Phi$ -factor becomes no longer implementable through  $ZYZ$ -decomposition from  $n = 3$  onwards, requiring the use of the more general implementation<sup>15</sup> of a block-diagonal unitary matrix (this time, with blocks only unitary), as described in Sections 4. As further and definitive evidence of this anomalous behavior, we can check the properties under the permutation  $\prod T_1^o = P_{(2,3)}$  of all the elements involved in  $M_1^o$ , thus completing the analysis of Section 3.1.2 for the function  $h_\beta(\alpha)$ :

$$P_{(2,3)} \exp\{i\theta_5 U_5\} P_{(2,3)} = \begin{pmatrix} \cos \theta_5 & i \sin \theta_5 & 0 & 0 \\ i \sin \theta_5 & \cos \theta_5 & 0 & 0 \\ 0 & 0 & e^{i\theta_5} & 0 \\ 0 & 0 & 0 & e^{-i\theta_5} \end{pmatrix} \in M_2 ZYZ \quad (40)$$

$$P_{(2,3)} \exp\{i\theta_7 U_7\} P_{(2,3)} = \begin{pmatrix} \cos \theta_7 & \sin \theta_7 & 0 & 0 \\ -\sin \theta_7 & \cos \theta_7 & 0 & 0 \\ 0 & 0 & e^{i\theta_7} & 0 \\ 0 & 0 & 0 & e^{-i\theta_7} \end{pmatrix} \in M_2 ZYZ \quad (41)$$

$$P_{(2,3)} \exp\{i\theta_{11} U_{11}\} P_{(2,3)} = \begin{pmatrix} e^{i\theta_{11}} & 0 & 0 & 0 \\ 0 & e^{-i\theta_{11}} & 0 & 0 \\ 0 & 0 & \cos \theta_{11} & i \sin \theta_{11} \\ 0 & 0 & i \sin \theta_{11} & \cos \theta_{11} \end{pmatrix} \in M_2 ZYZ \quad (42)$$

$$P_{(2,3)} \exp\{i\theta_{14} U_{14}\} P_{(2,3)} = \begin{pmatrix} e^{i\theta_{14}} & 0 & 0 & 0 \\ 0 & e^{-i\theta_{14}} & 0 & 0 \\ 0 & 0 & \cos \theta_{14} & \sin \theta_{14} \\ 0 & 0 & -\sin \theta_{14} & \cos \theta_{14} \end{pmatrix} \in M_2 ZYZ \quad (43)$$

This behavior is then also reflected in the overall product.

Concerning the  $\Phi$ -factor, only the  $\prod T_1^o$  sub-factor remains to be analyzed; using the recipe described in Section 3.1.1 with the precaution of labeling the qubits from 0 onwards, it is straightforward to deduce the corresponding quantum circuit (see Figure 9).

Decimal	Bits	Binary	Control-Target	$k$ -index
1	$x_0$	1	(1,0)	0

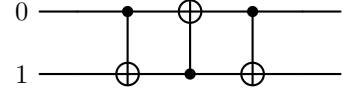


Figure 9: Diagram to find the control-target pair and the  $k$ -index for the CNOTs representing  $\prod T_1^o$ .

### 3.5 2-qubit circuit to approximate $SU(4)$

Composing the sub-circuits of the previous subsections, the overall quantum circuit to approximate every special unitary operator according to equation (5) within a QNN framework can be assembled. As will be seen from the test results, presented in Section 7, the designed QNN can be trained with only one single layer, regardless of the sparsity of the operator. This result is very interesting in comparison to the numerical simulations carried out in a complete classical context using optimization algorithms like Nelder-Mead [33]. In the following, the index layer  $l$  is set to 1 and the approximating operator can be rewritten as:

$$\begin{aligned} \mathcal{U}_{approx}(\Theta) &= Z_1(\Theta_Z) \Psi_1(\Theta_\Psi) \Phi_1(\Theta_\Phi) = \\ &= \exp\{i\theta_3 U_3\} \exp\{i\theta_8 U_8\} \exp\{i\theta_{15} U_{15}\} \exp\{i\theta_1 U_1\} \exp\{i\theta_2 U_2\} \exp\{i\theta_9 U_9\} \exp\{i\theta_{12} U_{12}\} \cdot \\ &\cdot \prod T_1^e M_1^e \prod T_1^e \prod T_1^o M_1^o \prod T_1^o = \\ &= \exp\{i\theta_3 U_3\} \exp\{i\theta_8 U_8\} \exp\{i\theta_{15} U_{15}\} \exp\{i\theta_1 U_1\} \exp\{i\theta_2 U_2\} \exp\{i\theta_9 U_9\} \exp\{i\theta_{12} U_{12}\} \cdot \\ &\cdot \left( \prod T_1^e \right) \left( \prod T_1^e \right) \exp\{i\theta_{10} U_{10}\} \exp\{i\theta_{13} U_{13}\} \exp\{i\theta_4 U_4\} \exp\{i\theta_6 U_6\} \left( \prod T_1^e \right) \left( \prod T_1^e \right) \cdot \\ &\cdot \left( \prod T_1^o \right) \left( \prod T_1^o \right) \exp\{i\theta_5 U_5\} \exp\{i\theta_7 U_7\} \exp\{i\theta_{11} U_{11}\} \exp\{i\theta_{14} U_{14}\} \left( \prod T_1^o \right) \left( \prod T_1^o \right) \end{aligned} \quad (44)$$

Finally, keeping in mind the reversed order of the factors compared to the mathematical writing, in Figure 10 the overall circuit is illustrated from left to right, line by line, taking care to label its sub-components and to

<sup>15</sup>This more general decomposition [32] still exploits  $ZYZ$ -type matrices, but adds important multi-controlled  $z$ -rotations both before and after.

point out which parts repeat identically; simplified CNOTs are marked in red. Due to its anomalous algebraic properties, it is not possible to include this case in the scalable scheme of simplifications that will be the main theme of Section 7. In Figure 11, the final quantum circuit optimized in terms of CNOT gates and capable of approximating any special unitary operator with 2 qubits is depicted for completeness.

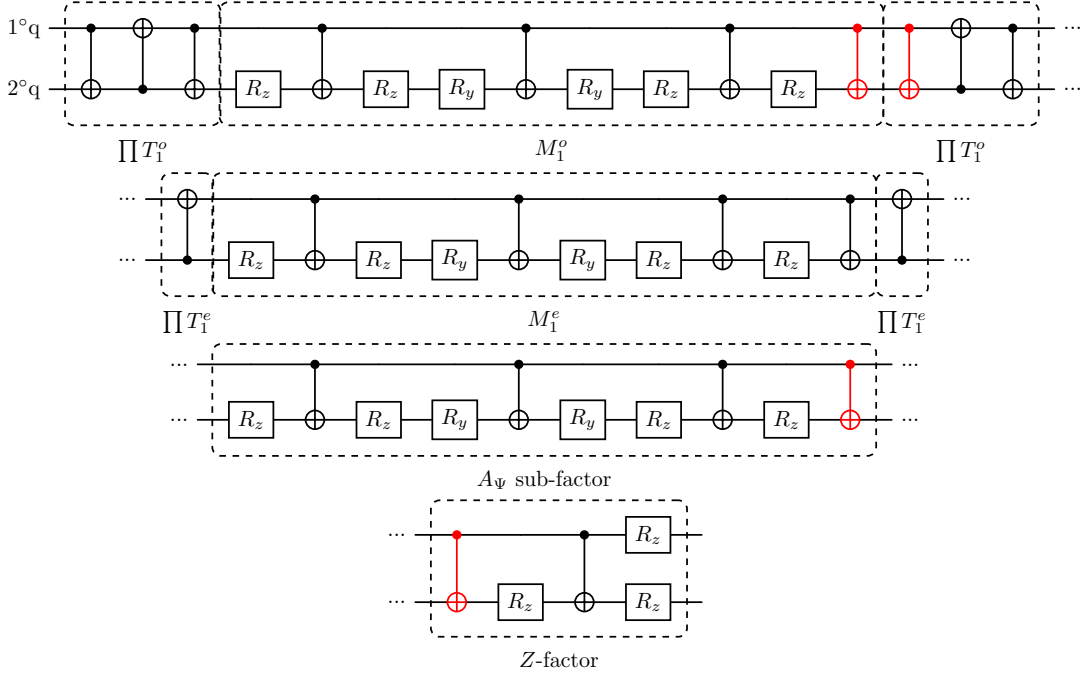


Figure 10: Quantum circuit for general 2-qubit special unitary operators; red gates are simplified gates.

## 4 Quantum circuit to approximate 3-qubit systems

According to the recursive construction of the SRBB described in Section 2.1, the design of the quantum circuit valid for any 3-qubit operator requires the matrix algebra of order 8 and, consequentially, also the algebraic bases of lower order starting from the basis  $\mathcal{U}^{(4)}$ , previously calculated in Section 3. However, unlike what was shown in Section 3 for 2 qubits, since the basis of interest has 64 matrices of order 8, it is really impractical to list each of its element or write the bases of order from 4 to 7 that build it. Precisely to overcome this inconvenience, the recursive algorithm that constructs the SRBB has been implemented, enriched with all the functions necessary to check the fundamental algebraic properties. For these reasons, only some general characteristics of the basis are provided below and useful shortcuts are proposed to manage all the elements of the algebra.

The basis  $\mathcal{B}^{(8)}$  is composed by 64 algebraic elements that describe the general evolution of an arbitrary 3-qubit quantum system. The set  $\{B_j^{(8)} : 1 \leq j \leq 63\}$  is a basis for the  $su(8)$  matrix algebra whose elements satisfy the properties of hermiticity, unitarity and zero trace:

$$\text{for } 1 \leq j \leq 63 : \quad [B_j^{(8)}]^\dagger = B_j^{(8)}, \quad [B_j^{(8)}]^2 = [B_j^{(8)}][B_j^{(8)}]^\dagger = \mathbb{I}_8, \quad \text{tr}[B_j^{(8)}] = 0 \quad (45)$$

The last element of the basis is as usual  $B_{64}^{(8)} = \mathbb{I}_8$ . Following the general formula (5) with  $l = 1$ , there are exactly:

- i) 8 diagonal elements  $B_j^{(8)}$ , belonging to the set  $\mathcal{J} = \{m^2 - 1, 2 \leq m \leq 8\} \cup \{64\} = \{3, 8, 15, 24, 35, 48, 63, 64\} = \mathcal{J}_Z \cup \{64\}$ ;
- ii) 8 elements  $B_j^{(8)}$  with a  $ZYZ$ -decomposition, divided into pairs, belonging to the set  $\mathcal{J}_\Psi = \{[(2m - 1)^2, (4m^2 - 2m)], 1 \leq m \leq 4\} = \{(1, 2), (9, 12), (25, 30), (49, 56)\}$ ;
- iii) 24 elements  $B_j^{(8)}$  divided into 6 quadruples, each of which is associated with a precise element of the set of permutations  $P_8^{even} = \{P_{(2,4)}, P_{(2,6)}, P_{(2,8)}, P_{(4,6)}, P_{(4,8)}, P_{(6,8)}\}$ , as shown in Table 3;



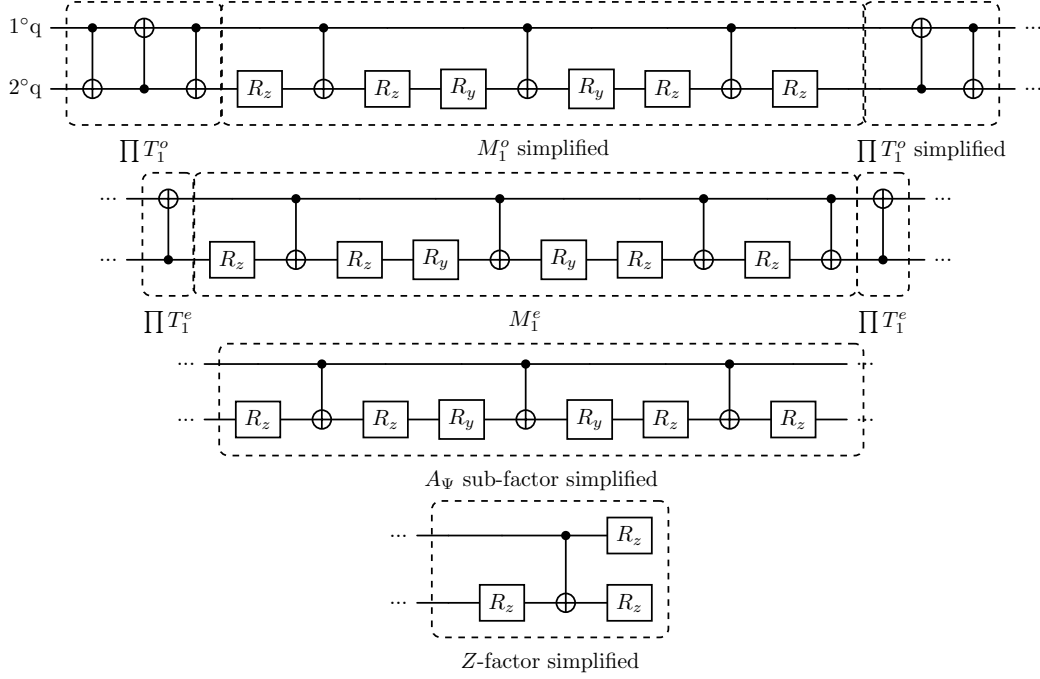


Figure 11: CNOT-optimized quantum circuit for general 2-qubit special unitary operators.

Pair	Elements
(2,4)	10,13,4,6
(2,6)	26,31,18,22
(2,8)	50,57,38,44
(4,6)	28,33,16,20
(4,8)	52,59,40,46
(6,8)	54,61,36,42

Table 3: Association between algebraic elements and even (2-cycles) permutations.

Pair	Elements
(2,3)	5,7,11,14
(2,5)	17,21,27,32
(2,7)	37,43,51,58
(4,5)	19,23,29,34
(4,7)	39,45,53,60
(6,7)	41,47,55,62

Table 4: Association between algebraic elements and odd (2-cycles) permutations.

- iv) 24 elements  $B_j^{(8)}$  divided into 6 quadruples, each of which is associated with a precise element of the set of permutations  $P_8^{odd} = \{P_{(2,3)}, P_{(2,5)}, P_{(2,7)}, P_{(4,5)}, P_{(4,7)}, P_{(6,7)}\}$ , as shown in Table 4.

A total of 64 elements is thus obtained, each taken only once except the last one (which do not participate in the generation of  $SU(8)$  matrices) and with a very specific role which will be shown in the following subsections.

The next step concerns the transition to the SRBB, namely, the replacement of the diagonal elements belonging to the set  $\mathcal{J}$  with others Hermitian unitary diagonal matrices, coming from Pauli strings. In Table 5, the replacement criterion is illustrated (for the explanation refer to Table 1). Therefore, the complete SRBB of order 8 is identified as the set  $\mathcal{U}^{(8)} = \{U_j^{(8)} : 1 \leq j \leq 64\}$  and defined by

$$U_j^{(8)} = \begin{cases} \text{new diagonal elements if } j \in \mathcal{J} = \{3, 8, 15, 24, 35, 48, 63, 64\} \\ B_j^{(8)} \text{ otherwise} \end{cases} \quad (46)$$

In order to appreciate the difference from the anomalous  $n = 2$  case and set a general rule for the scalable

Decimal	Binary	String	Matrix	Element	Replaced
0	000	$\mathbb{I}_2 \otimes \mathbb{I}_2 \otimes \mathbb{I}_2$	$\mathbb{I}_8$	64	no
1	001	$\mathbb{I}_2 \otimes \mathbb{I}_2 \otimes \sigma_3$	$diag(1, -1, 1, -1, 1, -1, 1, -1)$	3	no
2	010	$\mathbb{I}_2 \otimes \sigma_3 \otimes \mathbb{I}_2$	$diag(1, 1, -1, -1, 1, 1, -1, -1)$	8	yes
3	011	$\mathbb{I}_2 \otimes \sigma_3 \otimes \sigma_3$	$diag(1, -1, -1, 1, 1, -1, -1, 1)$	15	yes
4	100	$\sigma_3 \otimes \mathbb{I}_2 \otimes \mathbb{I}_2$	$diag(1, 1, 1, 1, -1, -1, -1, -1)$	24	yes
5	101	$\sigma_3 \otimes \mathbb{I}_2 \otimes \sigma_3$	$diag(1, -1, 1, -1, -1, 1, -1, 1)$	35	yes
6	110	$\sigma_3 \otimes \sigma_3 \otimes \mathbb{I}_2$	$diag(1, 1, -1, -1, -1, -1, 1, 1)$	48	yes
7	111	$\sigma_3 \otimes \sigma_3 \otimes \sigma_3$	$diag(1, -1, -1, 1, -1, 1, 1, -1)$	63	yes

Table 5: The new sequence of diagonal basis elements that marks the transition to SRBB.

pattern, it turns out to be very useful to analyze the algebraic properties of this basis under permutation. This analysis can be carried out following Section 3.1.2 in combination with Tables 3 and 4. At this point, the construction of the quantum circuit for the  $n = 3$  case as described by the general equation (5) can start: the three main factors will be shown first separately and then combined to highlight the simplifications of CNOTs.

#### 4.1 Diagonal contributions

In this subsection, the  $Z$ -factor (6) responsible for diagonal contributions in the  $n = 3$  case is computed and constructed<sup>16</sup>:

$$\begin{aligned}
Z(\Theta_Z) &= \prod_{j=2}^8 \exp\{i \theta_{j^2-1} U_{j^2-1}\} = \\
&= \exp\{i \theta_3 U_3\} \exp\{i \theta_8 U_8\} \exp\{i \theta_{15} U_{15}\} \exp\{i \theta_{24} U_{24}\} \exp\{i \theta_{35} U_{35}\} \exp\{i \theta_{48} U_{48}\} \exp\{i \theta_{63} U_{63}\}
\end{aligned} \tag{47}$$

In order to draw the corresponding circuit, the scheme already explained in Section 3.2 is followed. Figure 12 shows the values of the parametric pairs  $(m, m')$ , essential for designing the circuits and understanding the scalable simplification scheme. Then, the last step consists in associating each line of the previous diagram

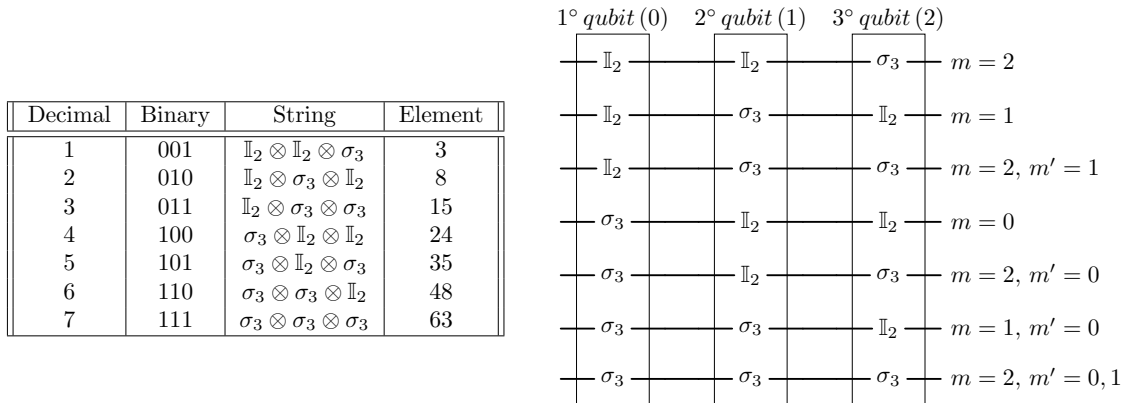


Figure 12: Diagram to find the position of CNOTs and rotation gates.

(and therefore each exponential factor considered) with one or more merged gates, following the scheme already explained in Section 3.2 (see Figure 13). Finally, Figure 14 shows the sequence of diagonal elements that minimizes the number of CNOTs, where red gates highlight the possible simplifications of CNOTs. In Section 6, this result will emerge directly from the scalable scheme that incorporates the simplifications.

#### 4.2 Even contributions

In this subsection, the  $\Psi$ -factor (7) will be analyzed and computed for a general 3-qubit system; as described in Section 2.1, it corresponds to the so called *even* contributions, which come from exponentials of a subset  $\mathcal{A}_\Psi$

<sup>16</sup>As before, the superscript  $2^n$  of each algebraic basis element is omitted for simplicity.

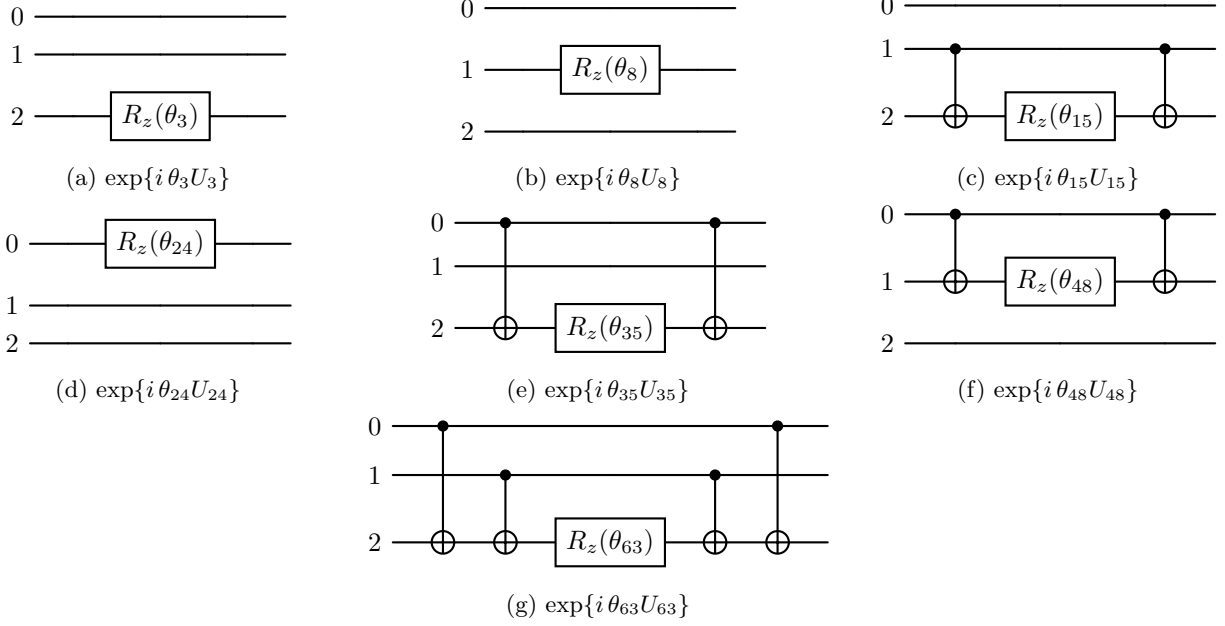


Figure 13: Seven little blocks that make up the  $Z$ -factor circuit for  $n = 3$ .

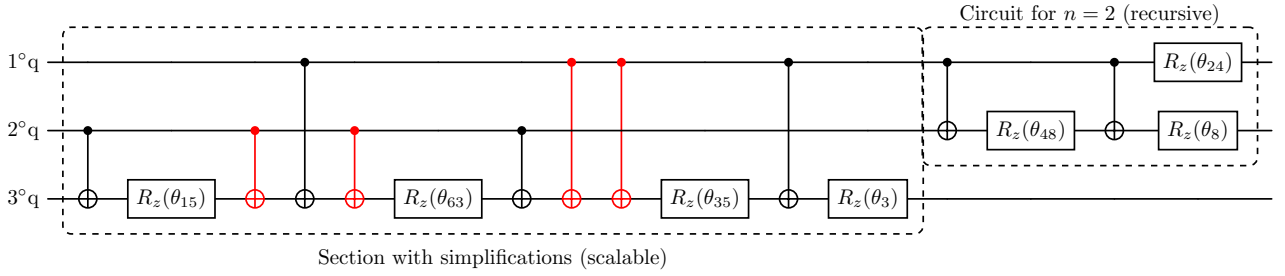


Figure 14:  $Z$ -factor quantum circuit for  $n = 3$ ; the highlighted gates simplify each other.

of SRBB elements and from permutations of exponentials of a subset  $\mathcal{B}_\Psi$  of SRBB elements:

$$\Psi(\Theta_\Psi) = \left[ \prod_{j=1}^4 \exp\{i\theta_{(2j-1)^2} U_{(2j-1)^2}\} \exp\{i\theta_{4j^2-2j} U_{4j^2-2j}\} \right] \prod_{x=1}^3 \left( \prod T_x^e \right) M_x^e \left( \prod T_x^e \right) \quad (48)$$

where

$$\prod T_1^e = P_{(2,4)} P_{(6,8)}, \quad \prod T_2^e = P_{(2,6)} P_{(4,8)}, \quad \prod T_3^e = P_{(2,8)} P_{(4,6)}, \quad (49)$$

and<sup>17</sup>

$$\begin{aligned} M_1^e &= \prod T_1^e \left[ \prod_{(2,4),(6,8)} \exp\{i\theta U_{h_\beta(\alpha-1)}\} \exp\{i\theta U_{f_\beta(\alpha-1)}\} \exp\{i\theta U_{h_{\beta-1}(\alpha)}\} \exp\{i\theta U_{f_{\beta-1}(\alpha)}\} \right] \prod T_1^e = \\ &= \prod T_1^e \left[ \exp\{i\theta U_{h_4(1)}\} \exp\{i\theta U_{f_4(1)}\} \exp\{i\theta U_{h_3(2)}\} \exp\{i\theta U_{f_3(2)}\} \cdot \right. \\ &\quad \cdot \exp\{i\theta U_{h_8(5)}\} \exp\{i\theta U_{f_8(5)}\} \exp\{i\theta U_{h_7(6)}\} \exp\{i\theta U_{f_7(6)}\} \left. \right] \prod T_1^e = \\ &= P_{(2,4)} P_{(6,8)} \left[ \exp\{i\theta U_{10}\} \exp\{i\theta U_{13}\} \exp\{i\theta U_4\} \exp\{i\theta U_6\} \cdot \right. \\ &\quad \cdot \exp\{i\theta U_{54}\} \exp\{i\theta U_{61}\} \exp\{i\theta U_{36}\} \exp\{i\theta U_{42}\} \left. \right] P_{(2,4)} P_{(6,8)} \end{aligned} \quad (50)$$

<sup>17</sup>To avoid repetitions and write compact formulas, we omit repeating the subscript for the  $\theta_i$  angles, which will still be equal to that of the associated basis elements.

$$\begin{aligned}
M_2^e &= \prod T_2^e \left[ \prod_{(2,6),(4,8)} \exp\{i\theta U_{h_\beta(\alpha-1)}\} \exp\{i\theta U_{f_\beta(\alpha-1)}\} \exp\{i\theta U_{h_{\beta-1}(\alpha)}\} \exp\{i\theta U_{f_{\beta-1}(\alpha)}\} \right] \prod T_2^e = \\
&= \prod T_2^e \left[ \exp\{i\theta U_{h_6(1)}\} \exp\{i\theta U_{f_6(1)}\} \exp\{i\theta U_{h_5(2)}\} \exp\{i\theta U_{f_5(2)}\} \cdot \right. \\
&\quad \cdot \exp\{i\theta U_{h_8(3)}\} \exp\{i\theta U_{f_8(3)}\} \exp\{i\theta U_{h_7(4)}\} \exp\{i\theta U_{f_7(4)}\} \left. \right] \prod T_2^e = \\
&= P_{(2,6)} P_{(4,8)} \left[ \exp\{i\theta U_{26}\} \exp\{i\theta U_{31}\} \exp\{i\theta U_{18}\} \exp\{i\theta U_{22}\} \cdot \right. \\
&\quad \cdot \exp\{i\theta U_{52}\} \exp\{i\theta U_{59}\} \exp\{i\theta U_{40}\} \exp\{i\theta U_{46}\} \left. \right] P_{(2,6)} P_{(4,8)}
\end{aligned} \tag{51}$$

$$\begin{aligned}
M_3^e &= \prod T_3^e \left[ \prod_{(2,8),(4,6)} \exp\{i\theta U_{h_\beta(\alpha-1)}\} \exp\{i\theta U_{f_\beta(\alpha-1)}\} \exp\{i\theta U_{h_{\beta-1}(\alpha)}\} \exp\{i\theta U_{f_{\beta-1}(\alpha)}\} \right] \prod T_3^e = \\
&= \prod T_3^e \left[ \exp\{i\theta U_{h_8(1)}\} \exp\{i\theta U_{f_8(1)}\} \exp\{i\theta U_{h_7(2)}\} \exp\{i\theta U_{f_7(2)}\} \cdot \right. \\
&\quad \cdot \exp\{i\theta U_{h_6(3)}\} \exp\{i\theta U_{f_6(3)}\} \exp\{i\theta U_{h_5(4)}\} \exp\{i\theta U_{f_5(4)}\} \left. \right] \prod T_3^e = \\
&= P_{(2,8)} P_{(4,6)} \left[ \exp\{i\theta U_{50}\} \exp\{i\theta U_{57}\} \exp\{i\theta U_{38}\} \exp\{i\theta U_{44}\} \cdot \right. \\
&\quad \cdot \exp\{i\theta U_{28}\} \exp\{i\theta U_{33}\} \exp\{i\theta U_{16}\} \exp\{i\theta U_{20}\} \left. \right] P_{(2,8)} P_{(4,6)}
\end{aligned} \tag{52}$$

The elements of the algebraic basis  $\mathcal{U}^{(8)}$  that come into play belong to the following sets:

- a set of pairs called  $\mathcal{A}_\Psi$  makes up the first sub-factor of type  $A$ ,

$$\mathcal{A}_\Psi = \{[(2m-1)^2, (4m^2-2m)], 1 \leq m \leq 4\} = \{(1, 2), (9, 12), (25, 30), (49, 56)\} \tag{53}$$

- a set of quadruples called  $\mathcal{B}_\Psi$ , divided into three subsets  $\mathcal{B}_{\Psi,x}$ , makes up the second sub-factor of type  $B$ ,

$$\mathcal{B}_\Psi = \begin{cases} \mathcal{B}_{\Psi,1} = \begin{cases} [h_4(1), f_4(1), h_3(2), f_3(2)] = (10, 13, 4, 6) \\ [h_8(5), f_8(5), h_7(6), f_7(6)] = (54, 61, 36, 42) \end{cases} \\ \mathcal{B}_{\Psi,2} = \begin{cases} [h_6(1), f_6(1), h_5(2), f_5(2)] = (26, 31, 18, 22) \\ [h_8(3), f_8(3), h_7(4), f_7(4)] = (52, 59, 40, 46) \end{cases} \\ \mathcal{B}_{\Psi,3} = \begin{cases} [h_8(1), f_8(1), h_7(2), f_7(2)] = (50, 57, 38, 44) \\ [h_6(3), f_6(3), h_5(4), f_5(4)] = (28, 33, 16, 20) \end{cases} \end{cases} \tag{54}$$

Accordingly, the first sub-factor of type  $A$  becomes a  $(2 \times 2)$ -block diagonal matrix,

$$\prod_{j \in \mathcal{A}_\Psi} \exp\{i\theta_j U_j\} = \begin{pmatrix} A_\Psi^1 & 0 & 0 & 0 \\ 0 & A_\Psi^2 & 0 & 0 \\ 0 & 0 & A_\Psi^3 & 0 \\ 0 & 0 & 0 & A_\Psi^4 \end{pmatrix} \tag{55}$$

where each block belongs to  $SU(2)$ , as can be quickly verified, thus composing as a whole a unitary matrix belonging to  $M_3ZYZ$ . In the second sub-factor of type  $B$ , factors called  $M_x^e$  are again  $(2 \times 2)$ -block diagonal matrices,

$$M_x^e = \prod T_x^e \cdot \prod_{j \in \mathcal{B}_{\Psi,x}} \exp\{i\theta_j U_j\} \cdot \prod T_x^e = \begin{pmatrix} B_{\Psi,x}^1 & 0 & 0 & 0 \\ 0 & B_{\Psi,x}^2 & 0 & 0 \\ 0 & 0 & B_{\Psi,x}^3 & 0 \\ 0 & 0 & 0 & B_{\Psi,x}^4 \end{pmatrix} \tag{56}$$

where each block belongs again to  $SU(2)$ , as can be quickly verified, thus composing as a whole another unitary matrix belonging to  $M_3ZYZ$ . The implementation of a  $M_3ZYZ$ -type matrix is always identical [32]. As previously explained, the rotation parameters are renamed as  $\theta_j^*$  because from the point of view of the variational quantum circuit the relation with algebraic elements is irrelevant. The sub-circuit for the first sub-factor of type  $A$  and for each  $M_x^e$  of the second sub-factor of type  $B$  is given by the complete decomposition of a  $M_3ZYZ$ -type matrix illustrated in Figure 15. The remaining three pairs of  $\prod T_x^e$  are not a problem from an implementation point of view if the recipe described in Section 3.1.1 (see Figure 16) is used.

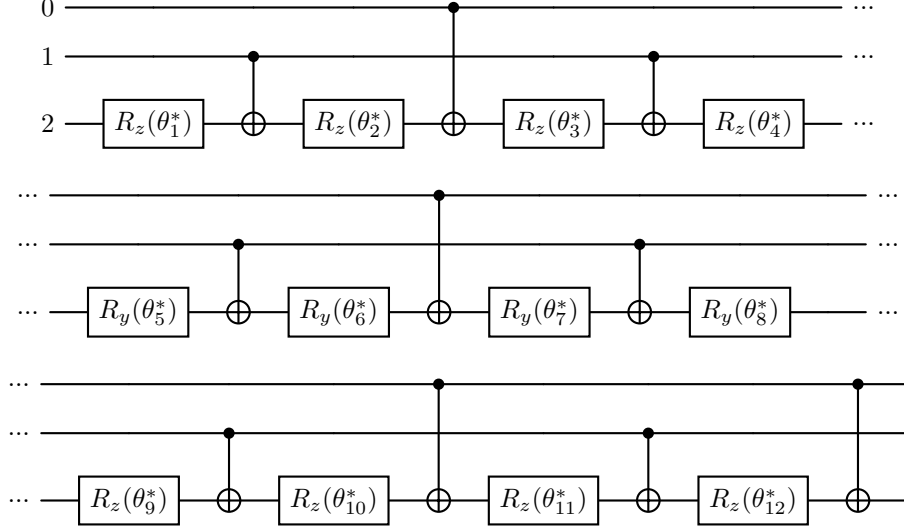


Figure 15: Fully decomposed  $M_3ZYZ$  quantum circuit.

x	Bits	Binary	Control-Target
1	$x_0x_1$	01	(2,1)
2	$x_0x_1$	10	(2,0)
3	$x_0x_1$	11	(2,0),(2,1)

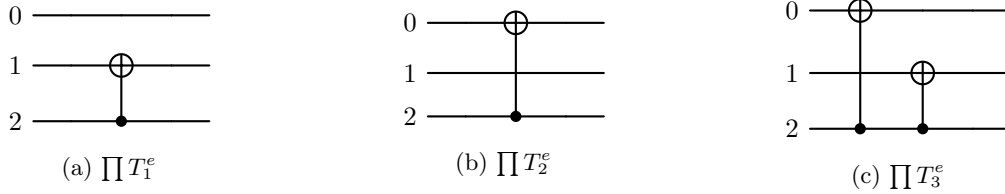


Figure 16: Diagram to find the control-target pair for the CNOTs representing  $\prod T_x^e$ .

### 4.3 Odd contributions

In this subsection, the  $\Phi$ -factor (8) will be analyzed and computed for a general 3-qubit system; as described in Section 2.1, it corresponds to the so called *odd* contributions, which come from permutations of exponentials of a subset  $\mathcal{C}_\Phi$  of SRBB elements:

$$\Phi(\Theta_\Phi) = \prod_{x=1}^3 \left( \prod T_x^o \right) M_x^o \left( \prod T_x^o \right) \quad (57)$$

where

$$\prod T_1^o = P_{(2,3)}P_{(6,7)}, \quad \prod T_2^o = P_{(2,5)}P_{(4,7)}, \quad \prod T_3^o = P_{(2,7)}P_{(4,5)}, \quad (58)$$

and<sup>18</sup>

$$\begin{aligned} M_1^o &= \prod T_1^o \left[ \prod_{(2,3),(6,7)} \exp\{i\theta U_{h_\beta(\alpha-1)}\} \exp\{i\theta U_{f_\beta(\alpha-1)}\} \exp\{i\theta U_{h_{\beta+1}(\alpha)}\} \exp\{i\theta U_{f_{\beta+1}(\alpha)}\} \right] \prod T_1^o = \\ &= \prod T_1^o \left[ \exp\{i\theta U_{h_3(1)}\} \exp\{i\theta U_{f_3(1)}\} \exp\{i\theta U_{h_4(2)}\} \exp\{i\theta U_{f_4(2)}\} \cdot \right. \\ &\quad \cdot \exp\{i\theta U_{h_7(5)}\} \exp\{i\theta U_{f_7(5)}\} \exp\{i\theta U_{h_8(6)}\} \exp\{i\theta U_{f_8(6)}\} \left. \right] \prod T_1^o = \\ &= P_{(2,3)}P_{(6,7)} \left[ \exp\{i\theta U_5\} \exp\{i\theta U_7\} \exp\{i\theta U_{11}\} \exp\{i\theta U_{14}\} \cdot \right. \\ &\quad \cdot \exp\{i\theta U_{41}\} \exp\{i\theta U_{47}\} \exp\{i\theta U_{55}\} \exp\{i\theta U_{62}\} \left. \right] P_{(2,3)}P_{(6,7)} \end{aligned} \quad (59)$$

<sup>18</sup>To avoid repetitions and write compact formulas, we omit repeating the subscript for the  $\theta_i$  angles, which will still be equal to that of the associated basis elements.

$$\begin{aligned}
M_2^o &= \prod T_2^o \left[ \prod_{(2,5),(4,7)} \exp\{i\theta U_{h_\beta(\alpha-1)}\} \exp\{i\theta U_{f_\beta(\alpha-1)}\} \exp\{i\theta U_{h_{\beta+1}(\alpha)}\} \exp\{i\theta U_{f_{\beta+1}(\alpha)}\} \right] \prod T_2^o = \\
&= \prod T_2^o \left[ \exp\{i\theta U_{h_5(1)}\} \exp\{i\theta U_{f_5(1)}\} \exp\{i\theta U_{h_6(2)}\} \exp\{i\theta U_{f_6(2)}\} \cdot \right. \\
&\quad \cdot \exp\{i\theta U_{h_7(3)}\} \exp\{i\theta U_{f_7(3)}\} \exp\{i\theta U_{h_8(4)}\} \exp\{i\theta U_{f_8(4)}\} \left. \right] \prod T_2^o = \\
&= P_{(2,5)} P_{(4,7)} \left[ \exp\{i\theta U_{17}\} \exp\{i\theta U_{21}\} \exp\{i\theta U_{27}\} \exp\{i\theta U_{32}\} \cdot \right. \\
&\quad \cdot \exp\{i\theta U_{39}\} \exp\{i\theta U_{45}\} \exp\{i\theta U_{53}\} \exp\{i\theta U_{60}\} \left. \right] P_{(2,5)} P_{(4,7)}
\end{aligned} \tag{60}$$

$$\begin{aligned}
M_3^o &= \prod T_3^o \left[ \prod_{(2,7),(4,5)} \exp\{i\theta U_{h_\beta(\alpha-1)}\} \exp\{i\theta U_{f_\beta(\alpha-1)}\} \exp\{i\theta U_{h_{\beta+1}(\alpha)}\} \exp\{i\theta U_{f_{\beta+1}(\alpha)}\} \right] \prod T_3^o = \\
&= \prod T_3^o \left[ \exp\{i\theta U_{h_7(1)}\} \exp\{i\theta U_{f_7(1)}\} \exp\{i\theta U_{h_8(2)}\} \exp\{i\theta U_{f_8(2)}\} \cdot \right. \\
&\quad \cdot \exp\{i\theta U_{h_5(3)}\} \exp\{i\theta U_{f_5(3)}\} \exp\{i\theta U_{h_6(4)}\} \exp\{i\theta U_{f_6(4)}\} \left. \right] \prod T_3^o = \\
&= P_{(2,7)} P_{(4,5)} \left[ \exp\{i\theta U_{37}\} \exp\{i\theta U_{43}\} \exp\{i\theta U_{51}\} \exp\{i\theta U_{58}\} \cdot \right. \\
&\quad \cdot \exp\{i\theta U_{19}\} \exp\{i\theta U_{23}\} \exp\{i\theta U_{29}\} \exp\{i\theta U_{34}\} \left. \right] P_{(2,7)} P_{(4,5)}
\end{aligned} \tag{61}$$

The elements of the algebraic basis  $\mathcal{U}^{(8)}$  that come into play belong to the following set of quadruples called  $\mathcal{C}_\Phi$ , divided into three subsets  $\mathcal{C}_{\Phi,x}$ :

$$\mathcal{C}_\Phi = \begin{cases} \mathcal{C}_{\Phi,1} = \begin{cases} [h_3(1), f_3(1), h_4(2), f_4(2)] = (5, 7, 11, 14) \\ [h_7(5), f_7(5), h_8(6), f_8(6)] = (41, 47, 55, 62) \end{cases} \\ \mathcal{C}_{\Phi,2} = \begin{cases} [h_5(1), f_5(1), h_6(2), f_6(2)] = (17, 21, 27, 32) \\ [h_7(3), f_7(3), h_8(4), f_8(4)] = (39, 45, 53, 60) \end{cases} \\ \mathcal{C}_{\Phi,3} = \begin{cases} [h_7(1), f_7(1), h_8(2), f_8(2)] = (37, 43, 51, 58) \\ [h_5(3), f_5(3), h_6(4), f_6(4)] = (19, 23, 29, 34) \end{cases} \end{cases} \tag{62}$$

Accordingly,  $M_x^o$  factors become  $2 \times 2$ -block diagonal matrices,

$$M_x^o = \prod T_x^o \cdot \prod_{i \in \mathcal{C}_{\Phi,x}} \exp\{i\theta_i U_i\} \cdot \prod T_x^o = \begin{pmatrix} C_{\Phi,x}^1 & 0 & 0 & 0 \\ 0 & C_{\Phi,x}^2 & 0 & 0 \\ 0 & 0 & C_{\Phi,x}^3 & 0 \\ 0 & 0 & 0 & C_{\Phi,x}^4 \end{pmatrix} \tag{63}$$

where each block no longer belongs to  $SU(2)$ , but only to  $U(2)$ , thus composing as a whole a unitary matrix that can be decomposed only in part through a  $M_3 ZY Z$  [32]. Exploiting the unitary (phase) scaling that exists between  $U(n)$  and  $SU(n)$ , the circuit for  $M_x^o$  is given in Figure 17.

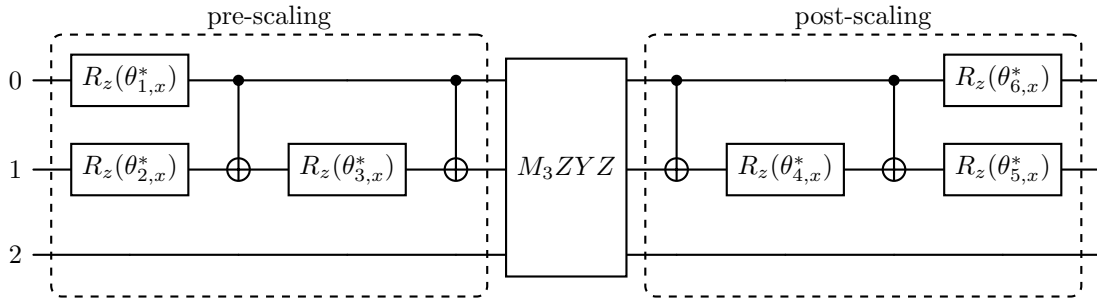


Figure 17: Quantum circuit for  $M_x^o$  factors; a  $ZYZ$ -core is surrounded by multi-controlled rotations.

Therefore, for  $n = 3$ , the scalability scheme proposed by [33] begins to hold, justified by the algebraic properties under permutation shown by equations (59), (60), (61). The remaining three pairs of  $\prod T_x^o$  can be implemented thanks to the recipe described in Section 3.1.1 (see Figure 18).

#### 4.4 3-qubit circuit to approximate $SU(8)$

Composing the sub-circuits of the previous subsections, the overall quantum circuit to approximate every special unitary operator according to the equation (5) within a QNN framework can be assembled. As for

x	Bits	Binary	Control-Target	k-index
1	$x_0x_1$	01	(2,1)	1
2	$x_0x_1$	10	(2,0)	0
3	$x_0x_1$	11	(2,0),(2,1)	0

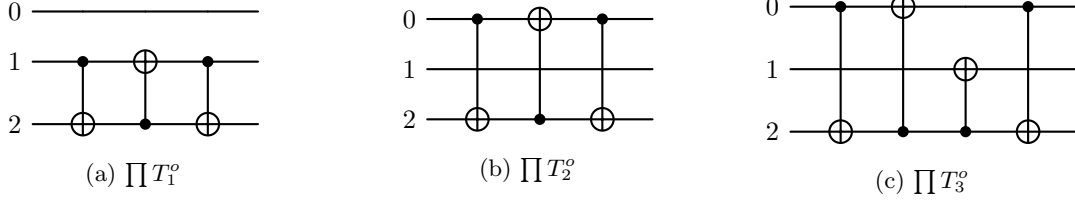


Figure 18: Diagram to find the control-target pair and the  $k$ -index for the CNOTs representing  $\prod T_x^o$ .

2-qubit systems, the approximating operator can be rewritten in the following way:

$$\begin{aligned}
\mathcal{U}_{approx}(\Theta) &= Z_1(\Theta_Z) \Psi_1(\Theta_\Psi) \Phi_1(\Theta_\Phi) = \\
&= \exp\{i\theta_3U_3\} \exp\{i\theta_8U_8\} \exp\{i\theta_{15}U_{15}\} \exp\{i\theta_{24}U_{24}\} \exp\{i\theta_{35}U_{35}\} \exp\{i\theta_{48}U_{48}\} \exp\{i\theta_{63}U_{63}\} \cdot \\
&\cdot \exp\{i\theta_1U_1\} \exp\{i\theta_2U_2\} \exp\{i\theta_9U_9\} \exp\{i\theta_{12}U_{12}\} \exp\{i\theta_{25}U_{25}\} \exp\{i\theta_{30}U_{30}\} \exp\{i\theta_{49}U_{49}\} \exp\{i\theta_{56}U_{56}\} \cdot \\
&\cdot \left(\prod T_1^e\right) M_1^e \left(\prod T_1^e\right) \left(\prod T_2^e\right) M_2^e \left(\prod T_2^e\right) \left(\prod T_3^e\right) M_3^e \left(\prod T_3^e\right) \cdot \\
&\cdot \left(\prod T_1^o\right) M_1^o \left(\prod T_1^o\right) \left(\prod T_2^o\right) M_2^o \left(\prod T_2^o\right) \left(\prod T_3^o\right) M_3^o \left(\prod T_3^o\right) = \\
&= \prod_{i \in \mathcal{J}_Z} \exp\{i\theta_i U_i\} \prod_{j \in \mathcal{A}_\Psi} \exp\{i\theta_j U_j\} \prod_{x=1}^3 \left[ \left(\prod T_x^e\right) \left(\prod T_x^e\right) \prod_{k_e \in \mathcal{B}_{\Psi,x}} \exp\{i\theta_{k_e} U_{k_e}\} \left(\prod T_x^e\right) \left(\prod T_x^e\right) \right] \cdot \\
&\cdot \prod_{x=1}^3 \left[ \left(\prod T_x^o\right) \left(\prod T_x^o\right) \prod_{k_o \in \mathcal{C}_{\Phi,x}} \exp\{i\theta_{k_o} U_{k_o}\} \left(\prod T_x^o\right) \left(\prod T_x^o\right) \right] = \\
&= \prod_{i \in \mathcal{J}_Z} \exp\{i\theta_i U_i\} \prod_{j \in \mathcal{A}_\Psi} \exp\{i\theta_j U_j\} \prod_{k_e \in \mathcal{B}_{\Psi,1}} \exp\{i\theta_{k_e} U_{k_e}\} \prod_{l_e \in \mathcal{B}_{\Psi,2}} \exp\{i\theta_{l_e} U_{l_e}\} \prod_{m_e \in \mathcal{B}_{\Psi,3}} \exp\{i\theta_{m_e} U_{m_e}\} \cdot \\
&\cdot \prod_{k_o \in \mathcal{C}_{\Phi,1}} \exp\{i\theta_{k_o} U_{k_o}\} \prod_{l_o \in \mathcal{C}_{\Phi,2}} \exp\{i\theta_{l_o} U_{l_o}\} \prod_{m_o \in \mathcal{C}_{\Phi,3}} \exp\{i\theta_{m_o} U_{m_o}\}
\end{aligned} \tag{64}$$

The last equality is due to the properties of permutation matrices and reveals the crucial role of grouping (and then ordering). Finally, keeping in mind the reversed order of the factors compared to the mathematical writing, in Figure 19 the overall quantum circuit is depicted from left to right, line by line, taking care to label its sub-components. This figure also highlights which parts of the quantum circuit repeat identically for this particular case  $n = 3$ . It is possible to immediately notice which CNOTs are simplified (red gates). Eliminating these latter, the final CNOT-optimized quantum circuit capable of approximating any special unitary operator with 3 qubits is found.

## 5 Quantum circuit to approximate 4-qubit systems

As required by the SRBB, the design of the quantum circuit valid for any 4-qubit operator requires the matrix algebra of order 16, which contains 256 elements (see Section 2.1 about the recursive construction); clearly, unlike what was done for  $n = 3$ , reporting the entire basis is an impractical and time-consuming task. Furthermore, since for  $n \geq 3$  the properties of the algebraic elements guarantee the same scalable structure in terms of grouping and ordering, for  $n = 4$  only some intermediate steps will be shown to correctly manage the approximation formula in light of the increased number of its elements. It is useful to point out that these analysis shortcuts summarize the fundamental steps of circuit design for any value of  $n$ .

The basis  $\mathcal{B}^{(16)}$  is composed by 256 algebraic elements that can describe the general evolution of an arbitrary 4-qubit quantum system. The set  $\{B_j^{(16)} : 1 \leq j \leq 255\}$  is a basis for the  $su(16)$  matrix algebra whose elements

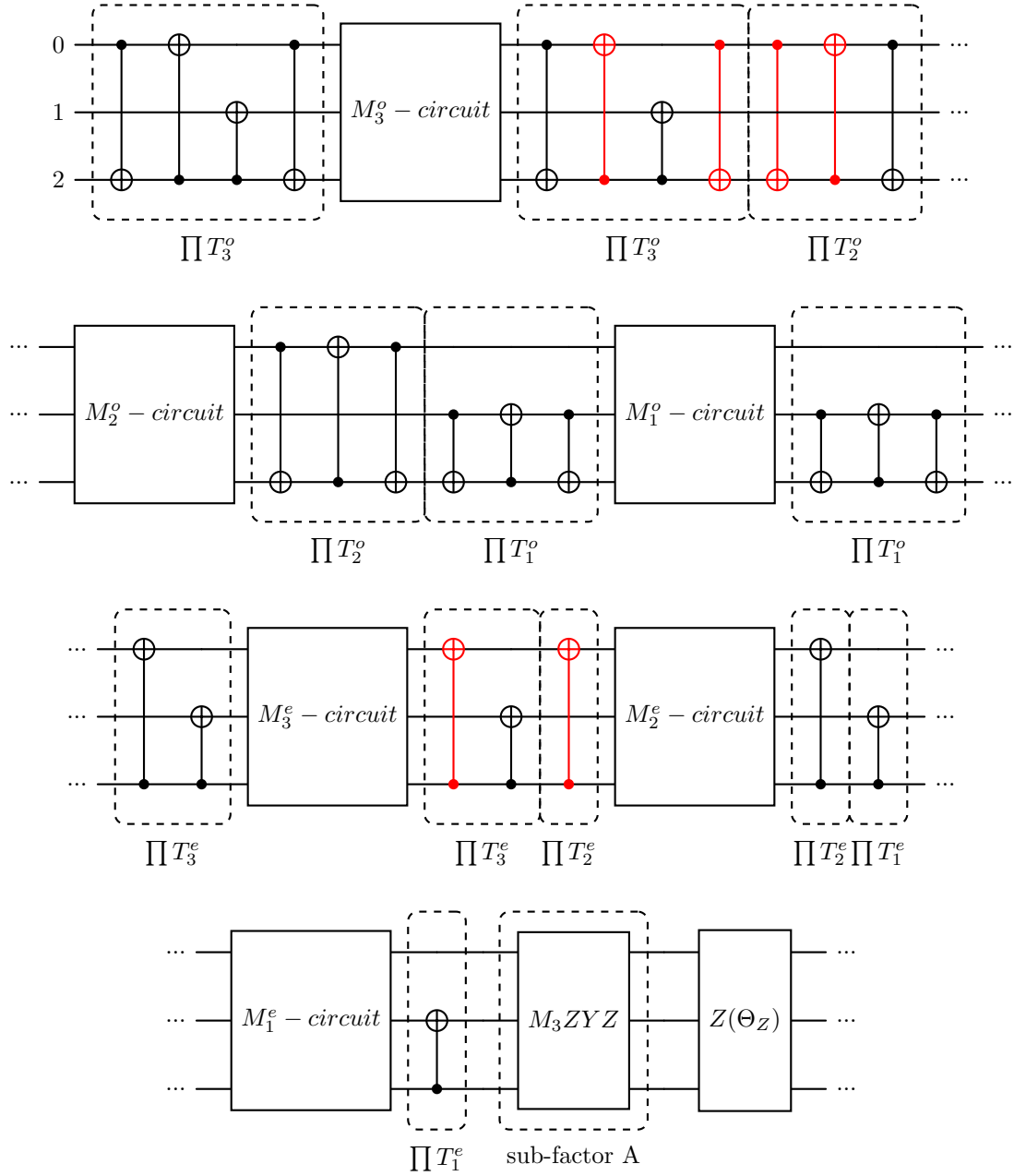


Figure 19: Quantum circuit for general 3-qubit special unitary operators.



satisfy the properties of hermiticity, unitarity and zero trace:

$$\text{for } 1 \leq j \leq 255 : \quad [B_j^{(16)}]^\dagger = B_j^{(16)}, \quad [B_j^{(16)}]^2 = [B_j^{(16)}][B_j^{(16)}]^\dagger = \mathbb{I}_{16}, \quad \text{tr}[B_j^{(16)}] = 0 \quad (65)$$

The last element of the basis is, as usual,  $B_{256}^{(16)} = \mathbb{I}_{16}$ . Following the general formula (5) with  $l = 1$ , there are exactly:

- i) 16 diagonal elements  $B_j^{(16)}$ , belonging to the set  $\mathcal{J} = \{m^2 - 1, 2 \leq m \leq 16\} \cup \{256\} = \{3, 8, 15, 24, 35, 48, 63, 80, 99, 120, 143, 168, 195, 224, 255, 256\} = \mathcal{J}_Z \cup \{256\}$ ;
- ii) 16 elements  $B_j^{(16)}$  with a  $ZYZ$ -decomposition, divided into pairs, belonging to the set  $\mathcal{J}_\Psi = \{[(2m-1)^2, (4m^2-2m)], 1 \leq m \leq 8\} = \{(1, 2), (9, 12), (25, 30), (49, 56), (81, 90), (121, 132), (169, 182), (225, 240)\}$ ;
- iii) 112 elements  $B_j^{(16)}$  divided into 28 quadruples, each of which is associated with a precise 2-cycle of the set of permutations  $P_{16}^{even}$ , as shown in Table 6. For brevity, only the elements associated with the first row of Table 6 are reported in Table 7.

$P_{(2,4)}$	$P_{(2,6)}$	$P_{(2,8)}$	$P_{(2,10)}$	$P_{(2,12)}$	$P_{(2,14)}$	$P_{(2,16)}$
	$P_{(4,6)}$	$P_{(4,8)}$	$P_{(4,10)}$	$P_{(4,12)}$	$P_{(4,14)}$	$P_{(4,16)}$
		$P_{(6,8)}$	$P_{(6,10)}$	$P_{(6,12)}$	$P_{(6,14)}$	$P_{(6,16)}$
			$P_{(8,10)}$	$P_{(8,12)}$	$P_{(8,14)}$	$P_{(8,16)}$
				$P_{(10,12)}$	$P_{(10,14)}$	$P_{(10,16)}$
					$P_{(12,14)}$	$P_{(12,16)}$
						$P_{(14,16)}$

Table 6: Elements of the 2-cycle group  $P_{16}^{even}$ .

Pair	Functions	Elements
(2,4)	$h_4(1), f_4(1), h_3(2), f_3(2)$	10,13,4,6
(2,6)	$h_6(1), f_6(1), h_5(2), f_5(2)$	26,31,18,22
(2,8)	$h_8(1), f_8(1), h_7(2), f_7(2)$	50,57,38,44
(2,10)	$h_{10}(1), f_{10}(1), h_9(2), f_9(2)$	82,91,66,74
(2,12)	$h_{12}(1), f_{12}(1), h_{11}(2), f_{11}(2)$	122,133,102,112
(2,14)	$h_{14}(1), f_{14}(1), h_{13}(2), f_{13}(2)$	170,184,146,158
(2,16)	$h_{16}(1), f_{16}(1), h_{15}(2), f_{15}(2)$	226,241,198,212

Table 7: Association between algebraic elements and even (2-cycles) permutations.

- iv) 112 elements  $B_j^{(16)}$  divided into 28 quadruples, each of which is associated with a precise element of the set of permutations  $P_{16}^{odd}$ , as shown in Table 8. Again, only the elements associated with the first row of Table 8 are reported in Table 9.

$P_{(2,3)}$	$P_{(2,5)}$	$P_{(2,7)}$	$P_{(2,9)}$	$P_{(2,11)}$	$P_{(2,13)}$	$P_{(2,15)}$
	$P_{(4,5)}$	$P_{(4,7)}$	$P_{(4,9)}$	$P_{(4,11)}$	$P_{(4,13)}$	$P_{(4,15)}$
		$P_{(6,7)}$	$P_{(6,9)}$	$P_{(6,11)}$	$P_{(6,13)}$	$P_{(6,15)}$
			$P_{(8,9)}$	$P_{(8,11)}$	$P_{(8,13)}$	$P_{(8,15)}$
				$P_{(10,11)}$	$P_{(10,13)}$	$P_{(10,15)}$
					$P_{(12,13)}$	$P_{(12,15)}$
						$P_{(14,15)}$

Table 8: Elements of the 2-cycle group  $P_{16}^{odd}$ .

A total of 256 elements is thus obtained, each taken only once except the last one (which do not participate in the generation of  $SU(16)$  matrices) and with a very peculiar role in the approximation.

The next step concerns the transition to the SRBB, namely, the replacement of the diagonal elements belonging to the set  $\mathcal{J}$  with others Hermitian unitary diagonal matrices, generated starting from Pauli string;

Pair	Functions	Elements
(2,3)	$h_3(1), f_3(1), h_4(2), f_4(2)$	5,7,11,14
(2,5)	$h_5(1), f_5(1), h_6(2), f_6(2)$	17,21,27,32
(2,7)	$h_7(1), f_7(1), h_8(2), f_8(2)$	37,43,51,58
(2,9)	$h_9(1), f_9(1), h_{10}(2), f_{10}(2)$	65,73,83,92
(2,11)	$h_{11}(1), f_{11}(1), h_{12}(2), f_{12}(2)$	101,111,123,134
(2,13)	$h_{13}(1), f_{13}(1), h_{14}(2), f_{14}(2)$	145,157,171,184
(2,15)	$h_{15}(1), f_{15}(1), h_{16}(2), f_{16}(2)$	197,211,227,242

Table 9: Association between algebraic elements and odd (2-cycles) permutations.

Decimal	Binary	String	Element
0	0000	$\mathbb{I}_2 \otimes \mathbb{I}_2 \otimes \mathbb{I}_2 \otimes \mathbb{I}_2$	256
1	0001	$\mathbb{I}_2 \otimes \mathbb{I}_2 \otimes \mathbb{I}_2 \otimes \sigma_3$	3
2	0010	$\mathbb{I}_2 \otimes \mathbb{I}_2 \otimes \sigma_3 \otimes \mathbb{I}_2$	8
3	0011	$\mathbb{I}_2 \otimes \mathbb{I}_2 \otimes \sigma_3 \otimes \sigma_3$	15
4	0100	$\mathbb{I}_2 \otimes \sigma_3 \otimes \mathbb{I}_2 \otimes \mathbb{I}_2$	24
5	0101	$\mathbb{I}_2 \otimes \sigma_3 \otimes \mathbb{I}_2 \otimes \sigma_3$	35
6	0110	$\mathbb{I}_2 \otimes \sigma_3 \otimes \sigma_3 \otimes \mathbb{I}_2$	48
7	0111	$\mathbb{I}_2 \otimes \sigma_3 \otimes \sigma_3 \otimes \sigma_3$	63
8	1000	$\sigma_3 \otimes \mathbb{I}_2 \otimes \mathbb{I}_2 \otimes \mathbb{I}_2$	80
9	1001	$\sigma_3 \otimes \mathbb{I}_2 \otimes \mathbb{I}_2 \otimes \sigma_3$	99
10	1010	$\sigma_3 \otimes \mathbb{I}_2 \otimes \sigma_3 \otimes \mathbb{I}_2$	120
11	1011	$\sigma_3 \otimes \mathbb{I}_2 \otimes \sigma_3 \otimes \sigma_3$	143
12	1100	$\sigma_3 \otimes \sigma_3 \otimes \mathbb{I}_2 \otimes \mathbb{I}_2$	168
13	1101	$\sigma_3 \otimes \sigma_3 \otimes \mathbb{I}_2 \otimes \sigma_3$	195
14	1110	$\sigma_3 \otimes \sigma_3 \otimes \sigma_3 \otimes \mathbb{I}_2$	224
15	1111	$\sigma_3 \otimes \sigma_3 \otimes \sigma_3 \otimes \sigma_3$	255

Table 10: The new sequence of diagonal basis elements that marks the transition to SRBB.

Table 10 shows the list of new diagonal elements. Therefore, the complete SRBB of order 16 is identified as the set  $\mathcal{U}^{(16)} = \{U_j^{(16)} : 1 \leq j \leq 256\}$  and defined by

$$U_j^{(16)} = \begin{cases} \text{new diagonal elements if } j \in \mathcal{J} \\ B_j^{(16)} \text{ otherwise} \end{cases} \quad (66)$$

In the following subsections, the design of the quantum circuit for  $n = 4$  is explained following the general equation (5) and, as usual, starting from the analysis of its three main factors. In order to show how the scaling characteristics help in circuit design for any value of  $n$ , the analysis will follow the same procedure already described in Section 4.

## 5.1 Diagonal contributions

In this subsection, the  $Z$ -factor (6) responsible for diagonal contributions in the  $n = 4$  case is briefly analyzed to show the most relevant aspects of its design<sup>19</sup>:

$$Z(\Theta_Z) = \prod_{j=2}^{16} \exp\{i\theta_{j^2-1}U_{j^2-1}\} = \prod_{j \in \mathcal{J}_Z} \exp\{i\theta_j U_j\} \quad (67)$$

With the aim of designing the corresponding circuit, the scheme already explained in Section 3 is followed. Figure 20 shows the values of the parametric pairs  $(m, m')$ , with reference to Table 10. Finally, the last step consists in associating each line of Figure 20 with one or more merged gates, following the scheme already explained in Section 3 (see Figure 21). The sequence of diagonal elements that minimizes the number of CNOTs is depicted in Figure 22, where the red gates highlight the possible simplifications of CNOTs. In Section 6, the CNOT-optimized circuit will emerge from the scalable algorithm of simplifications.

<sup>19</sup>As before, the superscript  $2^n$  of each algebraic basis element is omitted for simplicity.

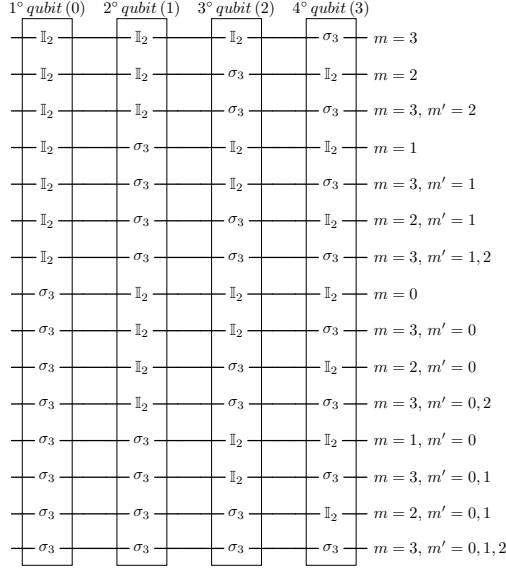


Figure 20: Diagram to find the position of CNOTs and rotation gates.

## 5.2 Even contributions

In this subsection, the  $\Psi$ -factor (7) will be briefly analyzed for a general 4-qubit system; below, the sub-factors that compose it and its properties are described following the same scheme as in Section 4.2.

$$\Psi(\Theta_\Psi) = \left[ \prod_{j=1}^8 \exp\{i\theta_{(2j-1)^2} U_{(2j-1)^2}\} \exp\{i\theta_{4j^2-2j} U_{4j^2-2j}\} \right] \prod_{x=1}^7 \left( \prod T_x^e \right) M_x^e \left( \prod T_x^e \right) \quad (68)$$

where

$$\begin{aligned} \prod T_1^e &= P_{(2,4)} P_{(14,16)} P_{(12,16)} P_{(12,14)} \\ \prod T_2^e &= P_{(2,6)} P_{(10,16)} P_{(10,14)} P_{(10,12)} \\ \prod T_3^e &= P_{(2,8)} P_{(6,16)} P_{(6,14)} P_{(6,12)} \\ \prod T_4^e &= P_{(2,10)} P_{(8,16)} P_{(8,14)} P_{(8,12)} \\ \prod T_5^e &= P_{(2,12)} P_{(8,10)} P_{(6,10)} P_{(6,8)} \\ \prod T_6^e &= P_{(2,14)} P_{(4,16)} P_{(4,12)} P_{(4,10)} \\ \prod T_7^e &= P_{(2,16)} P_{(4,14)} P_{(4,8)} P_{(4,6)} \end{aligned} \quad (69)$$

For practical reasons, only  $M_{1,2,3}^e$  are reported below given that the construction of the remaining ones is identical<sup>20</sup>.

$$\begin{aligned} M_1^e &= \prod T_1^e \left[ \prod_{\substack{(2,4), (14,16), \\ (12,16), (12,14)}} \exp\{i\theta U_{h_\beta(\alpha-1)}\} \exp\{i\theta U_{f_\beta(\alpha-1)}\} \exp\{i\theta U_{h_{\beta-1}(\alpha)}\} \exp\{i\theta U_{f_{\beta-1}(\alpha)}\} \right] \prod T_1^e = \\ &= \prod T_1^e \left[ \exp\{i\theta U_{h_4(1)}\} \exp\{i\theta U_{f_4(1)}\} \exp\{i\theta U_{h_3(2)}\} \exp\{i\theta U_{f_3(2)}\} \cdot \right. \\ &\cdot \exp\{i\theta U_{h_{16}(13)}\} \exp\{i\theta U_{f_{16}(13)}\} \exp\{i\theta U_{h_{15}(14)}\} \exp\{i\theta U_{f_{15}(14)}\} \cdot \\ &\cdot \exp\{i\theta U_{h_{16}(11)}\} \exp\{i\theta U_{f_{16}(11)}\} \exp\{i\theta U_{h_{15}(12)}\} \exp\{i\theta U_{f_{15}(12)}\} \cdot \\ &\left. \cdot \exp\{i\theta U_{h_{14}(11)}\} \exp\{i\theta U_{f_{14}(11)}\} \exp\{i\theta U_{h_{13}(12)}\} \exp\{i\theta U_{f_{13}(12)}\} \right] \prod T_1^e \end{aligned} \quad (70)$$

<sup>20</sup>To avoid repetitions and write compact formulas, we omit repeating the subscript for the  $\theta_i$  angles, which will still be equal to that of the associated basis elements.

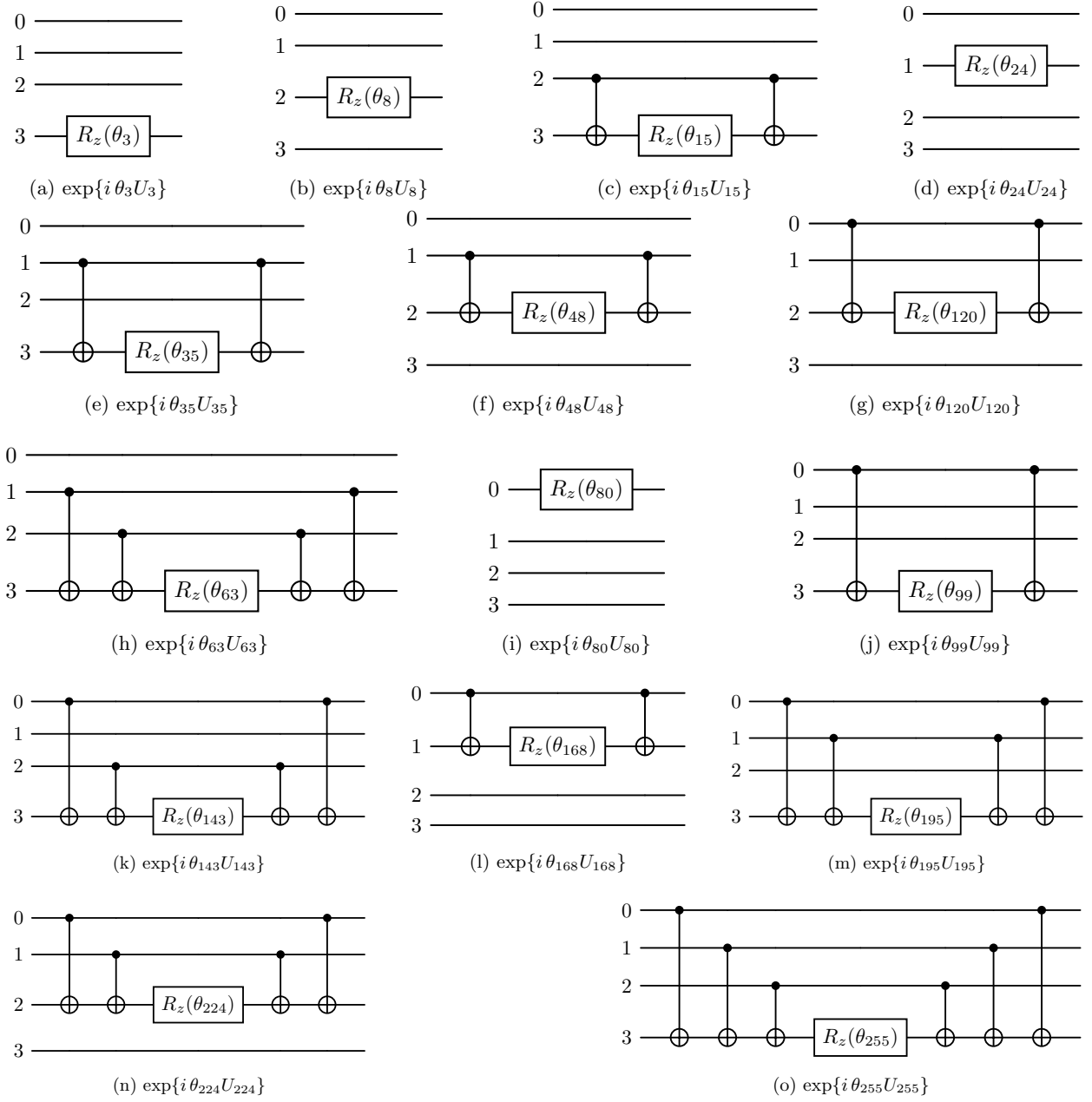


Figure 21: Fifteen little blocks that make up the  $Z$ -factor circuit for  $n = 4$ .

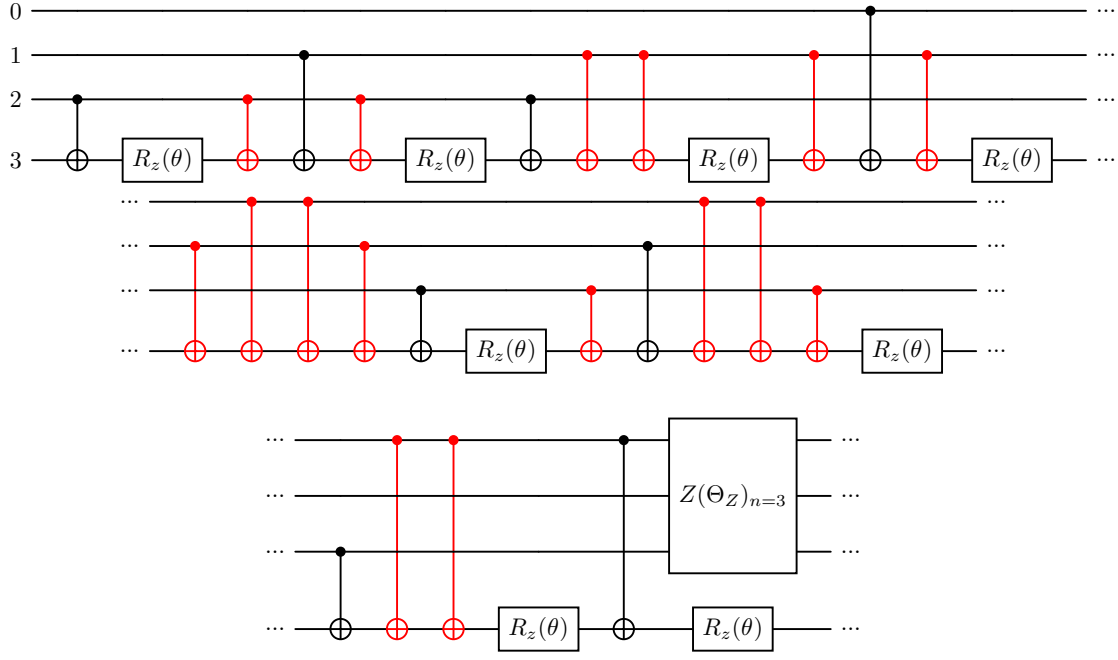


Figure 22:  $Z$ -factor quantum circuit for  $n = 4$ ; the highlighted gates simplify each other.

$$\begin{aligned}
M_2^e &= \prod T_2^e \left[ \prod_{\substack{(2,6), (10,16), \\ (10,14), (10,12)}} \exp\{i\theta U_{h_\beta(\alpha-1)}\} \exp\{i\theta U_{f_\beta(\alpha-1)}\} \exp\{i\theta U_{h_{\beta-1}(\alpha)}\} \exp\{i\theta U_{f_{\beta-1}(\alpha)}\} \right] \prod T_2^e = \\
&= \prod T_2^e \left[ \exp\{i\theta U_{h_6(1)}\} \exp\{i\theta U_{f_6(1)}\} \exp\{i\theta U_{h_5(2)}\} \exp\{i\theta U_{f_5(2)}\} \cdot \right. \\
&\cdot \exp\{i\theta U_{h_{16}(9)}\} \exp\{i\theta U_{f_{16}(9)}\} \exp\{i\theta U_{h_{15}(10)}\} \exp\{i\theta U_{f_{15}(10)}\} \cdot \\
&\cdot \exp\{i\theta U_{h_{14}(9)}\} \exp\{i\theta U_{f_{14}(9)}\} \exp\{i\theta U_{h_{13}(10)}\} \exp\{i\theta U_{f_{13}(10)}\} \cdot \\
&\cdot \left. \exp\{i\theta U_{h_{12}(9)}\} \exp\{i\theta U_{f_{12}(9)}\} \exp\{i\theta U_{h_{11}(10)}\} \exp\{i\theta U_{f_{11}(10)}\} \right] \prod T_2^e
\end{aligned} \tag{71}$$

$$\begin{aligned}
M_3^e &= \prod T_3^e \left[ \prod_{\substack{(2,8), (6,16), \\ (6,14), (6,12)}} \exp\{i\theta U_{h_\beta(\alpha-1)}\} \exp\{i\theta U_{f_\beta(\alpha-1)}\} \exp\{i\theta U_{h_{\beta-1}(\alpha)}\} \exp\{i\theta U_{f_{\beta-1}(\alpha)}\} \right] \prod T_3^e = \\
&= \prod T_3^e \left[ \exp\{i\theta U_{h_8(1)}\} \exp\{i\theta U_{f_8(1)}\} \exp\{i\theta U_{h_7(2)}\} \exp\{i\theta U_{f_7(2)}\} \cdot \right. \\
&\cdot \exp\{i\theta U_{h_{16}(5)}\} \exp\{i\theta U_{f_{16}(5)}\} \exp\{i\theta U_{h_{15}(6)}\} \exp\{i\theta U_{f_{15}(6)}\} \cdot \\
&\cdot \exp\{i\theta U_{h_{14}(5)}\} \exp\{i\theta U_{f_{14}(5)}\} \exp\{i\theta U_{h_{13}(6)}\} \exp\{i\theta U_{f_{13}(6)}\} \cdot \\
&\cdot \left. \exp\{i\theta U_{h_{12}(5)}\} \exp\{i\theta U_{f_{12}(5)}\} \exp\{i\theta U_{h_{11}(6)}\} \exp\{i\theta U_{f_{11}(6)}\} \right] \prod T_3^e
\end{aligned} \tag{72}$$

The elements of the algebraic basis  $\mathcal{U}^{(16)}$  that come into play belong to the following sets:

- a set of pairs called  $\mathcal{A}_\Psi$  makes up the first sub-factor of type  $A$ ,

$$\begin{aligned}
\mathcal{A}_\Psi &= \{[(2m-1)^2, (4m^2-2m)], 1 \leq m \leq 8\} = \\
&= \{(1, 2), (9, 12), (25, 30), (49, 56), (81, 90), (121, 132), (169, 182), (225, 240)\}
\end{aligned} \tag{73}$$

- a set of quadruples called  $\mathcal{B}_\Psi$ , divided into seven subsets  $\mathcal{B}_{\Psi,x}$ , makes up the second sub-factor of type  $B$ ,

$$\begin{aligned}
\mathcal{B}_{\Psi,1} &= \begin{cases} [h_4(1), f_4(1), h_3(2), f_3(2)] \\ [h_{16}(13), f_{16}(13), h_{15}(14), f_{15}(14)] \\ [h_{16}(11), f_{16}(11), h_{15}(12), f_{15}(12)] \\ [h_{14}(11), f_{14}(11), h_{13}(12), f_{13}(12)] \end{cases} & \mathcal{B}_{\Psi,2} &= \begin{cases} [h_6(1), f_6(1), h_5(2), f_5(2)] \\ [h_{16}(9), f_{16}(9), h_{15}(10), f_{15}(10)] \\ [h_{14}(9), f_{14}(9), h_{13}(10), f_{13}(10)] \\ [h_{12}(9), f_{12}(9), h_{11}(10), f_{11}(10)] \end{cases} \\
\mathcal{B}_{\Psi,3} &= \begin{cases} [h_8(1), f_8(1), h_7(2), f_7(2)] \\ [h_{16}(5), f_{16}(5), h_{15}(6), f_{15}(6)] \\ [h_{14}(5), f_{14}(5), h_{13}(6), f_{13}(6)] \\ [h_{12}(5), f_{12}(5), h_{11}(6), f_{11}(6)] \end{cases} & \mathcal{B}_{\Psi,4} &= \begin{cases} [h_{10}(1), f_{10}(1), h_9(2), f_9(2)] \\ [h_{16}(7), f_{16}(7), h_{15}(8), f_{15}(8)] \\ [h_{14}(7), f_{14}(7), h_{13}(8), f_{13}(8)] \\ [h_{12}(7), f_{12}(7), h_{11}(8), f_{11}(8)] \end{cases} \\
\mathcal{B}_{\Psi,5} &= \begin{cases} [h_{12}(1), f_{12}(1), h_{11}(2), f_{11}(2)] \\ [h_{10}(7), f_{10}(7), h_9(8), f_9(8)] \\ [h_{10}(5), f_{10}(5), h_9(6), f_9(6)] \\ [h_8(5), f_8(5), h_7(6), f_7(6)] \end{cases} & \mathcal{B}_{\Psi,6} &= \begin{cases} [h_{14}(1), f_{14}(1), h_{13}(2), f_{13}(2)] \\ [h_{16}(3), f_{16}(3), h_{15}(4), f_{15}(4)] \\ [h_{12}(3), f_{12}(3), h_{11}(4), f_{11}(4)] \\ [h_{10}(3), f_{10}(3), h_9(4), f_9(4)] \end{cases} \\
\mathcal{B}_{\Psi,7} &= \begin{cases} [h_{16}(1), f_{16}(1), h_{15}(2), f_{15}(2)] \\ [h_{14}(3), f_{14}(3), h_{13}(4), f_{13}(4)] \\ [h_8(3), f_8(3), h_7(4), f_7(4)] \\ [h_6(3), f_6(3), h_5(4), f_5(4)] \end{cases} & & \end{aligned} \tag{74}
\end{aligned}$$

Accordingly, the first sub-factor of type  $A$  becomes a  $SU(2)$ -block diagonal matrix, as can be quickly verified, thus composing as a whole a unitary matrix belonging to  $M_4ZYZ$ . In the second sub-factor of type  $B$ , the  $M_x^e$  factors are again  $SU(2)$ -block diagonal matrices, thus composing as a whole another unitary matrix belonging to  $M_4ZYZ$ . The circuit corresponding to the first sub-factor of type  $A$  and to  $M_x^e$  of the second sub-factor of type  $B$  is given by Figure 23 (the rotation parameters are renamed as  $\theta_j^*$ ). The remaining seven pairs of  $\prod T_x^e$  are implemented as described in Section 3.1.1; the result is illustrated in Figure 24.

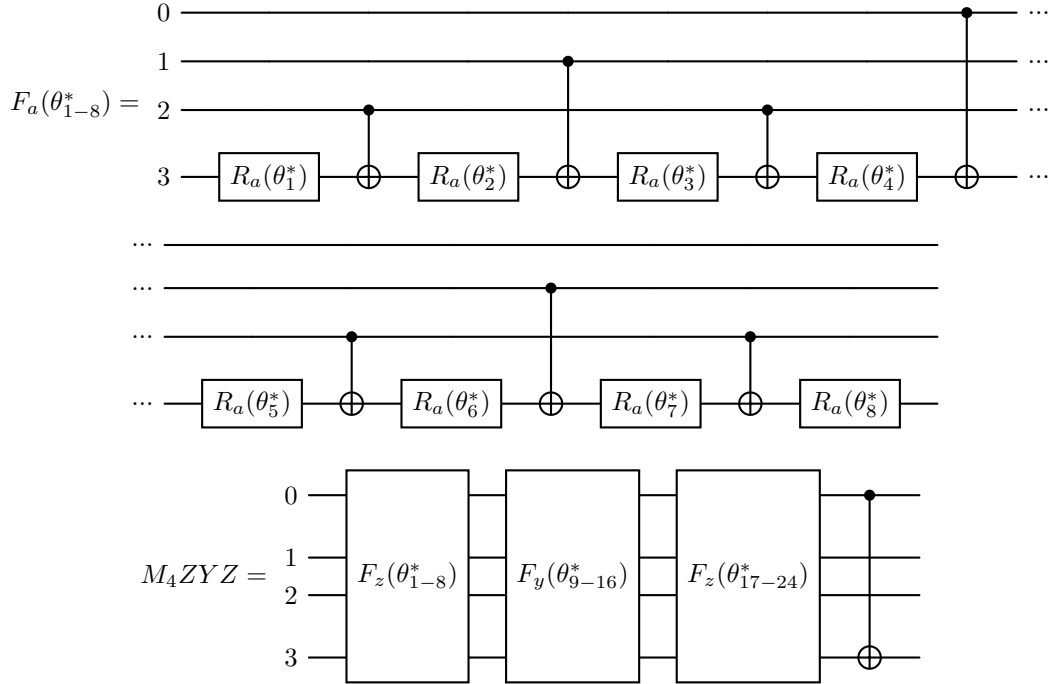


Figure 23:  $M_4ZYZ$  quantum circuit.

### 5.3 Odd contributions

In this subsection, the  $\Phi$ -factor (8) will be analyzed and compute for a general 4-qubit system; as already seen in Section 4.3, it is composed starting from the subset  $\mathcal{C}_\Phi$  of SRBB elements:

$$\Phi(\Theta_\Phi) = \prod_{x=1}^7 \left( \prod T_x^o \right) M_x^o \left( \prod T_x^o \right) \tag{75}$$

x	Bits	Binary	Control-Target
1	$x_0x_1x_2$	001	(3,2)
2	$x_0x_1x_2$	010	(3,1)
3	$x_0x_1x_2$	011	(3,1),(3,2)
4	$x_0x_1x_2$	100	(3,0)
5	$x_0x_1x_2$	101	(3,0),(3,2)
6	$x_0x_1x_2$	110	(3,0)(3,1)
7	$x_0x_1x_2$	111	(3,0),(3,1),(3,2)

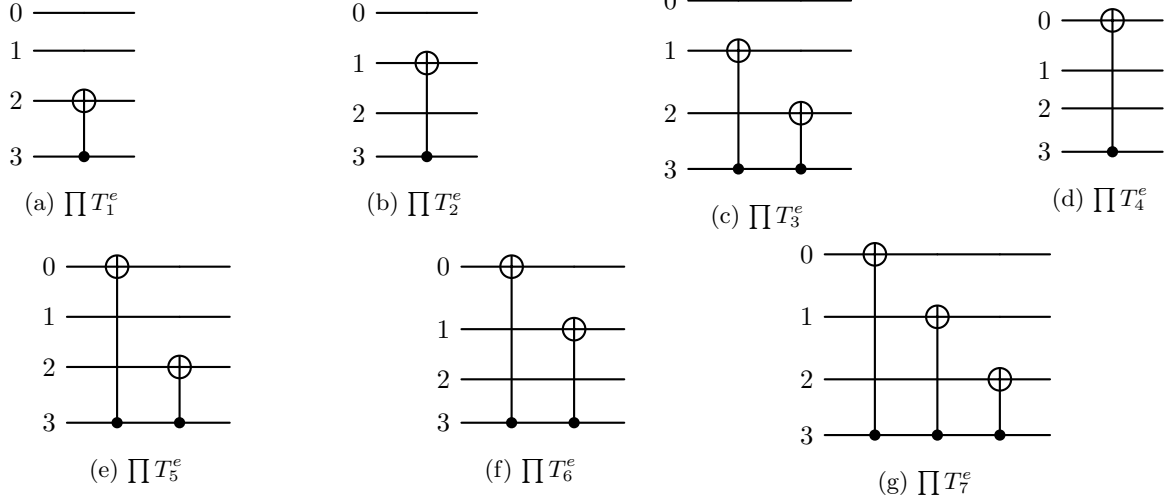


Figure 24: Diagram to find the control-target pairs for the CNOTs representing  $\prod T_x^e$ .

where

$$\begin{aligned}
\prod T_1^o &= P_{(2,3)}P_{(14,15)}P_{(12,15)}P_{(12,13)} \\
\prod T_2^o &= P_{(2,5)}P_{(10,15)}P_{(10,13)}P_{(10,11)} \\
\prod T_3^o &= P_{(2,7)}P_{(8,15)}P_{(8,13)}P_{(8,11)} \\
\prod T_4^o &= P_{(2,9)}P_{(6,15)}P_{(6,13)}P_{(6,11)} \\
\prod T_5^o &= P_{(2,11)}P_{(8,9)}P_{(6,9)}P_{(6,7)} \\
\prod T_6^o &= P_{(2,13)}P_{(4,15)}P_{(4,11)}P_{(4,9)} \\
\prod T_7^o &= P_{(2,15)}P_{(4,13)}P_{(4,7)}P_{(4,5)}
\end{aligned} \tag{76}$$

For practical reasons, only  $M_{1,2,3}^o$  are reported below given that the construction of the remaining ones is identical<sup>21</sup>.

$$\begin{aligned}
M_1^o &= \prod T_1^o \left[ \prod_{\substack{(2,3), (14,15), \\ (12,15), (12,13)}} \exp\{i\theta U_{h_\beta(\alpha-1)}\} \exp\{i\theta U_{f_\beta(\alpha-1)}\} \exp\{i\theta U_{h_{\beta+1}(\alpha)}\} \exp\{i\theta U_{f_{\beta+1}(\alpha)}\} \right] \prod T_1^o = \\
&= \prod T_1^o [\exp\{i\theta U_{h_3(1)}\} \exp\{i\theta U_{f_3(1)}\} \exp\{i\theta U_{h_4(2)}\} \exp\{i\theta U_{f_4(2)}\} \cdot \\
&\cdot \exp\{i\theta U_{h_{15}(13)}\} \exp\{i\theta U_{f_{15}(13)}\} \exp\{i\theta U_{h_{16}(14)}\} \exp\{i\theta U_{f_{16}(14)}\} \cdot \\
&\cdot \exp\{i\theta U_{h_{15}(11)}\} \exp\{i\theta U_{f_{15}(11)}\} \exp\{i\theta U_{h_{16}(12)}\} \exp\{i\theta U_{f_{16}(12)}\} \cdot \\
&\cdot \exp\{i\theta U_{h_{13}(11)}\} \exp\{i\theta U_{f_{13}(11)}\} \exp\{i\theta U_{h_{14}(12)}\} \exp\{i\theta U_{f_{14}(12)}\}] \prod T_1^o
\end{aligned} \tag{77}$$

<sup>21</sup>To avoid repetitions and write compact formulas, we omit repeating the subscript for the  $\theta_i$  angles, which will still be equal to that of the associated basis elements.

$$\begin{aligned}
M_2^o &= \prod T_2^o \left[ \prod_{\substack{(2,5), (10,15), \\ (10,13), (10,11)}} \exp\{i\theta U_{h_\beta(\alpha-1)}\} \exp\{i\theta U_{f_\beta(\alpha-1)}\} \exp\{i\theta U_{h_{\beta+1}(\alpha)}\} \exp\{i\theta U_{f_{\beta+1}(\alpha)}\} \right] \prod T_2^o = \\
&= \prod T_2^o [\exp\{i\theta U_{h_5(1)}\} \exp\{i\theta U_{f_5(1)}\} \exp\{i\theta U_{h_6(2)}\} \exp\{i\theta U_{f_6(2)}\} \cdot \\
&\cdot \exp\{i\theta U_{h_{15}(9)}\} \exp\{i\theta U_{f_{15}(9)}\} \exp\{i\theta U_{h_{16}(10)}\} \exp\{i\theta U_{f_{16}(10)}\} \cdot \\
&\cdot \exp\{i\theta U_{h_{13}(9)}\} \exp\{i\theta U_{f_{13}(9)}\} \exp\{i\theta U_{h_{14}(10)}\} \exp\{i\theta U_{f_{14}(10)}\} \cdot \\
&\cdot \exp\{i\theta U_{h_{11}(9)}\} \exp\{i\theta U_{f_{11}(9)}\} \exp\{i\theta U_{h_{12}(10)}\} \exp\{i\theta U_{f_{12}(10)}\}] \prod T_2^o
\end{aligned} \tag{78}$$

$$\begin{aligned}
M_3^o &= \prod T_3^o \left[ \prod_{\substack{(2,7), (8,15), \\ (8,13), (8,11)}} \exp\{i\theta U_{h_\beta(\alpha-1)}\} \exp\{i\theta U_{f_\beta(\alpha-1)}\} \exp\{i\theta U_{h_{\beta+1}(\alpha)}\} \exp\{i\theta U_{f_{\beta+1}(\alpha)}\} \right] \prod T_3^o = \\
&= \prod T_3^o [\exp\{i\theta U_{h_7(1)}\} \exp\{i\theta U_{f_7(1)}\} \exp\{i\theta U_{h_8(2)}\} \exp\{i\theta U_{f_8(2)}\} \cdot \\
&\cdot \exp\{i\theta U_{h_{15}(7)}\} \exp\{i\theta U_{f_{15}(7)}\} \exp\{i\theta U_{h_{16}(8)}\} \exp\{i\theta U_{f_{16}(8)}\} \cdot \\
&\cdot \exp\{i\theta U_{h_{13}(7)}\} \exp\{i\theta U_{f_{13}(7)}\} \exp\{i\theta U_{h_{14}(8)}\} \exp\{i\theta U_{f_{14}(8)}\} \cdot \\
&\cdot \exp\{i\theta U_{h_{11}(7)}\} \exp\{i\theta U_{f_{11}(7)}\} \exp\{i\theta U_{h_{12}(8)}\} \exp\{i\theta U_{f_{12}(8)}\}] \prod T_3^o
\end{aligned} \tag{79}$$

The elements of the algebraic basis  $\mathcal{U}^{(16)}$  that come into play belong to the following set  $C_\Phi$ , divided into seven subsets  $C_{\Phi,x}$ :

$$\begin{aligned}
C_{\Phi,1} &= \begin{cases} [h_3(1), f_3(1), h_4(2), f_4(2)] \\ [h_{15}(13), f_{15}(13), h_{16}(14), f_{16}(14)] \\ [h_{15}(11), f_{15}(11), h_{16}(12), f_{16}(12)] \\ [h_{13}(11), f_{13}(11), h_{14}(12), f_{14}(12)] \end{cases} & C_{\Phi,2} &= \begin{cases} [h_5(1), f_5(1), h_6(2), f_6(2)] \\ [h_{15}(9), f_{15}(9), h_{16}(10), f_{16}(10)] \\ [h_{13}(9), f_{13}(9), h_{14}(10), f_{14}(10)] \\ [h_{11}(9), f_{11}(9), h_{12}(10), f_{12}(10)] \end{cases} \\
C_{\Phi,3} &= \begin{cases} [h_7(1), f_7(1), h_8(2), f_8(2)] \\ [h_{15}(7), f_{15}(7), h_{16}(8), f_{16}(8)] \\ [h_{13}(7), f_{13}(7), h_{14}(8), f_{14}(8)] \\ [h_{11}(7), f_{11}(7), h_{12}(8), f_{12}(8)] \end{cases} & C_{\Phi,4} &= \begin{cases} [h_9(1), f_9(1), h_{10}(2), f_{10}(2)] \\ [h_{15}(5), f_{15}(5), h_{16}(6), f_{16}(6)] \\ [h_{13}(5), f_{13}(5), h_{14}(6), f_{14}(6)] \\ [h_{11}(5), f_{11}(5), h_{12}(6), f_{12}(6)] \end{cases} \\
C_{\Phi,5} &= \begin{cases} [h_{11}(1), f_{11}(1), h_{12}(2), f_{12}(2)] \\ [h_9(7), f_9(7), h_{10}(8), f_{10}(8)] \\ [h_9(5), f_9(5), h_{10}(6), f_{10}(6)] \\ [h_7(5), f_7(5), h_8(6), f_8(6)] \end{cases} & C_{\Phi,6} &= \begin{cases} [h_{13}(1), f_{13}(1), h_{14}(2), f_{14}(2)] \\ [h_{15}(3), f_{15}(3), h_{16}(4), f_{16}(4)] \\ [h_{11}(3), f_{11}(3), h_{12}(4), f_{12}(4)] \\ [h_9(3), f_9(3), h_{10}(4), f_{10}(4)] \end{cases} \\
C_{\Phi,7} &= \begin{cases} [h_{15}(1), f_{15}(1), h_{16}(2), f_{16}(2)] \\ [h_{13}(3), f_{13}(3), h_{14}(4), f_{14}(4)] \\ [h_7(3), f_7(3), h_8(4), f_8(4)] \\ [h_5(3), f_5(3), h_6(4), f_6(4)] \end{cases}
\end{aligned} \tag{80}$$

Accordingly, the  $M_x^o$  factors become  $2 \times 2$ -block diagonal matrix where each block no longer belongs to  $SU(2)$  (but only to  $U(2)$ ), as can be quickly verified, thus composing as a whole a unitary matrix that can be decomposed only in part through a  $M_4 ZYZ$  [32]. Exploiting the unitary (phase) scaling that exists between  $U(n)$  and  $SU(n)$ , the circuit for  $M_x^o$  is given by Figure 25. Therefore, for  $n = 4$  the scalability scheme proposed by [33] continues to hold and is again justified by the algebraic properties under permutation shown by equations (77), (78), (79). The remaining seven pairs of  $\prod T_x^o$  factors are implemented through the recipe described in Section 3.1.1 (see Figure 26).

## 5.4 4-qubit circuit to approximate $SU(16)$

Composing the circuits of the previous subsections, we can draw the overall circuit to approximate a general (special) unitary operator according to equation (5) with a QNN. As will be seen from the test results presented in Section 7, the designed QNN can be trained with one single layer, regardless of the sparsity of the operator; this result is very interesting in comparison from the numerical simulations carried out in a complete classical



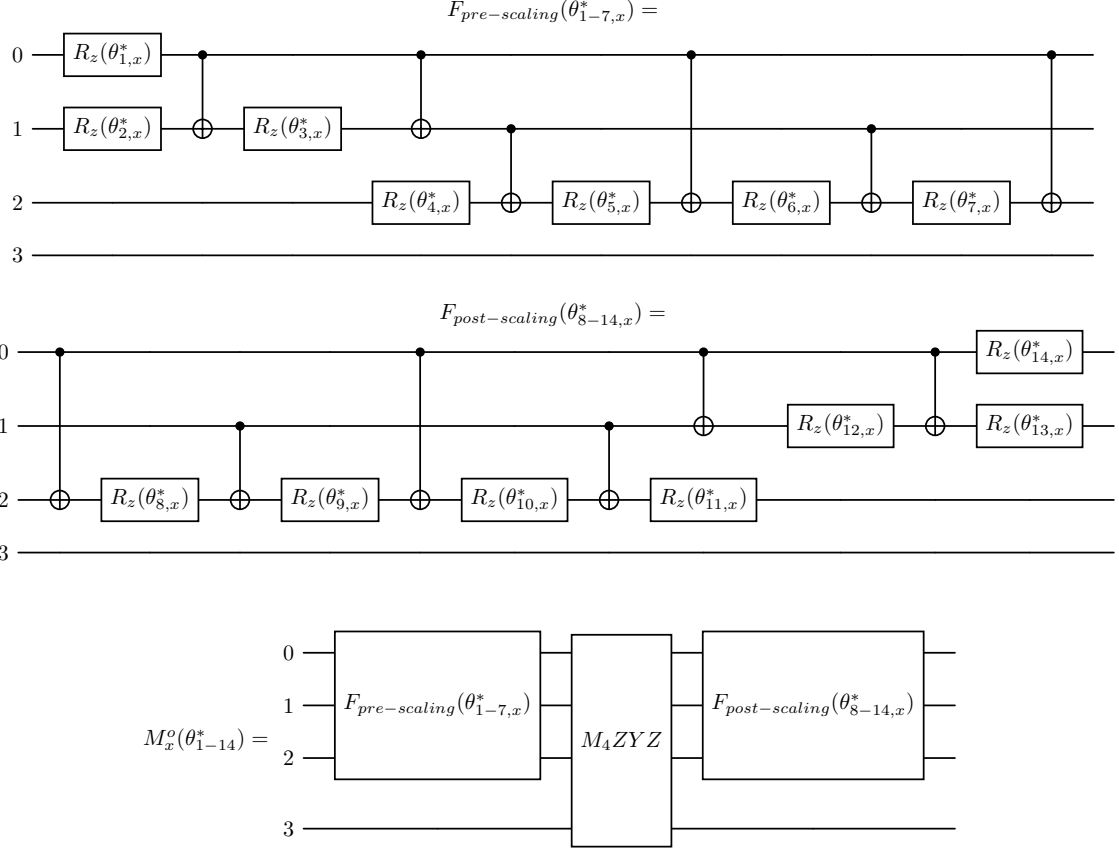


Figure 25:  $M_x^o$  quantum circuit.

context using optimization algorithms like Neelder-Mead [32]. For this reason, in the following, we will take into consideration  $l = 1$  by rewriting the approximating operator in the following way:

$$\begin{aligned}
\mathcal{U}_{approx}(\Theta) &= Z_1(\Theta_Z) \Psi_1(\Theta_\Psi) \Phi_1(\Theta_\Phi) = \\
&= \prod_{i \in \mathcal{D}_Z} \exp\{i \theta_i U_i\} \prod_{j \in \mathcal{A}_\Psi} \exp\{i \theta_j U_j\} \cdot \prod_{x=1}^7 \left[ \prod_{k_e \in \mathcal{B}_{\Psi,x}} \exp\{i \theta_{k_e} U_{k_e}\} \right] \prod_{x=1}^7 \left[ \prod_{k_o \in \mathcal{C}_{\Phi,x}} \exp\{i \theta_{k_o} U_{k_o}\} \right] \quad (81)
\end{aligned}$$

Finally, keeping in mind the reversed order of the factors compared to the mathematical writing, in Figure 27 is illustrated the overall circuit from left to right, line by line, taking care to label its sub-components; considering the depth, the circuit is broken into several sub-figures. Figure 27 highlights which parts of the quantum circuit repeat identically for this particular case  $n = 4$  and it is possible to immediately notice which CNOTs are simplified (red gates). Eliminating these latter, the final CNOT-optimized quantum circuit capable of approximating any special unitary operator with 4 qubits is found.

## 6 A scalable algorithm for optimizing CNOT-gates in the SRBB-based synthesis framework

In the previous Sections, a detailed construction of the VQCs to approximate unitary evolutions with the SRBB decomposition is provided for  $n = 2, 3, 4$ . Besides, from an implementation viewpoint, the scalable design of the quantum circuits is derived step by step from the algebraic properties of SRBB elements and their peculiar grouping, as proposed by the literature [33].

In this Section, a new scalable algorithm that takes into account CNOT-simplifications and perfectly compatible with the grouping introduced in [33] is proposed and analyzed in depth. As anticipated,  $n = 2$  represents a very particular case excluded from the scalable scheme due to the anomalous matrix properties of its factor  $M_1^o$ . In order to clearly illustrate the new simplification scheme and its features, various examples will be proposed after a general discussion which aims to present the implementation details; by doing so, the anomalies of the  $n = 2$  case will also be highlighted.

x	Bits	Binary	Control-Target	k-index
1	$x_0x_1x_2$	001	(3,2)	2
2	$x_0x_1x_2$	010	(3,1)	1
3	$x_0x_1x_2$	011	(3,1),(3,2)	1
4	$x_0x_1x_2$	100	(3,0)	0
5	$x_0x_1x_2$	101	(3,0),(3,2)	0
6	$x_0x_1x_2$	110	(3,0),(3,1)	0
7	$x_0x_1x_2$	111	(3,0),(3,1),(3,2)	0

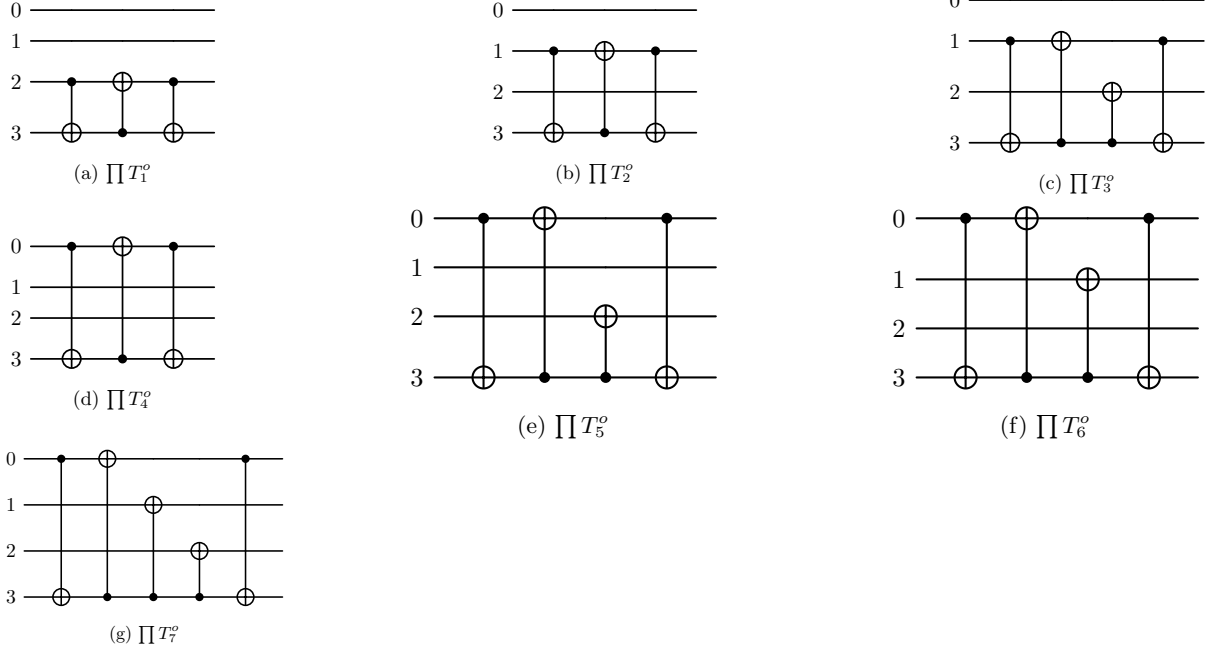


Figure 26: Diagram to find the control-target pair and the  $k$ -index for the CNOTs representing  $\prod T_x^o$ .

Considering the original structure of the overall approximating quantum circuit for a generic  $n$ , represented by equation (5), only some circuit blocks allow simplifications of CNOT gates, as stated by the following proposition.

**Proposition 2.** *For  $n \geq 3$ , the SRBB-type decomposition produces CNOT-simplifications inside the  $Z(\Theta_Z)$ -factor, representing the diagonal contributions of the  $SU(2^n)$  algebraic basis, and between  $\prod T_x^{e/o}$  factors, representing respectively permutation matrices with even/odd indices.*

*Proof.* With reference to equation (5) and to the scalable features of the resulting quantum circuit (see for instance Figure 27 in combination with Figure 23 and Figure 25), the factors called  $M_x^{e/o}$  do not allow CNOT-simplifications either within them or with adjacent factors from  $n = 3$  onwards. Firstly, from their complete decomposition, it is immediate to see that a rotation is always interposed between a pair of CNOTs; secondly, while  $M_x^e$  factors start with a rotation and end with a  $\text{CNOT}_{(0,n-1)}$ ,  $M_x^o$  factors start and end with a couple of rotations, preventing simplifications with adjacent CNOTs of the previous and subsequent factors<sup>22</sup>. For this reason, it can be said that  $M_x^{e/o}$  factors are encapsulated inside a pair of  $\prod T_x^{e/o}$  factors for each value of  $x$ , which from now on will be denoted as the *edges* of the  $\Psi(\Theta_\Psi)/\Phi(\Theta_\Phi)$ -factors.  $\square$

## 6.1 Simplifying CNOTs between diagonal contributions

For an  $n$ -qubit register, the SRBB elements that come into play in the  $Z(\Theta_Z)$ -factor design (6) belong to the set  $\zeta_n = \{j^2 - 1, 2 \leq j \leq 2^n\}$ , a total of  $2^n - 1$  elements, i.e., all the diagonal elements except the last one. The diagonal nature of these algebraic elements allows building the corresponding circuit according to different orderings, but the most interesting among them is the one with the largest number of simplifications between

<sup>22</sup>The particular case  $n = 2$  and its simplifications will be discussed in section 6.3.2.

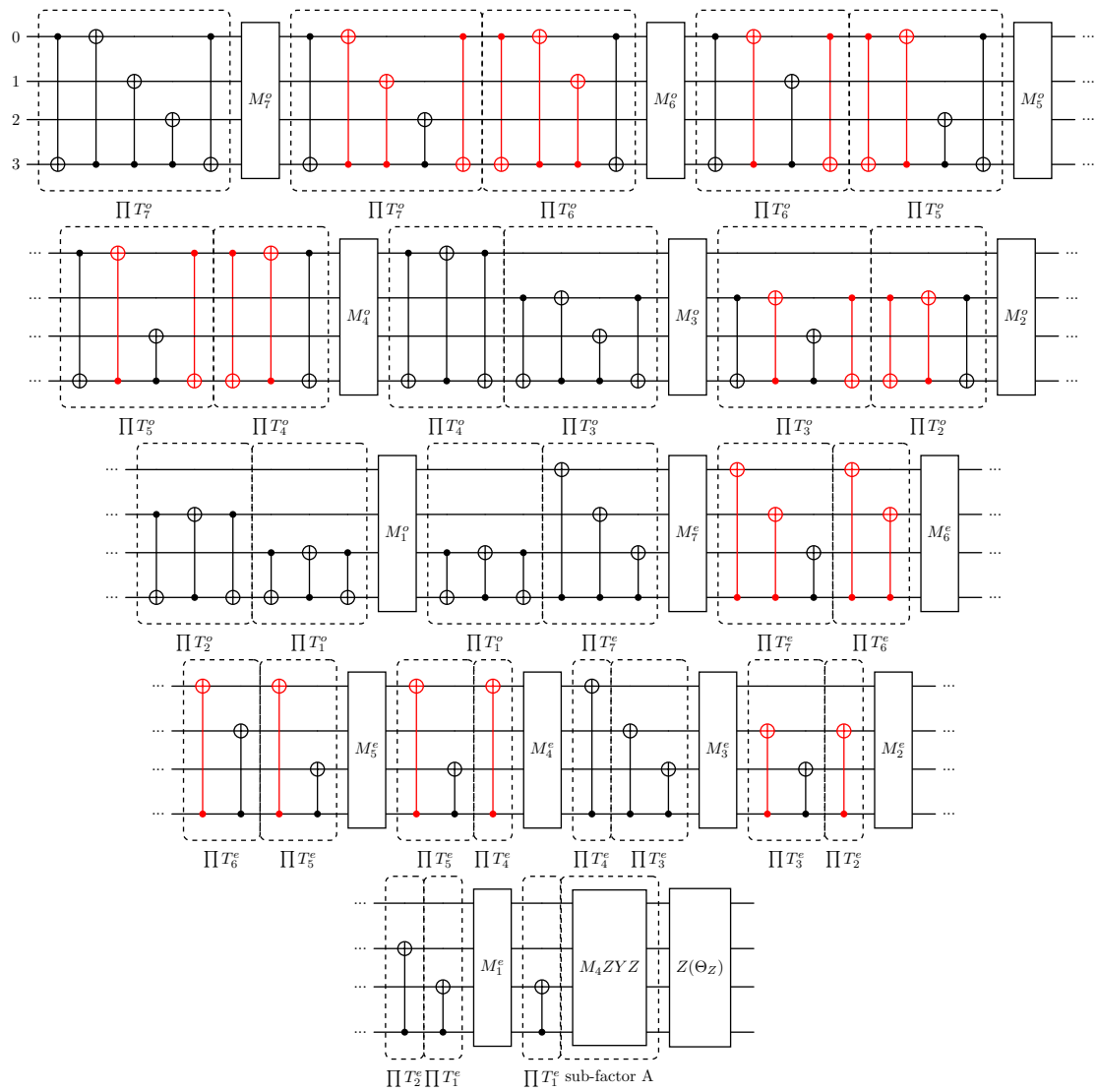


Figure 27: Quantum circuit for general 4-qubit special unitary operators.

CNOT gates. Therefore, it is absolutely important to understand how these simplifications occur and the  $n = 3$  case is considered as a reference example to clarify that<sup>23</sup>. Starting from the set  $\zeta_3 = \{3, 8, 15, 24, 35, 48, 63\}$ , Table 11 is constructed to order its diagonal elements and derive the pairs of parameters  $(m, m')$ , in turn useful to design the quantum circuit for the  $Z$ -factor. The rows of this table are the binary representation of numbers

Position	1° q	2° q	3° q	Element	$m$	$m'$
1	0	0	1	$U_3$	3	
2	0	1	0	$U_8$	2	
3	0	1	1	$U_{15}$	3	2
4	1	0	0	$U_{24}$	1	
5	1	0	1	$U_{35}$	3	1
6	1	1	0	$U_{48}$	2	1
7	1	1	1	$U_{63}$	3	1,2

Table 11: Pairs of parameters  $(m, m')$  to build the  $Z(\Theta_Z)$ -factor circuit for  $n = 3$ .

from 1 to  $2^n - 1 = 7$ , while some columns are associated with the qubits of the quantum register, labeled from 1 to  $n$ , from left to right. Then, for each row, the parameter  $m$  is associated with the rightmost 1 bit of the binary string and the parameter  $m'$  with any other bits equal to 1. The last two columns of Table 11 report the values of the pairs  $(m, m')$ . Lastly, each row corresponds to a diagonal element of the circuit according to the following recipe [33]: the parameter  $m$  indicates the qubit on which to perform a  $z$ -rotation, while the parameter  $m'$  indicates the control qubit of a CNOT-pair with target on the qubit indicated by  $m$ ; if  $m' \neq 0$ , the same CNOT must be placed before and after the  $R_z$ -gate. Figure 28 illustrates an example of CNOT-simplification (red gates) for the  $Z$ -factor in the  $n = 3$  case, resulting from the concatenation of elements  $U_{15}$  and  $U_{63}$ . It is clear that a CNOT-simplification occurs due to a juxtaposition on the same control-target pair between different diagonal contributions, if no evolution of information (interference) comes from the gates in between. From a diagrammatic point of view, this fact in Table 11 is reflected in the condition of having the two binary strings representing the elements taken into consideration with at least two pairs of bits with value 1 in the same position and one of these must correspond to the last qubit.

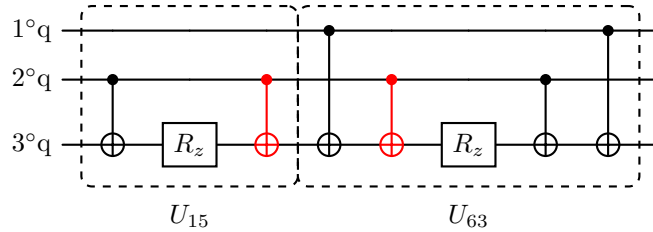


Figure 28: Example of a CNOT-simplification within the  $Z(\Theta_Z)$ -factor for the sub-sequence  $U_{15} - U_{63}$ .

**Proposition 3.** *A CNOT-simplification within the  $Z(\Theta_Z)$ -factor occurs due to a juxtaposition of the same parametric pair  $(m, m')$  between different binary strings representing diagonal contribution of the SRBB.*

*Proof.* The specific case for  $n = 3$ , described above as an example to clarify the conditions of simplification, has a completely general value since it is based on:

- i) the relationship between the pair of parameters  $(m, m')$  and the circuit representation of diagonal SRBB contributions (first defined in [32]);
- ii) the properties of the binary representation valid for any  $n$ .

□

To proceed further and deduce a fundamental feature of the scaling pattern for this diagonal factor, an important observation is mandatory: thanks to the properties of the binary representation, the rows of Table 11 that end with 0 correspond to all and only the rows of the binary table for the  $n = 2$  case (with the obvious precaution of eliminating the rightmost qubit and renaming the diagonal elements). This implies a recursive

<sup>23</sup>Being the first case for which scalability applies, it is the simplest example but also the best starting point for building any other.

scheme within the scalability scheme; fixed  $n$  by the choice of the quantum register, only the rows of the binary table ending with 1 will bring a new contribution to the circuit, while the remaining ones exactly represent the circuit for the  $Z$ -factor of the  $n - 1$  case. This is true except for  $n = 2$  which falls out the scalability scheme and justifies the following proposition.

**Proposition 4.** *For  $n \geq 3$ , the optimal number of CNOTs in the  $Z$ -factor design is reachable by implementing only the rows that end with 1-valued bit of the binary table representing the SRBB diagonal contributions, in addition to the circuit of the previous  $n - 1$  case, if a scalable method is known to simplify pairs of CNOTs.*

*Proof.* This proof relies entirely on the properties of binary representation; keeping in mind that the last diagonal element (the one corresponding to the binary string with only zeros) is not taken into account, in the transition to the binary table of the  $n - 1$  case it is necessary to eliminate the column of the last qubit and the rows ending with 0. Thus, if you have a *scalable* method to find the maximum number of simplifications between the parametric pairs  $(m, m')$ , exploiting the properties of the binary representation it is possible to apply it recursively only to the rows ending in 1 of the case  $n$  in question and add the  $Z$ -factor circuit for the  $n - 1$  case, already simplified in the previous iteration. Since the minimum number of qubits of interest is 2, because for  $n = 1$  the SRBB would be replaced by the well known Pauli Basis, 2-qubit systems are excluded by this proposition as they are included in the first iteration (every recursive method requires a starting point).  $\square$

In the following, the scalable and easily implementable algorithm that directly provides the CNOT-simplified circuit for rows ending with 1 is described. This pattern has been investigated with different methods, some of which based on combinatorics<sup>24</sup> and one based on Gray Code: it is possible to prove that the latter encodes the optimal solution.

### 6.1.1 Gray-Code-based solution

As anticipated, it turned out that the cyclic Gray Code matrices encode the optimal solution in terms of CNOT-simplifications. Before providing the proof, the fundamental steps of the algorithm are described taking the  $n = 3$  case as reference to facilitate its generalization and therefore its implementation.

The starting point is to recursively construct the (cyclic) Gray Code matrices up to the case  $n$  in question; their columns are labeled according to the qubits of the quantum register from left to right. Then, for the recursive scheme already explained, only the rows ending with 1 are considered, one for each diagonal element associated to a new contribution (a subset of  $\zeta_3$ , highlighted in blue in Table 12). The latter are important for the following two reasons.

- i. Reading the table from top to bottom, it is possible to recognize the optimal ordering of the involved elements that ensures the largest number of CNOT-simplification, recovering the correspondence with algebraic elements described in Table 11. In particular, as illustrated in Table 12, the first line ending with 1 will always be the simplest contribution due to the Gray Code rule and so the last little block of the sequence (see for instance Figure 29). The second line ending with 1, instead, will always be the first little block of the sequence and, after it, all the others in order. In other words, the first element of the optimal sequence will always be the second line ending with 1 and then all the others following the order of the *cyclic* Gray Code. The reason why it is best to keep the simplest algebraic element at the end will be clear once the complete structure is obtained.
- ii. Reading the table from top to bottom, two lines at a time, it is possible to identify a rule that directly designs the CNOT-simplified circuit. In correspondence with the only bit that changes from one row to another, associate a CNOT with the control in that qubit and the target in the  $n$ -th qubit, followed by a  $z$ -rotation in the  $n$ -th qubit. Keeping in mind that simplified gates are marked in red in Figure 29, the rule can be checked for the sub-sequence 15-63. Thus, every row of Table 12 corresponds to a piece of the circuit, but what matters are the jumps between two green lines. In the first jump, the only bit that changes is the second, so a  $\text{CNOT}_{(2,3)}$  and a rotation in the third qubit. In the second jump, the only bit that changes is the first, so a  $\text{CNOT}_{(1,3)}$  and a rotation in the third qubit, bypassing the simplified pair of CNOTs, and so on.

Finally, Figure 30 shows the  $Z$ -factor circuit for the  $n = 3$  case resulting from all the simplifications just introduced. The circuit for the diagonal contributions is composed by 2 blocks; the first block comes from the rows of the binary table ending with 1 (new contributions of the case  $n$  in question) and relies on a Gray Code pattern (scalable part), which encode the optimal ordering in terms of CNOT-count; the second block comes

<sup>24</sup>A solution that is not entirely optimal can be found by placing the elements with at least one similar pair  $(m, m')$  next to the element with the greatest (or greater) number of pairs  $(m, m')$ , once on the right and once on the left, until the items run out.

$n = 1$	$n = 2$		$n = 3$			Element
$1^\circ \text{q}$	$1^\circ \text{q}$	$2^\circ \text{q}$	$1^\circ \text{q}$	$2^\circ \text{q}$	$3^\circ \text{q}$	
			0	0	0	-
			0	0	1	$U_3$
0	0	0	0	1	1	$U_{15}$
	0	1	0	1	0	-
1	1	1	1	1	0	-
	1	0	1	1	1	$U_{63}$
			1	0	1	$U_{35}$
			1	0	0	-

Table 12: Cyclic Gray Code matrices.

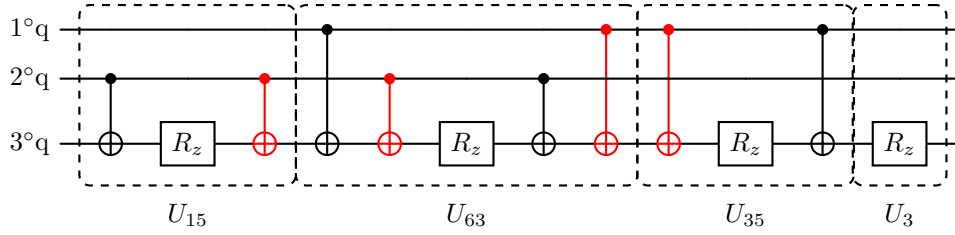


Figure 29: Simplifications (red gates) coming from new diagonal contributions only.

from the rows of the binary table ending with 0 and it is exactly the  $Z$ -factor circuit for the previous  $n - 1$  case (recursive part). This scalable and partly recursive simplification scheme guarantees the minimum number of CNOT gates at any  $n$  inside the  $Z$ -factor of the SRBB-based approximate unitary synthesis algorithm.

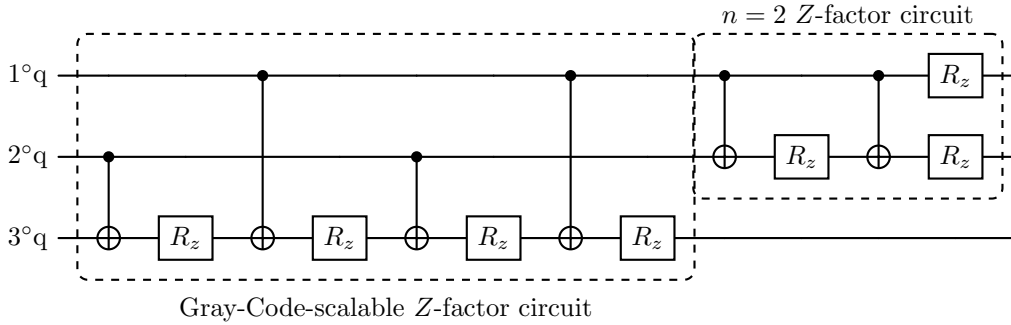


Figure 30: The  $Z(\Theta_Z)$ -factor circuit for  $n = 3$  with reduced CNOT-count.

**Proposition 5.** For  $n \geq 3$ , the minimum number of CNOT gates within the  $Z(\Theta_Z)$ -factor of the SRBB-type decomposition is achieved by the combination of a scalable Gray-Code-ordering of new diagonal contributions and a recursive algorithm that adds the contributions of the  $n - 1$  case.

*Proof.* This proof is built on logic by contradiction; suppose that there is a better ordering of the diagonal elements than the Gray Code along the linear sequence, i.e., an ordering that implies a larger number of pairs of simplified CNOTs. It is important to note that, depending on the chosen ordering, a higher number of simplified CNOTs can come from:

- i. a greater number of edges (between different diagonal elements) that present simplifications;
- ii. a greater number of simplified pairs (therefore pairs of parameters  $(m, m')$  juxtaposed) in the edges already considered.

The first step is to demonstrate that Gray Code sorting already uses the largest number of edges that admit simplifications between CNOT-pairs. The number of non-recursive diagonal elements, corresponding to new contributions or binary strings ending in 1, are exactly  $2^{n-1}$ ; but among the latter, the first element (the one

with the simplest binary string) cannot generate simplifications of CNOTs<sup>25</sup> and must be subtracted, remaining with  $2^{n-1} - 1$  elements. This is the reason why this element is always placed at the end of the sequence of non-recursive diagonal elements and, as can be seen from Figures 30 and 32, allows the circuit to be compacted. Therefore, the maximum number of edges that could present simplifications is  $2^{n-1} - 2$ , i.e., the number of elements suitable for simplifications minus one.

As can be deduced from Section 6.1.1, in Gray-Code-based sorting the CNOT-simplifications correspond to pairs of 1's in the same qubit (see for example the pairs of 1-valued bits for the subsequence  $U_{15} - U_{63}$  in Table 12). Considering only rows ending in 1 except for the first one, cyclic order on the Gray Code matrix will encounter pairs of rows that always share at least one 1-valued qubit in addition to the last one, and thus also a simplification. For this reason, the Gray-Code-based method uses by definition the maximum number of edges with simplifications, for which the only way to have a larger number of simplifications is to consider case ii. Therefore, the discussion shifts to counting the total number of control-target pairs and how many times each parameter  $m'$  produces a pair of CNOTs to be simplified.

Since  $m'$  varies from 1 to  $n - 1$  and the number of 1s in each column of the binary table is equal to  $2^{n-1}$  (see for example Tables 11 and 15), the number of parameters  $m'$  useful for non-recursive pattern in each column is equal to  $2^{n-2}$  and the total number of pairs  $(m, m')$  is worth  $(n - 1) \cdot 2^{n-2}$ . Due to the linear sequence, each element can be used twice for the same index  $m'$ , i.e., one pair with a previous element and one with a following element, except for the elements at the ends of the sequence: this implies that each parameter  $m'$  can be used at most  $2^{n-2} - 1$  times. With reference to Tables 11 and 15, Tables 13 and 14, respectively, show these counts in cases  $n = 3, 4$  to clarify. From the examples in Tables 13 and 14, it is clear that the Gray Code method exploits

$m' (n = 3)$	available	used	max
1	2	1	yes
2	2	1	yes

Table 13: Counts of parameters  $m'$  used to form pairs of CNOT-simplifications in  $n = 3$  cases.

$m' (n = 4)$	available	used	max
1	4	3	yes
2	4	3	yes
3	4	2	no

Table 14: Counts of parameters  $m'$  used to form pairs of CNOT-simplifications in  $n = 4$  cases.

each index to the maximum only for some values of  $n$  and with simple counts it is possible to highlight which indices could offer further simplifications<sup>26</sup>. At this point, having a greater number of simplified pairs means having further control-target couplings involving the parameters  $m'$  which are not used to the maximum, but this is impossible as all the elements suitable for these couplings have already been used a maximum number of times. To prove this latter sentence, it is useful to count the number of elements involved in the simplification pairs for each parameter  $m'$  and also the number of elements shared by simplifications with different  $m'$  indexes. In this way it can be shown how the saturation of the simplification pairs for the first parameters  $m'$  (the ones used to the maximum at every  $n$ ) reduces the number of elements available for couplings with other subsequent values of  $m'$ .

Considering the binary tables used for sorting, each parameter  $m'$  takes into account an equal number of non-recursive diagonal elements, namely  $2^{n-2}$ . Since some binary strings have a multi-valued parameter  $m'$ , the corresponding elements will show different possible pairs of simplification. In this way, in counting the elements involved in the simplification pairs, some elements will be shared by different pairs of parameters  $(m, m')$ . The method illustrated below counts precisely these shared elements and shows that, for each index  $m'$ , the number of shared elements is exactly what allows using all the diagonal elements (and having simplifications between each of them). In the binary tables, like Table 11 and 15,  $n - 1$  columns represent the possible values of  $m'$ . To count the elements shared by two different simplification pairs the following recipe can be considered:

- a) the value  $m' = 1$  (the first column on the left) can be ignored as it is the first index to saturate;

<sup>25</sup>Simplifications are prohibited for this element because it is the only one with no value for the parameter  $m'$ , see for instance Tables 12 and 16.

<sup>26</sup>Actually, it is simple to prove that only for  $n = 3$  the method exploits each index to the maximum and from  $n = 4$  onwards the indices not fully used increase as  $n$  increases.

- b) for  $2 \leq m' \leq n-1$ , a shared element is present if in correspondence with a 1 in column  $m'$  there are other 1s associated with it in the columns to its left.

Then, having ordered the columns of the binary representation from 1 to  $n$  and from left to right, the first column will have  $2^0 = 1$  group of  $2^{n-1}$  1-valued bits, the second column will have  $2^1 = 2$  groups of  $2^{n-2}$  1-valued bits each, the third column will have  $2^2 = 4$  groups of  $2^{n-3}$  1-valued bits each, and so on. It is then possible to enumerate the binary strings that have a 1-valued bit in the  $i$ -th column and others 1-valued bits in the columns to its left, according to the following formula:

$$\begin{aligned} \sum_{i=1}^{n-2} \frac{2^{n-1}}{2 \cdot 2^i} (2^i - 1) &= 2^{n-2}(n-2) - 2^{n-2} \left( \sum_{i=1}^{n-2} \frac{1}{2^i} \right) = 2^{n-2} \left[ (n-2) - \sum_{i=0}^{n-2} \frac{1}{2^i} + 1 \right] = \\ &= 2^{n-2}(n-3) + 1 \end{aligned} \quad (82)$$

The saturation of  $(m, m')$  pairs available for subsequent simplifications is shown by the difference between the sum of all the elements involved by each index  $m'$  and the number of elements shared by the pairs with different  $m'$  along the *linear* sequence:

$$2^{n-2}(n-1) - 2^{n-2}(n-3) - 1 = 2^{n-1} - 1 \quad (83)$$

that is exactly the number of non-recursive diagonal elements considered in the design of the scalable part of the  $Z$ -factor. In conclusion, a greater number of CNOT-simplifications is not possible since they should be looked for in the  $(m, m')$  pairs with non-saturated  $m'$  values, but there are no elements available after the saturation of the first indexes  $m'$ . Indeed, it would imply other elements of the sequence in addition to the totality already considered (maximum number of edges with simplifications reached) or other couplings in addition to the possible ones already considered (once the first indices are saturated, there are no longer couplings available for not fully-used  $m'$  indexes with the elements left in play). While the first scenario contradicts the initial assumption on the number of diagonal elements, the second one contradicts the linear sequence assumption.  $\square$

The scalable algorithm for the  $Z$ -factor circuit stated in Proposition 5, optimized in terms of CNOT gates through a Gray-Code-ordering, is illustrated via pseudocode in Algorithm 1.

---

**Algorithm 1** [ $Z$ -FACTOR] Scalable CNOT-optimized  $Z(\Theta_Z)$ -factor circuit

---

- 1: **Provided:**  $CNOT(c, t)$  where  $c$  stands for control and  $t$  for target;  $R_z(\theta_a)$ ; an algorithm that generates the binary matrices where the 1s indicate the only bit that changes line after line in the Gray Code recursion, called *CNOT-remaining-Gray* (see Table 12 and Figure 29); the usual notation where the first qubit is labeled with 0.
  - 2: **Input:** number of qubits  $n > 2$ ; set of parameters  $\theta_a \in \Theta_Z$ ; output of *CNOT-remaining-Gray*.
  - 3: **Output:** circuit for the  $Z(\Theta_Z)$ -factor, optimized in terms of *CNOT* gates.
  - 4: **for all**  $k$  such that  $0 \leq k < n-1$  **do**
  - 5:   Consider the output of *CNOT-remaining-Gray* in the reversed order, i.e., the binary matrix  $n-2-k$
  - 6:   **for** row  $i$  in matrix  $n-2-k$  **do**
  - 7:     **for** column  $j$  in row  $i$  **do**
  - 8:      **if** element  $(i, j)$  equals 1 **then**
  - 9:         $CNOT(j, n-1-k)$
  - 10:         $R_z(\theta_{a_i})$  on qubit  $n-1-k$
  - 11:      **else**
  - 12:        Pass
  - 13:      **end if**
  - 14:    **end for**
  - 15: **end for**
  - 16: **end for**
  - 17:  $R_z(\theta_{a_{2^{n-1}}})$  on qubit 0
- 

### 6.1.2 Solution for $n = 4$

As for 3-qubit systems, the starting point is to identify the SRBB diagonal elements which participate in the construction of the  $Z$ -factor. The latter belong to the set

$$\zeta_4 = \{3, 8, 15, 24, 35, 48, 63, 80, 99, 120, 143, 168, 195, 224, 255\}$$



Position	1° q	2° q	3° q	4° q	Element	$m$	$m'$
1	0	0	0	1	$U_3$	4	
2	0	0	1	0	$U_8$	3	
3	0	0	1	1	$U_{15}$	4	3
4	0	1	0	0	$U_{24}$	2	
5	0	1	0	1	$U_{35}$	4	2
6	0	1	1	0	$U_{48}$	3	2
7	0	1	1	1	$U_{63}$	4	2,3
8	1	0	0	0	$U_{80}$	1	
9	1	0	0	1	$U_{99}$	4	1
10	1	0	1	0	$U_{120}$	3	1
11	1	0	1	1	$U_{143}$	4	1,3
12	1	1	0	0	$U_{168}$	2	1
13	1	1	0	1	$U_{195}$	4	1,2
14	1	1	1	0	$U_{224}$	3	1,2
15	1	1	1	1	$U_{255}$	4	1,2,3

Table 15: Pairs of parameters  $(m, m')$  to build the  $Z(\Theta_Z)$ -factor circuit.

and Table 15 sorts them according to the binary representation of their position in the set. Then, the cyclic Gray Code matrix for  $n = 4$  is constructed and its rows ending with 1 are highlighted in green, as illustrated in Table 16. Finally, reading the table from top to bottom, two lines at a time, it is possible to directly draw

$n = 1$	$n = 2$		$n = 3$			$n = 4$				Element
1° q	1° q	2° q	1° q	2° q	3° q	1° q	2° q	3° q	4° q	
						0	0	0	0	-
						0	0	0	1	$U_3$
						0	0	1	1	$U_{15}$
			0	0	0	0	0	1	0	-
			0	0	1	0	1	1	0	-
			0	0	1	0	1	1	1	$U_{63}$
	0	0	0	1	1	0	1	0	1	$U_{35}$
0	0	1	0	1	0	0	1	0	0	-
1	1	1	1	1	0	1	1	0	0	-
			1	1	1	1	1	0	1	$U_{195}$
			1	0	1	1	1	1	1	$U_{255}$
			1	0	0	1	1	1	0	-
						1	0	1	0	-
						1	0	1	1	$U_{143}$
						1	0	0	1	$U_{99}$
						1	0	0	0	-

Table 16: Cyclic Gray Code matrices.

the circuit simplified in terms of CNOTs. In Figure 31, the optimal sequence of diagonal elements is illustrated (simplified gates are marked in red for clarity) and the resulting circuit for the  $Z$ -factor of the  $n = 4$  case is shown in Figure 32.

## 6.2 Simplifying CNOTs between even/odd contributions

For an  $n$ -qubit register, there are exactly  $2^{n-1} - 1$  factors of type  $\prod T_x^e$  that come into play in the construction of the  $\Psi(\Theta_\Psi)$ -factor (7) and the same number for  $\prod T_x^o$  that come into play in the construction of the  $\Phi(\Theta_\Phi)$ -factor (8). These factors are denoted as the edges of the  $\Psi/\Phi$ -factor, respectively, because they flank, both from the right and from the left, each sub-factor  $M_x^{e/o}$  that appears inside it. Precisely between these edges, simplifications of CNOT gates will be found. As mentioned in Section 2, they are constructed as the product of the disjoint transpositions of the set of permutations  $P_{2^n}^{even}$  and  $P_{2^n}^{odd}$ . For instance, the  $n = 3$  case under consideration has to take into account the sets  $P_8^{even} = \{P_{(2,4)}, P_{(2,6)}, P_{(2,8)}, P_{(4,6)}, P_{(4,8)}, P_{(6,8)}\}$  and  $P_8^{odd} = \{P_{(2,3)}, P_{(2,5)}, P_{(2,7)}, P_{(4,5)}, P_{(4,7)}, P_{(6,7)}\}$ . These sets are divided into the  $2^{n-1} - 1 = 3$  subsets of disjoint

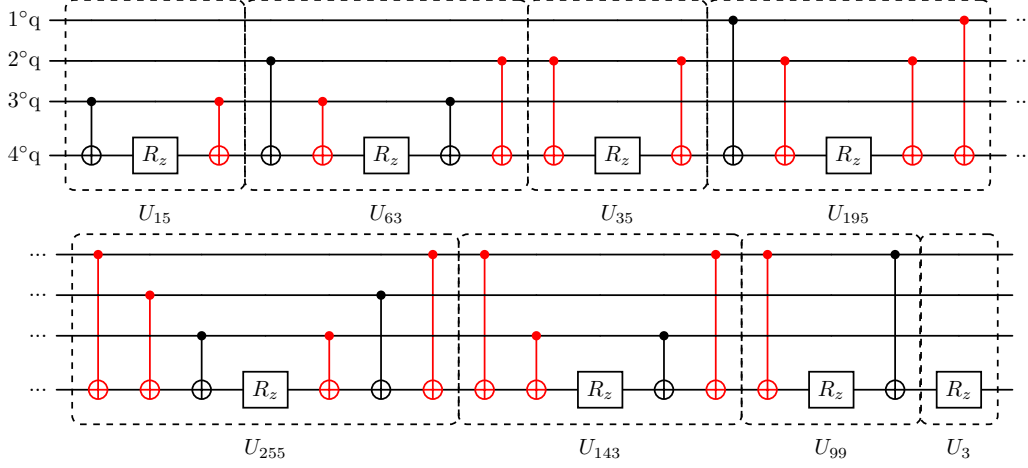


Figure 31: Simplifications (red gates) coming from new diagonal contributions only.

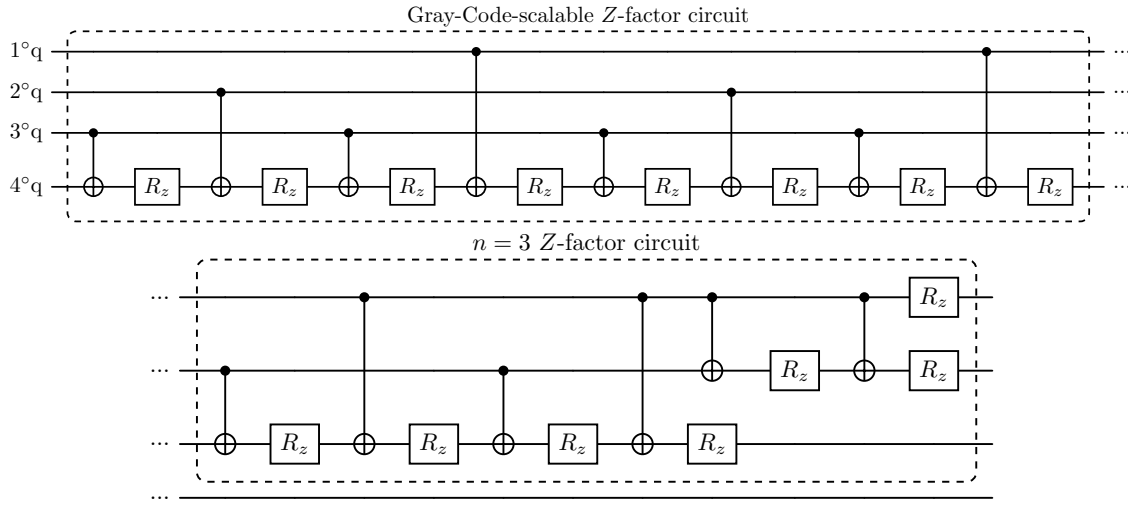


Figure 32: The  $Z(\Theta_Z)$ -factor circuit for  $n = 4$  with reduced CNOT-count.

transpositions, each of which contains  $2^{n-2} = 2$  elements:

$$\begin{aligned}
 \prod T_1^e &= P_{(2,4)}P_{(6,8)} & \prod T_1^o &= P_{(2,3)}P_{(6,7)} \\
 \prod T_2^e &= P_{(2,6)}P_{(4,8)} & \prod T_2^o &= P_{(2,5)}P_{(4,7)} \\
 \prod T_3^e &= P_{(2,8)}P_{(4,6)} & \prod T_3^o &= P_{(2,7)}P_{(4,5)}
 \end{aligned} \tag{84}$$

Similarly to the case of the Z-factor previously described, the simplifications occur due to the juxtaposition of CNOTs with the same control-target pair. Therefore, keeping in mind the general structure of the circuit (5) for one single layer ( $l = 1$ ), sequences of this type will appear within the  $\Psi$ -factor:

$$\mathcal{U}_{approx} = Z(\Theta_Z^1)[\dots][\left(\prod T_1^e\right) M_1^e \left(\prod T_1^o\right) \left(\prod T_2^e\right) M_2^e \left(\prod T_2^o\right) \left(\prod T_3^e\right) M_3^e \left(\prod T_3^o\right)]\Phi(\Theta_\Phi^1) \tag{85}$$

Simplifications can only occur between 2 edges of different macro-factors, as happens for  $\prod T_2^e$  and  $\prod T_3^e$  in the  $n = 3$  case. However, in the perspective of defining a general (and scalable) rule to find between which edges it is possible to simplify, a final binary scheme is mandatory. The latter consists of the binary table obtained by arranging the binary representation of numbers from 1 to  $2^{n-1} - 1 = 3$  in rows and considering  $n - 1$  qubits as columns. Then, reading the table from bottom to top (so as to follow the logical order in which the factors appear in the circuit), and comparing two consecutive lines at a time, a simplification occurs if the pair of binary strings has a 1 on the same bit. Consequently, the remaining CNOT gates are obtained by considering as targets the qubits corresponding to the bits which in the two strings takes on different values, while the control is always in the  $n$ -th qubit. Figure 33 illustrates this last step, highlighting in red the simplifications and in green the remaining CNOTs.

$x$	$1^\circ \text{ q}$	$2^\circ \text{ q}$	sub-factor
1	0	1	$\prod T_1^e$
2	1	0	$\prod T_2^e$
3	1	1	$\prod T_3^e$

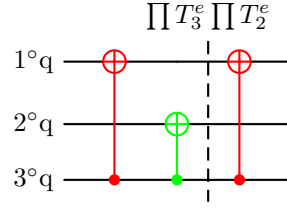


Figure 33: Simplification scheme for  $\prod T_x^e$  factors in the  $n = 3$  case; only the  $\prod T_3^e \prod T_2^e$  pair of edges shows simplifications.

**Proposition 6.** A CNOT-simplification between  $\prod T_x^{e/o}$  factors occurs if, in the correct logic order, these factors show pairs of bits with value 1 at the same position in the binary table that sort them.

*Proof.* The specific case for  $n = 3$ , described above as an example to clarify the conditions of simplification, has a completely general value since it is based on:

- i) the relationship between binary representation and the circuit implementation of  $\prod T_x^{e/o}$  contributions (defined in Section 3.1.1);
- ii) the properties of the binary representation valid for any  $n$ .

□

For the  $\prod T_x^o$  factors of the odd case, the considerations are completely similar and the same tabular scheme is used with one only difference: once a pair of binary strings appropriate for simplification has been found, the leftmost pair of bits equal to 1 determines the value of the parameter  $k$ , which only for the  $\prod T_x^o$  factors implies two CNOTs where the control-target pair is reversed. Figure 34 illustrates this last step, highlighting in red the simplifications and in green the remaining CNOTs. Besides, it is possible to simplify the search for edges suitable for simplifications restricting it to the even case, which turns out to be faster due to the absence of the parameter  $k$ , as stated by the following proposition.

**Proposition 7.** Once the pairs of edges with CNOT-simplifications of the even case have been found, in the odd case the same pairs will result.

*Proof.* Both even and odd cases rely on the same binary table, in which the  $\prod T_x^{e/o}$  factors are only ordered. The presence of the parameter  $k$  does not modify this ordering, but only adds a pair of CNOT gates with control-target qubits reversed, before and after the structure of the even case, for each value of  $x$ . Thus, in addition to the simplified pairs of the even case, there will always be an additional simplified pair of CNOTs, the ones placed side by side in the simplifying border. □

$x$	$1^\circ \text{ q}$	$2^\circ \text{ q}$	sub-factor	$k$
1	0	1	$\prod T_1^e$	2
2	1	0	$\prod T_2^e$	1
3	1	1	$\prod T_3^e$	1

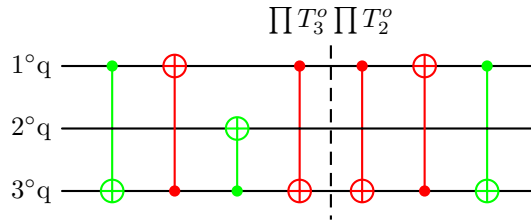


Figure 34: Simplification scheme for  $\prod T_x^o$  factors in the  $n = 3$  case; only the  $\prod T_3^o \prod T_2^o$  pair of edges shows simplifications.

Proposition 6 identifies a scalable method for the  $\Psi/\Phi$ -factor design, optimized in terms of CNOT gates thanks to simple binary matrices, as illustrated via pseudocode in Algorithm 2, 3, 4 and 5.

### 6.2.1 Solution for $n = 4$

In the case of 4-qubit systems, there are exactly  $2^{n-1} - 1 = 7$  factors of type  $\prod T_x^e$  inside  $\Psi(\Theta_\Psi)$  and the same number of type  $\prod T_x^o$  inside  $\Phi(\Theta_\Phi)$ . As described in Section 2, they are defined as the product of disjoint

---

**Algorithm 2 [PERMUTATION]** Circuit for a single  $\prod T_x^{e/o}$  factor,  $1 \leq x \leq 2^{n-1} - 1$ , parity = {even, odd}

---

- 1: **Provided:**  $CNOT(c, t)$  where  $c$  stands for control and  $t$  for target; the usual notation where the first qubit is labeled with 0.
  - 2: **Input:** binary array corresponding to the  $\prod T_x^{e/o}$  factor (see Figure 33); position  $x$  in the sequence of  $\prod T_x^{e/o}$  factors; array with  $k$ -index (see Figure 34).
  - 3: **Output:** circuit of the  $\prod T_x^{e/o}$  factor for a particular position  $x$ .
  - 4: **if** parity = even **then**
  - 5:     **for** element  $i$  in binary array **do**
  - 6:         **if** element  $i$  equals 1 **then**
  - 7:              $CNOT(n - 1, i)$
  - 8:         **else**
  - 9:             Pass
  - 10:         **end if**
  - 11:     **end for**
  - 12: **else**
  - 13:     Consider the element  $x$  of the array with  $k$ -index, i.e.,  $k_x$
  - 14:      $CNOT(k_x, n - 1)$
  - 15:     Run instructions for parity = even
  - 16:      $CNOT(k_x, n - 1)$
  - 17: **end if**
- 

---

**Algorithm 3 [ $\Psi$ -FACTOR-MAIN]** Scalable scheme for CNOT-simplifications within the alternating sequence of  $\prod T_x^e$  and  $M_x^e$  factors,  $1 \leq x \leq 2^{n-1} - 1$

---

- 1: **Provided:**  $CNOT$ -remaining-Gray (see Algorithm Z-FACTOR); an algorithm that generates the binary matrix, obtained by comparing two rows at a time of the *reverse* binary matrix that orders  $\prod T_x^e$  factors (see Figure 33), where the 1s indicate the positions in which the bits have different values (called  $CNOT$ -remaining-EvenEdges); a scalable algorithm for  $M_x^e$  circuits, called  $Me$ -factor-circuit.
  - 2: **Input:** set of parameters  $\theta_a \in \Theta_\Psi$ ; output of  $CNOT$ -remaining-Gray; output of  $CNOT$ -remaining-EvenEdges; output of  $Me$ -factor-circuit.
  - 3: **Output:** circuit for the 2nd sub-factor of  $\Psi$ , in the correct logic order but without  $\prod T_{x_{max}}^e$ ,  $\prod T_1^e$  and  $M_{x_{max}}^e$ , optimized in terms of  $CNOT$  gates.
  - 4: Consider the output of  $CNOT$ -remaining-EvenEdges, i.e., a binary matrix
  - 5: **for** row  $i$  in binary matrix **do**
  - 6:     **for** column  $j$  in row  $i$  **do**
  - 7:         **if** element  $(i, j)$  equals 1 **then**
  - 8:              $CNOT(n - 1, j)$
  - 9:         **else**
  - 10:             Pass
  - 11:         **end if**
  - 12:     **end for**
  - 13:     Run  $Me$ -factor-circuit
  - 14: **end for**
-

---

**Algorithm 4** [ $\Phi$ -FACTOR-MAIN] Scalable scheme for CNOT-simplifications within the alternating sequence of  $\prod T_x^o$  and  $M_x^o$  factors,  $1 \leq x \leq 2^{n-1} - 1$

---

1: **Provided:** *CNOT-remaining-Gray* (see Algorithm Z-FACTOR); an algorithm that generates the matrix, obtained by comparing two rows at a time of the *reverse* binary matrix that orders  $\prod T_x^o$  factors (see Figure 34), where the 1s indicate the positions in which the bits have different values, the 2s the positions in which the bits have value equals to 1, the 0s the remaining positions (called *CNOT-remaining-OddEdges*); a scalable algorithm for  $M_x^o$  circuits, called *Mo-factor-circuit*; Algorithm  $\Psi$ -FACTOR-MAIN.

2: **Input:** set of parameters  $\theta_a \in \Theta_\Phi$ ; output of *CNOT-remaining-Gray*; output of *CNOT-remaining-OddEdges*; output of *Mo-factor-circuit*; array with  $k$ -index (see Figure 34); output of Algorithm 3  $\Psi$ -FACTOR-MAIN.

3: **Output:** circuit for the  $\Phi$  factor, in the correct logic order but without  $\prod T_{x_{max}}^o$ ,  $\prod T_1^o$  and  $M_{x_{max}}^o$ , optimized in terms of *CNOT* gates.

4: Consider the output of *CNOT-remaining-OddEdges*, i.e., a matrix with entries  $\{0,1,2\}$

5: **for** row  $i$  in matrix **do**

6:   **for** column  $j$  in row  $i$  **do**

7:     **if** element  $(i, j)$  equals 2 **then**

8:       Consider the element  $i$  of the array with  $k$ -index, i.e.,  $k_i$

9:       *CNOT*( $k_i, n - 1$ )

10:      Run instructions from 6 to 12 of Algorithm  $\Psi$ -FACTOR-MAIN (with the output of *CNOT-remaining-EvenEdges*)

11:      *CNOT*( $k_i, n - 1$ )

12:      Run *Mo-factor-circuit*

13:      Break

14:     **else if** no element  $(i, j)$  equals 2 **then**

15:       This is an edge without CNOT-simplifications

16:       Run Algorithm PERMUTATION for  $x = i$  and parity = odd

17:       Run Algorithm PERMUTATION for  $x = i + 1$  and parity = odd

18:       Run *Mo-factor-circuit*

19:       Break

20:     **end if**

21:   **end for**

22: **end for**

---



---

**Algorithm 5** [ $\Psi/\Phi$ -FACTORS] Scalable CNOT-optimized  $\Psi(\Theta_\Psi)/\Phi(\Theta_\Phi)$ -factor circuit, parity = {even, odd}

---

**Provided:** Algorithm PERMUTATION, Algorithm  $\Psi$ -FACTOR-MAIN and Algorithm  $\Phi$ -FACTOR-MAIN.

**Input:** set of parameters  $\theta_a \in \{\Theta_\Psi \cup \Theta_\Phi\}$ ;  $x_{max} = 2^{n-1} - 1$ ; outputs of Algorithms PERMUTATION, Algorithm  $\Psi$ -FACTOR-MAIN and Algorithm  $\Phi$ -FACTOR-MAIN.

**Output:**  $\Psi$ -factor and  $\Phi$ -factor circuits, in the correct logic order and optimized in terms of *CNOT* gates.

**if** parity = even **then**

  Run Algorithm PERMUTATION for  $x = x_{max}$  and parity = even

  Run *Me-factor-circuit* (for  $x = x_{max}$ )

  Run Algorithm  $\Psi$ -FACTOR-MAIN

  Run Algorithm PERMUTATION for  $x = 1$  and parity = even

  Run *Me-factor-circuit* (for the 1st sub-factor of  $\Psi$ )

**else**

  Run Algorithm PERMUTATION for  $x = x_{max}$  and parity = odd

  Run *Mo-factor-circuit* (for  $x = x_{max}$ )

  Run Algorithm  $\Phi$ -FACTOR-MAIN

  Run Algorithm 2 PERMUTATION (for  $x = 1$  and parity = odd)

**end if**

---

2-cycles from the set of permutations  $P_{16}^{even}$  and  $P_{16}^{odd}$ , respectively. However, for the purposes of this Section, it is more useful to use their representation in terms of CNOTs<sup>27</sup>:

$$\begin{aligned}
\prod T_1^e &= CNOT_{(4,3)} & \prod T_1^o &= CNOT_{(3,4)} \prod T_1^e CNOT_{(3,4)} \\
\prod T_2^e &= CNOT_{(4,2)} & \prod T_2^o &= CNOT_{(2,4)} \prod T_2^e CNOT_{(2,4)} \\
\prod T_3^e &= CNOT_{(4,2)} CNOT_{(4,3)} & \prod T_3^o &= CNOT_{(2,4)} \prod T_3^e CNOT_{(2,4)} \\
\prod T_4^e &= CNOT_{(4,1)} & \prod T_4^o &= CNOT_{(1,4)} \prod T_4^e CNOT_{(1,4)} \\
\prod T_5^e &= CNOT_{(4,1)} CNOT_{(4,3)} & \prod T_5^o &= CNOT_{(1,4)} \prod T_5^e CNOT_{(1,4)} \\
\prod T_6^e &= CNOT_{(4,1)} CNOT_{(4,2)} & \prod T_6^o &= CNOT_{(1,4)} \prod T_6^e CNOT_{(1,4)} \\
\prod T_7^e &= CNOT_{(4,1)} CNOT_{(4,2)} CNOT_{(4,3)} & \prod T_7^o &= CNOT_{(1,4)} \prod T_7^e CNOT_{(1,4)}
\end{aligned} \tag{86}$$

To find between which edges it is possible to simplify CNOT pairs, the table described in the previous Section is constructed (note that the table should be read from the bottom and in the odd case it has an extra column for the index  $k$ ). The resulting gates are shown in Figure 35 for the even case and in Figure 36 for the odd one. Since for  $n = 4$  the edges suitable for simplifications are four in both cases, the rows of the tables are partitioned for clarity.

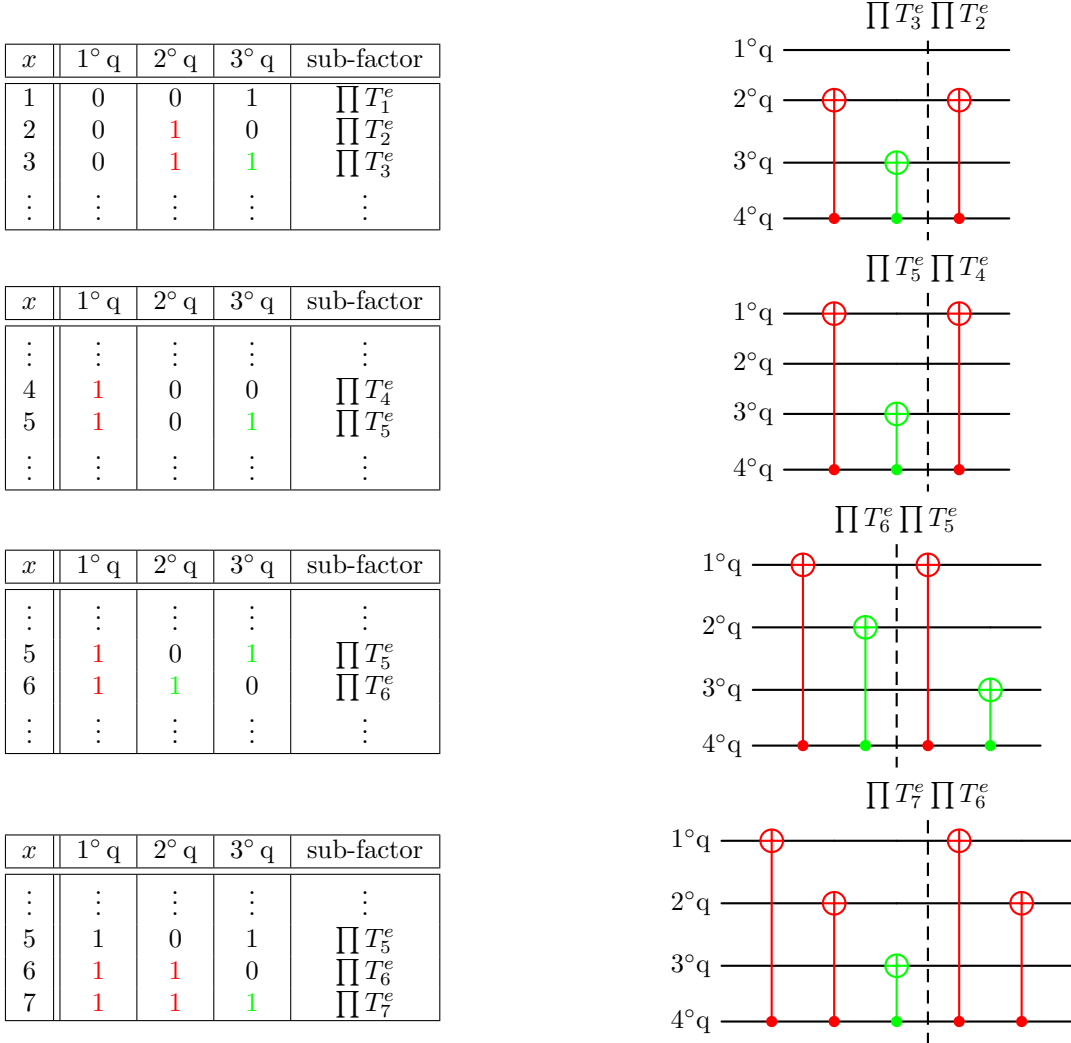


Figure 35: Simplification scheme for  $\prod T_x^e$  factors for  $n = 4$  case.

<sup>27</sup>As usual, the first label of the pair stands for the control qubit and second one for the target.

$x$	$1^\circ q$	$2^\circ q$	$3^\circ q$	sub-factor	$k$
1	0	0	1	$\prod T_1^o$	3
2	0	1	0	$\prod T_2^o$	2
3	0	1	1	$\prod T_3^o$	2
$\vdots$	$\vdots$	$\vdots$	$\vdots$	$\vdots$	$\vdots$

$x$	$1^\circ q$	$2^\circ q$	$3^\circ q$	sub-factor	$k$
$\vdots$	$\vdots$	$\vdots$	$\vdots$	$\vdots$	$\vdots$
4	1	0	0	$\prod T_4^e$	1
5	1	0	1	$\prod T_5^e$	1
$\vdots$	$\vdots$	$\vdots$	$\vdots$	$\vdots$	$\vdots$

$x$	$1^\circ q$	$2^\circ q$	$3^\circ q$	sub-factor	$k$
$\vdots$	$\vdots$	$\vdots$	$\vdots$	$\vdots$	$\vdots$
5	1	0	1	$\prod T_5^o$	1
6	1	1	0	$\prod T_6^o$	1
$\vdots$	$\vdots$	$\vdots$	$\vdots$	$\vdots$	$\vdots$

$x$	$1^\circ q$	$2^\circ q$	$3^\circ q$	sub-factor	$k$
$\vdots$	$\vdots$	$\vdots$	$\vdots$	$\vdots$	$\vdots$
5	1	0	1	$\prod T_5^o$	1
6	1	1	0	$\prod T_6^o$	1
7	1	1	1	$\prod T_7^o$	1

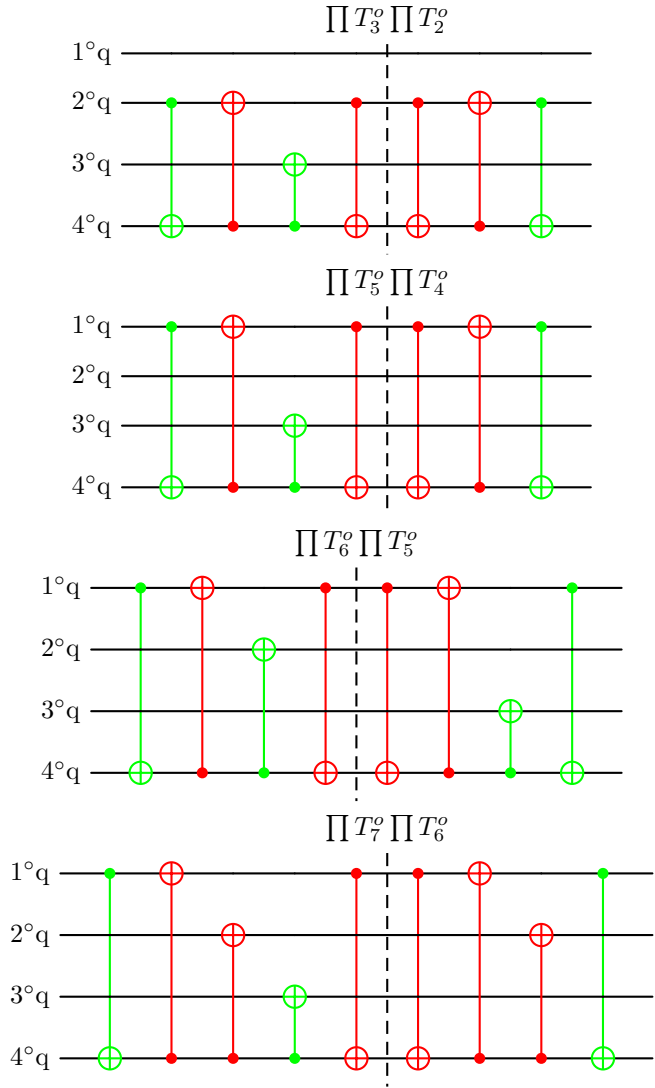


Figure 36: Simplification scheme for  $\prod T_x^o$  factors for  $n = 4$  case.

Finally, the simplification algorithms proposed above can be merged into an overall algorithm (see Algorithm 6) for the scalable (and partially recursive) construction of the CNOT-optimized VQC for the approximation of  $SU(2^n)$  operators.

---

**Algorithm 6 [SU-SYNTHESIS]** CNOT-optimized circuit to approximate  $SU(2^n)$  operators within SRBB-framework

---

**Provided:** CNOT-optimized circuit for  $n = 2$ , Algorithm  $\Psi/\Phi$ -FACTORS and Algorithm Z-FACTOR.

**Input:** number of qubits  $n \geq 2$ ; set of parameters  $\theta_i \in \{\Theta_Z \cup \Theta_\Psi \cup \Theta_\Phi\}$ ; outputs of Algorithm  $\Psi/\Phi$ -FACTORS and Algorithm Z-FACTOR.

**Output:** complete circuit, optimized in terms of CNOT gates, to approximate a given special unitary matrix.

Partition of the entire set of parameters into three subsets, those for  $\Theta_Z$ ,  $\Theta_\Psi$  and  $\Theta_\Phi$

**if**  $n = 2$  **then**

CNOT-optimized circuit for  $n = 2$  (see Figure 10, outside the scalability pattern)

**else**

Run Algorithm  $\Psi/\Phi$ -FACTORS for parity = odd

Run Algorithm  $\Psi/\Phi$ -FACTORS for parity = even

Run Algorithm Z-FACTOR

**end if**

---

### 6.3 CNOT-reduced quantum circuit to approximate SU operators with SRBB-decomposition

The scalable simplification algorithm, valid for any  $n \geq 3$ , has been successfully incorporated into the original scalability scheme [33] reducing the number of CNOTs of the overall circuit. In light of the anomalous behavior for  $n = 2$ , which will be explained below in section 6.3.2, the implementation of the recursive construction of the SRBB represents a useful tool for visualizing the algebraic elements and verifying their fundamental group properties.

**Proposition 8.** *The following formulas are obtained for gates count after the scalable CNOT-simplification procedure on the approximate SRBB-based synthesis algorithm when  $n \geq 3$ :*

$$\begin{aligned} N_{CNOT} &= 2^{2n+1} - 5 \cdot 2^{n-1} + 2n - 4 \\ N_{Rot} &= 2^{2n+1} - 5 \cdot 2^{n-1} + 1 \\ CNOT_{red} &= 2^n(2n - 5) - 2n + 8 \end{aligned} \quad (87)$$

where the first and the second equations represent, respectively, the exponential trend of the total number of CNOT-gates and rotations (both z- and y-rotations), while the last one calculates the reduction of CNOT-gates compared to the original structure proposed by the literature. For the anomalous case  $n = 2$ , instead, it is found:

$$\begin{aligned} N_{CNOT} &= \frac{3}{2} \cdot 4^n + \left(n - \frac{3}{2}\right) 2^n - 8 = 18 \\ N_{Rot} &= \frac{3}{2} \cdot 4^n - 2^{n-1} - 1 = 21 \\ CNOT_{red} &= 4 \end{aligned} \quad (88)$$

For the length and modularity features of proofs, these trends are proven in the next Sections 6.3.1 and 6.3.2.

#### 6.3.1 Proof of gate count formulas

For general  $n$ , defining the overall function that describes the number of CNOT-gates after the simplification process means adding all the relevant contributions, as they appear in the original structure, and then subtracting the simplified quantity<sup>28</sup>:

$$\begin{aligned} N_{CNOT} &= N_{CNOT}(Z) + N_{CNOT}(\text{1st subfactor of } \Psi) + N_{CNOT}(M_x^e) + N_{CNOT}\left(\prod T_x^e\right) + \\ &+ N_{CNOT}(M_x^o) + N_{CNOT}\left(\prod T_x^o\right) - N_{CNOT}\left(\text{simplif. } \prod T_x^e\right) - N_{CNOT}\left(\text{simplif. } \prod T_x^o\right) \end{aligned} \quad (89)$$

---

<sup>28</sup>In this way, the formula describing the difference in terms of CNOTs with respect to the original structure will be obtained accordingly.



where  $N_{CNOT}(\text{simplif. } \prod T_x^{e/o})$  represents the number of simplified CNOTs inside factors  $\prod T_x^{e/o}$  and the simplifications within the  $Z$ -factor are not included because from  $n \geq 3$  the term  $N_{CNOT}(Z)$  already takes them into account. In the following, each term will be analyzed separately and then added only at the end.

□  $N_{CNOT}(Z)$

As anticipated, this term represents the number of resulting CNOTs after the simplifications only for  $n \geq 3$ . With reference to Section 6.1.1, the number of CNOT-gates for each  $Z$ -factor corresponds to the  $2^{n-1}$  jumps among the rows ending with 1 in the cyclic Gray Code matrix. Considering the recursive pattern within the diagonal contributions, the overall number of CNOTs for the case  $n$  in question is equivalent to the series:

$$\sum_{m=2}^n 2^{m-1} = \left( \sum_{m=0}^n 2^{m-1} \right) - \frac{3}{2} = 2^n - 2 \quad (90)$$

To calculate the effect of the simplification process with respect to the original structure, it is also very useful to calculate the number of CNOTs of the diagonal factor without the simplifications. The latter corresponds to double the number of 1-valued bits within the columns of the control qubits (all except the last one, associated to parameters  $m'$ ) in the binary tables that build the  $Z$ -factor circuit. This method analyzes the binary tables by columns and takes advantage of the fact that in each column there is the same number of 1s, even if they are grouped differently. In formulas it is worth that:

$$2 \sum_{n=2}^M 2^{M-n} (2^{n-1} - 1) = 2^M (M + 2) + 2 - 2^{M+2} = 2^M (M - 2) + 2 \quad (91)$$

where  $M = n_{max}$ ,  $2^{M-n}$  is the number of subgroups in each column and  $2^{n-1} - 1$  is the number of 1s associated to  $m'$  in each subgroups. This result allows to directly calculate the number of CNOT-simplifications within the  $Z$ -factor for  $n \geq 3$  ( $M = n_{max} \rightarrow n$ ):

$$[2^n(n-2) + 2] - (2^n + 2) = 2^n(n-3) + 4 \quad (92)$$

□  $N_{CNOT}(\text{1st subfactor of } \Psi) + N_{CNOT}(M_x^e)$

These two factors are analyzed together because the number of CNOTs contained in them depends on the  $ZYZ$ -decomposition property that they both satisfy. As explained in [33], a  $M_n ZYZ$ -type matrix can be fully decomposed and implemented through  $3 \cdot 2^{n-1} - 2$  CNOT-gates. Thus, considering the  $2^{n-1} - 1$  factors of type  $M_x^e$  plus the first sub-factor of  $\Psi(\Theta_\Psi)$  that fall into this decomposition, the total number of CNOTs is  $2^{n-1}(3 \cdot 2^{n-1} - 2)$ .

□  $N_{CNOT}(M_x^o)$

Due to their algebraic properties, these sub-factors cannot be implemented with a pure  $ZYZ$ -decomposition, but multi-controlled  $z$ -rotations must be added before and after a  $ZYZ$ -type kernel [33]. For this reason, the total number of CNOTs is  $(2^{n-1} - 1)(5 \cdot 2^{n-1} - 6)$ .

□  $N_{CNOT}(\prod T_x^e)$

With reference to the binary tables used to built the corresponding quantum circuits for these factors, the total number of CNOTs is equivalent to double the number of 1-valued bits, remembering that target columns are  $n - 1$ . Thus, in each column there are exactly  $2^{n-2}$  1-valued bits and the formula for the total number of CNOTs within these factors is  $2(n-1)2^{n-2}$ .

□  $N_{CNOT}(\prod T_x^o)$

For these factors the same rules apply as for the even case with only one difference due to their very definition (presence of the parameter  $k$ ): the total number of CNOTs is equal to the number of CNOTs for the even case plus the number of pairs  $\text{CNOT}_{(k,n)}$ . The final formula is  $2[(n-1)2^{n-2} + 2(2^{n-1} - 1)]$ .

□  $N_{CNOT}(\text{simplif. } \prod T_x^e)$

To calculate the number of simplifications inside  $\prod T_x^e$  factors it is absolutely important to understand the recursive pattern with which pairs of 1s (simplifications) appear in the binary tables that encode these factors. In Figure 37, this pattern is illustrated for  $n = 3, 4, 5$  to simplify the explanation. Firstly, the 1s highlighted in red form the pairs indicating the simplifications according to the rule already explained in Section 6.2; secondly, the entire table is divided into two blocks by a horizontal line that partitions it exactly in half: it is immediate to observe that the number of simplifications of case  $n$  corresponds to the number of simplifications present in the upper half of the table of case  $n + 1$ . Finally, the number

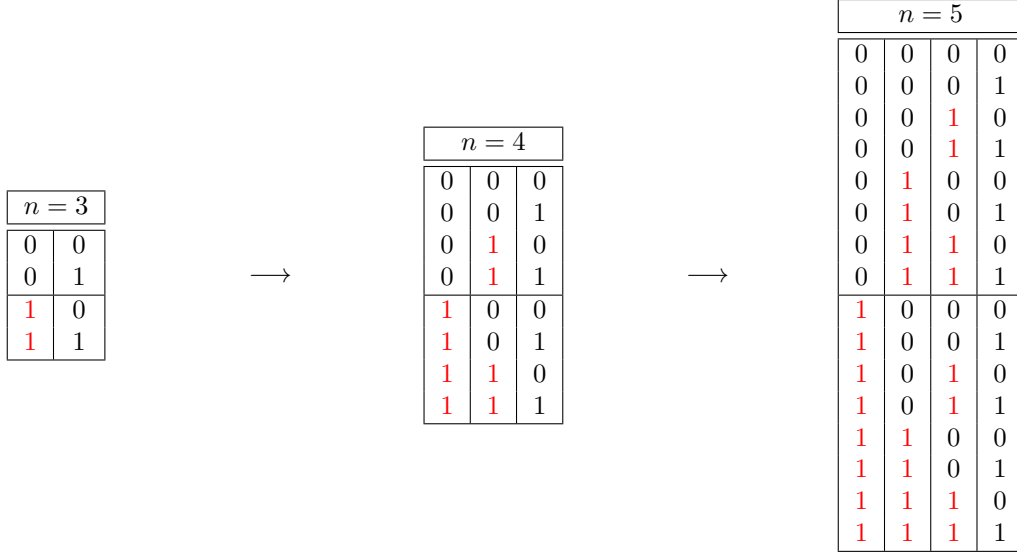


Figure 37: Recursive scheme for simplification within  $\prod T_x^e$  factors.

of simplifications (pairs of 1) of the lower half equals  $2^{n-2} - 1$  and a fraction of these, more precisely all except those of the first column, are equal to those of the upper half. Thus, introducing the function

$$f_{max}(i) = 2^{n_{max}-2-i} - 1 \quad (93)$$

it is possible to count the total number of pairs of (vertically) adjacent 1-valued bits (CNOT-simplifications) through the formula

$$\sum_{i=0}^{n_{max}-3} 2^i \cdot f_{max}(i) \quad (94)$$

and, multiplying by 2, obtain the corresponding number of CNOTs ( $n_{max} \rightarrow n$ ):

$$\begin{aligned} N_{CNOT}(\text{simplif. } \prod T_x^e) &= 2 \left( \sum_{i=0}^{n-3} 2^i \cdot f_{max}(i) \right) = \sum_{i=0}^{n-3} 2^{i+1} (2^{n-2-i} - 1) = \\ &= \sum_{i=0}^{n-3} 2^{n-1} - \sum_{i=0}^{n-3} 2^{i+1} = 2^{n-1} (n-3) + 2 \end{aligned} \quad (95)$$

□  $N_{CNOT}(\text{simplif. } \prod T_x^o)$

For the odd case the same type of analysis applies, but a contribution must be added for the simplifications that come from the pairs of 1s added by the parameter  $k$ . Remembering the definition of the parameter  $k$ , which in Figure 37 corresponds to calculating the number of pairs that can be created with the leftmost 1s in each row, the function  $f_{max}(i)$  introduced for the even case can be used to derive the number of simplifications even in the odd case:

$$\begin{aligned} N_{CNOT}(\text{simplif. } \prod T_x^o) &= N_{CNOT}(\text{simplif. } \prod T_x^e) + 2 \sum_{i=3}^n f_i(0) = \\ &= 2^{n-1} (n-3) + 2 + 2 \sum_{i=3}^n (2^{i-2} - 1) = \\ &= 2^{n-1} (n-3) + 2 - 2n + 4 + \frac{1}{2} \left( \sum_{i=0}^n 2^i - \sum_{i=0}^2 2^i \right) = 2^n - 2n \end{aligned} \quad (96)$$

Putting everything together, the number of CNOTs expressed by the first of equations (87) is proven.

To deduce the total number of rotations  $N_{Rot}$ , the second of equations (87), the following contributions must be considered:

$$N_{Rot} = N_{Rot}(Z) + N_{Rot}(\text{1st subfactor of } \Psi) + N_{Rot}(M_x^e) + N_{Rot}(M_x^o) \quad (97)$$

Below, each term will be analyzed separately and then added only at the end.

□  $N_{Rot}(Z)$

In the  $Z$ -factor, the number of rotation is very simple since it corresponds to the number of diagonal elements involved, that is  $2^n - 1$ .

□  $N_{Rot}(\text{1st subfactor of } \Psi)$

Thanks to its algebraic properties that allow a complete  $ZYZ$ -decomposition, this factor has exactly  $3 \cdot 2^{n-1}$  rotations.

□  $N_{Rot}(M_x^e)$

Again due to decomposition properties, each factor of type  $M_x^e$  has  $3 \cdot 2^{n-1}$  rotations. Thus, the total number is simply  $3(2^{n-1} - 1)2^{n-1}$ .

□  $N_{Rot}(M_x^o)$

As explained in [32], a block-diagonal unitary matrix with  $U(2)$  blocks can be decomposed by appropriately modifying the structure of a  $ZYZ$ -type matrix. This modification involves the addition of  $n - 2$  multi-controlled  $z$ -rotations and 1  $z$ -rotations, before and after the central  $ZYZ$ -core. Considering that, as for the even case, there are  $2^{n-1} - 1$  factors of this type, the total number of rotations in the odd case is expressed by the equation:

$$(2^{n-1} - 1) \left[ 2 \sum_{m=0}^{n-2} 2^m + 3 \cdot 2^{n-1} \right] = (2^{n-1} - 1)(5 \cdot 2^{n-1} - 2) \quad (98)$$

where the total number of  $y$ -rotations is  $(2^{n-1} - 1) \cdot 2^{n-1}$  since in the  $ZYZ$ -core there is only one multi-controlled  $y$ -rotation with  $2^{n-1}$  controls and the total number of  $z$ -rotations is instead

$$(2^{n-1} - 1) \cdot \left( 2 \sum_{m=0}^{n-1} 2^m \right) = 2(2^n - 1)(2^{n-1} - 1) \quad (99)$$

Putting everything together, the number of rotations expressed by the second of equations (87) is proven.

Finally, the last of equations (87) concerning the reduction in terms of CNOT-gates with respect to the original structure proposed in [33] is easily derived from the contributions already computed:

$$\begin{aligned} CNOT_{red} &= N_{CNOT}(\text{simplif. } Z) + N_{CNOT} \left( \text{simplif. } \prod T_x^e \right) + N_{CNOT} \left( \text{simplif. } \prod T_x^o \right) = \\ &= 2^n(n - 3) + 4 + 2[(n - 3)2^{n-1} + 2] + 2^n - 2n = \\ &= 2^n(2n - 5) - 2n + 8 \end{aligned} \quad (100)$$

valid from  $n \geq 3$ .

### 6.3.2 Anomaly for $n = 2$

Sections 2, 3, 4 provide all the elements to understand how the  $n = 2$  case falls out the scalability pattern. There are essentially two reasons: the  $M_1^o$  sub-factor is a  $M_2 ZYZ$ -type matrix only for  $n = 2$  and only with 2 qubits the  $Z(\Theta_Z)$ -factor admits simplifications with  $\Psi(\Theta_\Psi)$ -factor. In the first case, the exception to the scalability is due to the fact that from  $n = 3$  onwards, the  $M_x^o$  sub-factors can all be implemented as block diagonal unitary matrices with unitary blocks (not  $SU(2)$  blocks as for  $M_n ZYZ$ -type matrices). Their implementation requires a different pattern, which starts and ends with a rotation gate, preventing simplifications with the adjacent CNOTs of others sub-factors (see for instance Figure 17). In the second case the explanation is simpler: by implementing both  $\Psi(\Theta_\Psi)$ - and  $Z(\Theta_Z)$ -factors through cyclic Gray Code<sup>29</sup>,  $\Psi(\Theta_\Psi)$  ends with a  $\text{CNOT}_{(1,n)}$ , where the first subscript stands for control, while  $Z(\Theta_Z)$  starts with a  $\text{CNOT}_{(n-1,n)}$ , preventing simplification from  $n \geq 3$  (see for instance the difference between Figures 10 and 14).

To complete the analysis of this particular case, equations (88) is demonstrated below. Since the underlying approximation algorithm is expressed by the same key equation (5), for each of the equations (88) the same contributions of the  $n \geq 3$  cases were taken into consideration. What changes are the algebraic properties of these contributions and therefore their implementation and the consequent possible simplifications.

□  $N_{CNOT}(Z)$

In this case, the formula  $2^n - 2 = 2$  counts the precise number of CNOT-gates *before* the simplification procedure (and not after as for  $n \geq 3$  cases).

<sup>29</sup>The first because it is composed of  $M_n ZYZ$  matrices and the second to reach the smallest number of CNOTs as previously described.

$$\square N_{CNOT}(1^\circ \text{ subfactor of } \Psi) + N_{CNOT}(M_x^{e/o})$$

As explained above, only for  $n = 2$  the  $M_1^o$  factor has a complete  $ZYZ$ -decomposition too, so that the structure of the overall circuit is characterized by sequences of  $ZYZ$ -type matrices. In addition to the  $1^\circ$  sub-factor of  $\Psi$ , the circuit counts  $2^{n-1} - 1 = 1$  contribution for the even case and  $2^{n-1} - 1 = 1$  contribution for the odd case. Thus, a total of  $(2^n - 1)(3 \cdot 2^{n-1} - 2) = 12$ .

$$\square N_{CNOT}\left(\prod T_x^{e/o}\right)$$

For both the even and odd cases, the same trends obtained for  $n \geq 3$  apply to these factors:  $2(n-1)2^{n-2} = 2$  for the even case and  $2[(n-1)2^{n-2} + 2(2^{n-1} - 1)] = 6$  for the odd case.

$$\square CNOT_{red}$$

From the circuit illustrated in Figure 10, it is possible to count the 4 simplified CNOTs for this particular and anomalous case.

Putting everything together, the number of CNOT-gates expressed by the first of equations (88) is proven.

As regards the total number of rotations in the  $n = 2$  case, the calculation is very simple given the repetition of  $2^n - 1$   $ZYZ$ -decompositions in addition to  $2^n - 1$  diagonal elements:

$$(3 \cdot 2^{n-1})(2^n - 1) + 2^n - 1 = 21 \quad (101)$$

## 7 Implementation and Results

The proposed scalable VQC has been implemented using the PennyLane library [35]. All the tests described in this section have been performed using the simulator provided by the same library, executed on a Linux machine equipped with an AMD EPYC 7282 CPU and 256 GB RAM.

Some tests (illustrated in Section 7.2) have been performed using IBM quantum computers, namely IBM Brisbane [36] and IBM Fez [37].

The QNN is utilized to approximate ideal circuits, from which the associated unitary matrices are retrieved. Since, the approximating algorithm operates with  $SU$  matrices, the  $SU(2^n)$  associated to the  $U(2^n)$  must be computed by dividing the ideal unitary matrix by its determinant, as previously explained in Section 2.

The parameters of the VQC are updated to minimize the cost function. In this work, different losses are tested:

- Frobenius norm:  $\|A\|_F = \sqrt{\text{tr}(AA^\dagger)}$ ,

where  $A = SU_{ideal} - SU_{VQC}$

- Trace distance:  $\|\rho - \sigma\|_1 = \text{tr} \sqrt{(\rho - \sigma)^\dagger (\rho - \sigma)}$

- Fidelity:  $F(\rho, \sigma) = (\text{tr} \sqrt{\sqrt{\rho}\sigma\sqrt{\rho}})^2$ ,

where  $\rho$  and  $\sigma$  are the density matrices of the states obtained by the ideal  $SU$  operation, which will be approximated, and by the VQC, respectively, given the same input state.

When the Frobenius norm is used as loss function, the VQC is constructed to obtain its matrix representation and the Frobenius distance is calculated to get the value of the loss. The Frobenius norm is applied to compare the  $SU(2^n)$  associated to the circuit that the QNN should approximate and the  $SU(2^n)$  associated to the VQC. Instead, when the fidelity or the trace distance are used, a training set with 1000 random states is created to perform the minimization of the loss function, in order to decrease (increase) the value of the trace (fidelity) of the states obtained by the ideal matrix and the approximated matrix.

However, a problem arises when the network is trained using fidelity or trace distance, since density matrices make use of the square moduli of the amplitudes nullifying the contribution of the phases that establishes the relationship between the special unitary group and the unitary one, as previously explained in Section 2. Thus, to recover the phase contribution, the following procedure has been implemented:

- the  $2^n$  roots of the determinant are calculated;
- the roots are associated with the  $2^n$  possible  $SU(2^n)$  matrices;
- after training, the distance between the approximated  $SU(2^n)$  matrix returned by the network and each possible  $SU(2^n)$  matrix is computed;

- finally, the approximated  $U(2^n)$  is computed multiplying the approximated  $SU(2^n)$  by the root associated with the ideal  $SU(2^n)$  that has the smallest distance.

The samples of the dataset are encoded utilizing the amplitude encoding. This scheme encodes a classical data  $x$  in a quantum state by associating the normalized features with the probability amplitudes of the quantum state. Given  $x = (x_1, x_2, \dots, x_N)^T$ , with  $N = 2^n$ , the quantum state is as follows:

$$U_\phi(x) : x \in \mathbb{R}^N \longrightarrow |\phi(x)\rangle = \frac{1}{\|x\|} \sum_{i=1}^N x_i |i\rangle, \quad (102)$$

where  $|i\rangle$  is the  $i$ th computational basis.

The optimization is performed using two different optimizers:

- Adam, which is a classical optimizer based on the gradient descent; the learning rate is 0.01 and, when the trace or fidelity are used, the number of epochs are 20 and the batch size is 64;
- Nelder Mead, which is used only with the Frobenius loss.

## 7.1 Tests with Quantum Circuit Simulation

The QNN has been tested with different numbers of qubits, from 2 to 6. Initially, it has been tested with predefined circuits, which are shown in Table 17 and depicted in appendix A, which are divided based on the number of qubits. In the definition of the circuits, the subscript number indicates the control/target qubit, while the superscript number indicates the control activation value. Then, the QNN has also been tested with random  $SU(2^n)$  matrices. The results obtained with Adam are shown in Table 18, where "circuits" indicates the circuits implemented in Table 17, while, "random" indicates the  $SU(2^n)$  matrices that are generated randomly. The execution time has been measured with respect to the Frobenius loss. For 6 qubits, the results of fidelity and trace are not included because the algorithm takes days. In general, the algorithm achieved a low value for the loss function up to 5 qubits, meaning a suitable approximations of the ideal matrices. The results show that the precision decreases when the number of qubits increases. This may result from the optimization process and the increased number of gates, which can create a more complex parametric landscape with additional local minima. Furthermore, for the same number of qubits, the performance worsens when using random matrices. This suggests that having sparse matrices or matrices with specific patterns simplifies the approximation for the QNN. In any case, the best performance is achieved after just 10 epochs and with only one single layer of the QNN.

An example of the execution with the Adam optimizer of an approximate predefined circuit and an approximate random unitary matrix is provided for 2 qubits in appendix B.

In Table 19, a comparison of the results for 2-qubit circuits is presented with those from [32] and the results obtained using [38] with our method (QNN optimized by using Adam or Nelder Mead). When the Adam optimizer was used, although the network achieved a lower accuracy compared to the results reported by [32], it demonstrated significantly reduced training times. This is a notable outcome, as it can help to obtain a coarse approximation of larger matrices in a reasonable time. Furthermore, when the Nelder Mead optimizer was used (as in [32]), the QNN achieved better results in both approximation error and time taken. The network can produce significant results in a short amount of time. Moreover, our method was also applied to the two-qubit optimal circuit of Vidal [38], where it achieved slightly worse performance. Additionally, the last row shows the results obtained with a random unitary. The network is able to achieve notable results in about 1 minute with the Nelder Mead optimizer and, in this case, the performance with [38] circuit are much worse.

In Table 20, a comparison of the results for 3-qubit circuits is presented with those from [32] and [30]. Also in this case, the network achieved superior results with Nelder Mead. The training times with Nelder Mead are significantly higher compared to the 2 qubits scenario, but the network can achieve better results than the other 2 methods. However, when Adam is used, the training times remain low, providing a fast way to achieve a coarse approximation of circuits.

In Table 21, a comparison of the results for 4-qubit circuits is presented with those from [32, 30]. The network achieved the same or even better accuracy of the other methods, except for the Grover algorithm, but its training times do not scale efficiently. Using Nelder Mead, given sufficient time, it can achieve the same performance of the other methods, therefore the focus should be on comparing the training time required to reach that approximation.

Table 22 presents the results of the verification of the density matrix evolution theorem, through the Liouville-Von Neumann equation:

$$\frac{\partial \rho}{\partial t} = \frac{-i}{\hbar} [H, \rho] \quad (103)$$

n = 2	n = 3	n = 4	n = 5, 6
$C_0^1 X_1$	$C_0^1 X_1 H_2$	$C_0^1 X_1 \cdot C_2^1 X_3$	<i>QFT5/6</i>
$C_1^1 X_0$	$C_0^1 X_1 I_2$	$C_1^1 X_0 \cdot C_3^1 X_2$	<i>Grover5/6</i>
$C_0 T_1$	$I_0 C_2^1 X_1$	$C_0^1 X_1 \cdot C_0^1 X_2 \cdot C_0^1 X_3$	–
$C_0 S_1$	$C_0^1 X_2$	$C_1^1 X_0 \cdot C_0^1 X_2 \cdot C_2^1 X_3 \cdot C_3^1 X_1$	–
$X_0 X_1$	$C_2^1 X_0$	$H_0 I_{1,2,3} \cdot C_0^1 X_1 I_{2,3} \cdot I_0 H_1 I_{2,3} \cdot I_0 C_1^1 X_2 I_3 \cdot I_{0,1} H_2 I_3 \cdot I_{0,1} C_2^1 X_3$	–
$Y_0 Y_1$	$C_0^1 X_1 X_2$	$H_0 H_1 I_2 I_3 \cdot I_0 C_1^1 X_2 I_3 \cdot I_0 I_1 H_2 H_3$	–
$Z_0 Z_1$	$C_0^1 X_1 Y_2$	$H_0 H_1 H_2 H_3 \cdot X_0 Y_1 Z_2 X_3$	–
$X_0 Z_1$	$C_0^1 X_1 Z_2$	$SWAP_{0,1} \sqrt{X_2} I_3 \cdot I_0 I_1 C_2^1 X_3$	–
$Z_0 X_1$	$X_0 X_1 X_2$	$ISWAP_{0,1} I_2 I_3 \cdot I_0 C_1^1 X_2 I_3 \cdot I_{0,1} C_2^1 S_3$	–
$Z_0 Y_1$	$X_0 Y_1 X_2$	$C_0^1 C_1^1 C_2^1 X_3$	–
$H_0 H_1$	$X_0 Y_1 Z_2$	$C_0^0 C_1^1 C_2^0 X_3$	–
$H_0 I_1$	$H_0 H_1 H_1$	$C_0^0 C_1^1 C_2^0 RY(\frac{\pi}{4})_3$	–
$X_0 X_1 \cdot Y_0 Y_1$	$I_0 C_1^1 X_2 \cdot C_0^1 X_1 I_2$	<i>Toffoli</i> <sub>0,1,2</sub> $I_3$	–
<i>SWAP</i> <sub>0,1</sub>	$I_0 C_2^1 X_1 \cdot C_1^1 X_0 I_2$	$X_0 C_1^1 X_2 Y_3 \cdot C_0^1 X_1 Y_2 X_3$	–
<i>SISWAP</i>	$C_0^1 X_2 \cdot I_0 C_1^1 X_2$	<i>QFT4</i>	–
<i>ISWAP</i>	<i>Toffoli</i>	<i>Grover4</i>	–
$H_0 I_1 \cdot C_0^1 X_1$	$C_0^0 C_1^0 X_2$	–	–
$\frac{1}{2} \sqrt{X_0} I_1$	$X_0 C_1^1 X_2 \cdot C_0^1 X_1 Y_2$	–	–
<i>Grover2</i>	$H_0 H_1 H_2 \cdot X_0 Y_1 X_2$	–	–
<i>QFT2</i>	$H_0 H_1 H_2 \cdot X_0 Y_1 Z_2$	–	–
–	$H_0 H_1 H_2 \cdot X_0 X_1 X_2$	–	–
–	$H_0 X_1 X_2 \cdot I_0 Y_1 Z_2$	–	–
–	$H_0 I_1 I_2 \cdot C_0^1 X_1 I_2 \cdot I_0 H_1 I_2 \cdot I_0 C_1^1 X_2$	–	–
–	$\sqrt{X_0} I_1 I_2 \cdot I_0 H_1 H_2 \cdot Y_0 C_1^1 S_2$	–	–
–	$C_0^1 C_1^0 RY(\frac{\pi}{4})_2$	–	–
–	<i>QFT3</i>	–	–
–	<i>Grover3</i>	–	–

Table 17: Set of tested circuits. The tensor product is omitted for brevity.

Loss results					
n	Ideal matrix	Trace	Fidelity	Frobenius	Execution time
2	circuits	$10^{-3}$	$10^{-8}$	$10^{-3}$	< 8s
2	random	$10^{-3}$	$10^{-5}$	$10^{-3}$	< 6s
3	circuits	$10^{-3}$	$10^{-7}$	$10^{-2}$	< 40s
3	random	$10^{-2}$	$10^{-3}$	$10^{-1} \sim 10^{-2}$	< 75s
4	circuits	$10^{-2}$	$10^{-5}$	$10^{-2}$	< 227s
4	random	0.13	$10^{-2}$	0.28	< 222s
5	circuits	$10^{-2}$	$10^{-3}$	0.3	< 21m
5	random	0.19	$10^{-2}$	0.67	< 25m
6	circuits	–	–	0.7	< 2h
6	random	–	–	1.3	< 2h

Table 18: Loss results divided according to the number of qubits and the ideal matrix used.

Ideal matrix	Time taken by our method + Adam opt	Time taken by our method + Nelder Mead opt	Time taken in seconds in [32]	Error from our method + Adam	Error from our method + Nelder Mead opt	Error from [32]	Error from [38] + our method + Adam	Error from [38] + our method + Nelder Mead
CNOT	8s	11 ~ 24s	90	$10^{-3}$	$10^{-15} \sim 10^{-16}$	$7.977 \times 10^{-14}$	$10^{-1} \sim 10^{-3}$	$10^{-15}$
<i>Grover</i> <sub>2</sub>			124			$1.256 \times 10^{-15}$		
XX			20			$6.226 \times 10^{-12}$		
YY			240			$3.223 \times 10^{-15}$		
ZZ			90			$1.363 \times 10^{-17}$		
SWAP			63			$1.839 \times 10^{-13}$		
XZ			150			$3.580 \times 10^{-13}$		
ZX			129			$5.438 \times 10^{-13}$		
ZY			121			$3.188 \times 10^{-12}$		
CNOT(2, 1)			45			$1.058 \times 10^{-13}$		
DCNOT			29			$4.020 \times 10^{-13}$		
XNOR			23			$3.166 \times 10^{-13}$		
iSWAP			183			$3.003 \times 10^{-14}$		
iSWAP			93			$2.037 \times 10^{-13}$		
C-Phase			15			$7.666 \times 10^{-15}$		
XX + YY			124			$1.665 \times 10^{-12}$		
$\sqrt{SWAP}$			97			$1.686 \times 10^{-13}$		
$\sqrt{iSWAP}$			10			$1.106 \times 10^{-13}$		
<i>QFT</i> <sub>2</sub>			31			$3.215 \times 10^{-13}$		
random			6			70		

Table 19: Comparison between different methods, with 2-qubit circuits and Frobenius loss.

Ideal matrix	Time taken by our method + Adam opt	Time taken by our method + Nelder Mead opt	Error from our method + Adam	Error from our method + Nelder Mead opt	Error from [32]	QFAST + KAK [30]	UniversalQ [30]
Toffoli	40s	< 1h	$10^{-2}$	$10^{-10} \sim 10^{-11}$	$4.48 \times 10^{-9}$	$1.5 \times 10^{-6}$	$2.6 \times 10^{-8}$
Fredkin					$1.6 \times 10^{-8}$	$2.2 \times 10^{-6}$	0
<i>Grover</i> <sub>3</sub>					$4.60 \times 10^{-9}$	$8.1 \times 10^{-7}$	0
Peres					$2 \times 10^{-8}$	$6.8 \times 10^{-7}$	$2.1 \times 10^{-8}$
<i>QFT</i> <sub>3</sub>					$3.1 \times 10^{-9}$	$3 \times 10^{-7}$	$3 \times 10^{-8}$

Table 20: Comparison between different methods, with 3-qubit circuits and Frobenius loss.

Ideal matrix	Time taken by our method + Adam opt	Time taken by our method + Nelder Mead opt	Error from our method + Adam	Error from our method + Nelder Mead opt	Error from [32]	QFAST + KAK [30]	UniversalQ [30]
$C_1C_1C_1X$	227s	< 2weeks	$10^{-1}$	$10^{-9}$	$1.97 \times 10^{-8}$	$2.2 \times 10^{-5}$	$1.3 \times 10^{-6}$
<i>Grover</i> <sub>4</sub>		~ 3weeks		$10^{-5}$	$2.12 \times 10^{-9}$	–	–
<i>QFT</i> <sub>4</sub>		< 2weeks		$10^{-9}$	$9.331 \times 10^{-8}$	–	–

Table 21: Comparison between different methods, with 4-qubit circuits and Frobenius loss.

whose solution is:

$$\rho(t) = U\rho(0)U^\dagger \quad (104)$$

From an implementation viewpoint, equation (104) is used to compute the ideal density matrix resulting from any ideal circuit, where  $\rho(0)$  is the amplitude encoding of the input state. The latter is compared to the approximate density matrix produced by the QNN via the trace distance.

Evolution				
n	Ideal matrix	Trace	Fidelity	Frobenius
2	circuits	$10^{-3}$	$10^{-6}$	$10^{-3}$
2	random	$10^{-3}$	$10^{-3}$	$10^{-3}$
3	circuits	$10^{-3}$	$10^{-5}$	$10^{-3}$
3	random	$10^{-2}$	$10^{-2}$	$10^{-3}$
4	circuits	$10^{-3}$	$10^{-5}$	$10^{-2}$
4	random	$10^{-1}$	$10^{-1}$	$10^{-2}$
5	circuits	$10^{-2}$	$10^{-2}$	$10^{-2}$
5	random	0.17	0.16	0.12
6	circuits	—	—	$10^{-2}$
6	random	—	—	0.12

Table 22: The results are divided based on the number of qubits and the ideal matrix used.

In Figure 38, the error on the test set is plotted, when the Adam optimizer is used. The test error is computed as the trace distance between the output state produced by the trained QNN and the ideal state obtained from the ideal circuit that the network should approximate. The plot shows how the fidelity can produce better results with a low number of qubits, while, when the number of qubits increases, the 3 losses behave in a similar manner. For 6 qubits, only the Frobenius results are shown since the algorithm takes days with fidelity and trace.

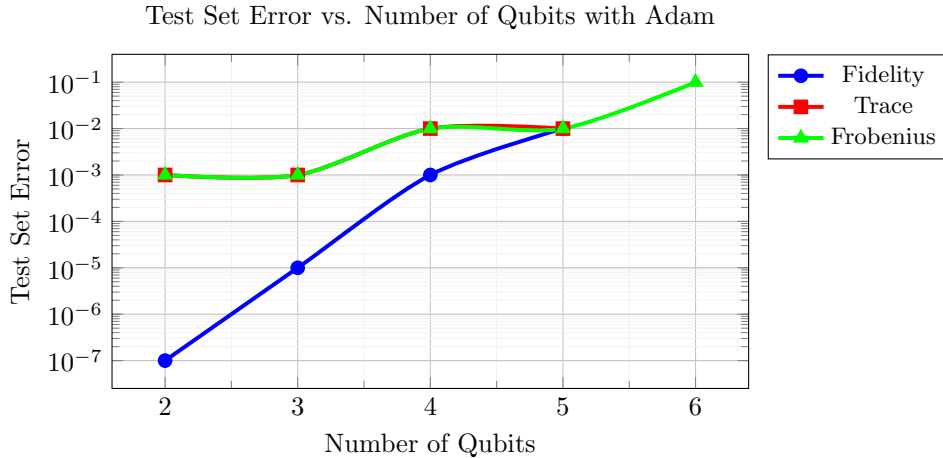


Figure 38: Test set error of the trained QNN with the 3 losses.

In Figure 39, the error on the test set is plotted, concerning experiments in which the Nelder Mead optimizer was used. These results are better than those obtained with Adam, but, from 4 qubits, it takes days to train.

## 7.2 Tests on Real Quantum Devices

In Table 23, the results obtained from tests performed using the IBM Brisbane quantum computer [36] are shown. In particular, the Hellinger distance between the ideal probability distribution and the approximated one produced by the QNN is computed.

Table 24 shows the execution time of a circuit on IBM Brisbane. When the number of qubits is small, the execution times for 1024 and 4096 shots are similar. However, when the number of qubits increases, the time taken with 4096 shots grows significantly.

In Table 25, the fidelity results on IBM quantum computers Brisbane and Fez [36, 37] are presented, when the QNN is trained with Adam to approximate a CNOT gate. In this case, the test set consists of only 10



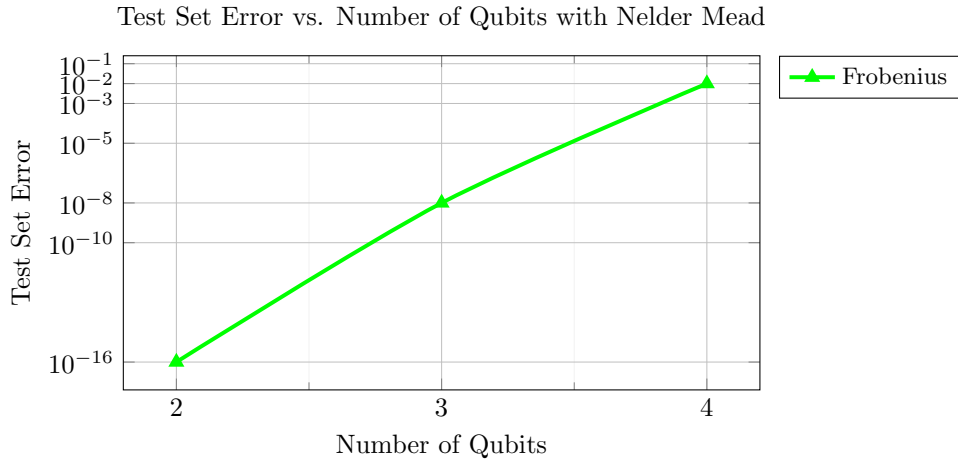


Figure 39: Test set error of the trained QNN with Frobenius loss

n	Hellinger distance
2	$\sim 0.15$
3	$\sim 0.30$
4	$\sim 0.35$

Table 23: Hellinger distance between the ideal probabilities and the one obtained using the IBM Brisbane quantum computer when the VQC is applied to the state  $|0\rangle^{\otimes n}$  with 1024 shots.

n	Time [s] for 1024 shots	Time [s] for 4096 shots
2	$\sim 3$	$\sim 3$
3	$\sim 3$	$\sim 3$
4	$\sim 4$	$\sim 4$
5	$\sim 5 - 6$	$\sim 11$
6	$\sim 11$	$\sim 40 - 45$

Table 24: Time in seconds taken for the execution on using the IBM Brisbane quantum computer when the VQC is applied to the state  $|0\rangle^{\otimes n}$ .

random states, which limits its generalizability. However, it still achieved a good approximation. An interesting observation arises when comparing the compiled circuits of the QNN trained with Adam and Nelder-Mead on real IBM hardware. On IBM Brisbane, the amplitude-encoded input state and Nelder-Mead QNN circuits are compiled into approximately 45 gates, while the Adam-trained circuits are compiled into around 60 gates. This likely occurs because the circuit produced by Nelder-Mead is more accurate, allowing the compiler to better recognize the ideal gate, rather than the sequence of RZ, RY, and CNOT gates used in the scalable algorithm.

Device	Time [s] for 1024 shots	Hellinger distance
IBM Brisbane	$\sim 3$	$\sim 0.06$
IBM Fez	$\sim 6$	$\sim 0.07$

Table 25: Results of an approximated CNOT on real IBM hardware.

### 7.3 Insights on loss functions

From an application viewpoint, the interpretations of the loss functions vary. When using the Frobenius loss, the  $\|A\|_F$  compares the two matrices algebraically, allowing it to find the ideal matrix. On the other hand, when using the trace distance or fidelity losses, these metrics compare the density matrices of the output states. Therefore, there may be scenarios where the QNN produces the correct output probability distribution when measured, but the approximated matrix differs from the ideal one. For instance, in Table 17, the circuit  $C_0^1 C_1^0 RY(\frac{\pi}{4})$  for 3 qubits shows discrepancies in some entries of the approximated matrix compared to the ideal one:

Ideal unitary matrix  $U$ :

$$\begin{bmatrix} 1+0j & 0j & 0j & 0j & 0j & 0j & 0j & 0j \\ 0j & 1+0j & 0j & 0j & 0j & 0j & 0j & 0j \\ 0j & 0j & 1+0j & 0j & 0j & 0j & 0j & 0j \\ 0j & 0j & 0j & 1+0j & 0j & 0j & 0j & 0j \\ 0j & 0j & 0j & 0j & \mathbf{0.92388+0j} & \mathbf{-0.38268-0j} & 0j & 0j \\ 0j & 0j & 0j & 0j & \mathbf{0.38268+0j} & \mathbf{0.92388+0j} & 0j & 0j \\ 0j & 0j & 0j & 0j & 0j & 0j & 1+0j & 0j \\ 0j & 0j & 0j & 0j & 0j & 0j & 0j & 1+0j \end{bmatrix}$$

Approximated unitary matrix  $U$  (Fidelity/Trace):

$$\begin{bmatrix} 1-10^{-5}j & 10^{-5}+10^{-5}j & 10^{-5}+10^{-5}j & 10^{-5}+0j & 10^{-5}j & 10^{-5}-10^{-5}j & 10^{-5}+0j & 10^{-5}+10^{-5}j \\ 10^{-5}+10^{-5}j & 1+10^{-5}j & 10^{-5}+10^{-5}j & 10^{-5}+10^{-5}j & -10^{-5}-10^{-5}j & 10^{-5}+0j & 10^{-5}+0j & 10^{-5}+10^{-5}j \\ -10^{-5}+10^{-5}j & -10^{-5}+10^{-5}j & 1-10^{-5}j & -10^{-5}-10^{-5}j & -10^{-4}+10^{-5}j & -10^{-4}-10^{-4}j & 0 & 10^{-5}-10^{-5}j \\ -10^{-5}+0j & -10^{-5}+10^{-5}j & 10^{-5}-10^{-5}j & 1+10^{-5}j & 10^{-5}+10^{-4}j & -10^{-5}-10^{-5}j & 10^{-5}-10^{-5}j & 10^{-5}-0j \\ 10^{-5}+10^{-5}j & 10^{-5}-10^{-5}j & -10^{-5}+10^{-4}j & -10^{-5}+10^{-4}j & \mathbf{0.70722-10^{-4}j} & \mathbf{-0.70699+10^{-4}j} & -0+10^{-4}j & -10^{-4}j \\ -10^{-5}-10^{-5}j & 10^{-5}-10^{-5}j & 10^{-4}-10^{-4}j & -10^{-5}+10^{-4}j & \mathbf{0.70699+10^{-4}j} & \mathbf{0.70722+10^{-4}j} & 10^{-5}-10^{-4}j & -10^{-5}-10^{-4}j \\ 10^{-5}+0j & 10^{-5}+0j & 0 & -10^{-5}-10^{-5}j & 0+10^{-5}j & -10^{-5}-10^{-4}j & 1+0j & 0+10^{-5}j \\ -10^{-5}+10^{-5}j & -10^{-5}+10^{-5}j & -10^{-5}-10^{-5}j & -10^{-5}+0j & 10^{-5}-10^{-4}j & 10^{-5}+0j & 10^{-5}j & 1-0j \end{bmatrix}$$

On the other hand, when the Frobenius norm is used as loss function, the neural network can find a correct approximation of the unitary matrices. For instance, the approximated unitary matrix for  $C_0^1 C_1^0 RY(\frac{\pi}{4})$  will result:

$$\begin{bmatrix} 0.99989+0.01376j & 10^{-5}-0j & -10^{-3}+10^{-3}j & 10^{-5}j & -10^{-4}+10^{-5}j & 10^{-5}-10^{-5}j & -10^{-4}-10^{-4}j & 10^{-4}-10^{-5}j \\ -10^{-5}-0j & 0.99999-0.00215j & -10^{-5}+0j & 10^{-3}-10^{-3}j & 10^{-5}-10^{-5}j & 10^{-4}+10^{-4}j & 10^{-5}-10^{-4}j & -10^{-4}-10^{-4}j \\ 10^{-3}+10^{-3}j & 10^{-5}+0j & 0.9999-0.01262j & -10^{-5}j & 10^{-4}+10^{-4}j & -10^{-4}+0j & 10^{-4}-10^{-4}j & 10^{-4}+10^{-4}j \\ 10^{-5}j & -10^{-3}-10^{-3}j & -10^{-5}j & 0.99999+10^{-4}j & -10^{-4}+10^{-5}j & 10^{-4}+10^{-4}j & 10^{-5}+10^{-5}j & 10^{-4}+10^{-4}j \\ 10^{-4}+10^{-5}j & 10^{-5}-10^{-5}j & -10^{-4}+10^{-4}j & 10^{-4}-10^{-4}j & \mathbf{0.92386+0.00185j} & \mathbf{-0.38273-10^{-5}j} & 10^{-4}+10^{-5}j & -10^{-4}+10^{-4}j \\ -10^{-5}-10^{-5}j & -10^{-4}+10^{-4}j & 10^{-5}+10^{-4}j & -10^{-4}+10^{-4}j & \mathbf{0.38273+10^{-5}j} & \mathbf{0.92386+10^{-5}j} & -10^{-4}-10^{-5}j & 10^{-4}+10^{-5}j \\ 10^{-5}-10^{-4}j & -10^{-5}-10^{-4}j & -10^{-4}-10^{-4}j & -10^{-5}+10^{-5}j & -10^{-5}-10^{-4}j & 10^{-4}-10^{-5}j & 1-10^{-3}j & 10^{-5}+10^{-4}j \\ -10^{-4}-10^{-5}j & 10^{-4}-10^{-4}j & -10^{-4}+10^{-4}j & -10^{-4}+10^{-4}j & 10^{-4}+10^{-5}j & -10^{-4}-10^{-4}j & -10^{-5}+10^{-4}j & 1-10^{-5}j \end{bmatrix}$$

For practical applications focused solely on output probability distribution given an input state to the circuit, fidelity and trace can be employed, up to 5 qubits. However, if precise matrix representation is crucial, the Frobenius norm stands as the only suitable loss function, thereby mitigating the risk of obtaining incorrect values.

Another important aspect is achieved using fidelity or trace distance. Except for certain specific cases, such as  $C_0^1 C_1^0 RY(\frac{\pi}{4})$ , it has been demonstrated that this algorithm can also be used for state preparation. This is achieved because, when the algorithm is trained using these 2 loss functions, 1000 random states are used. Then, if the approximated unitary matrix is correct, it means that the QNN can also successfully perform approximate state preparation.

## 8 Conclusions

In this work, a scalable QNN is proposed to approximate any unitary operator through the Standard Recursive Block Basis (SRBB) decomposition, which is capable of representing unitary matrices in parametric form by exploiting Lie algebras. Particular attention is paid to the relationship between  $SU(2^n)$  and  $U(2^n)$  Lie groups, given that the algorithm works only with special unitary matrices; by exploiting a phase correction approach (unitary scaling), it is possible to generalize the approximation technique to generic unitary matrices. Firstly, the  $n = 2$  case is found to be a peculiar scenario outside the scalability scheme proposed in the literature, which concerns only the ordering and grouping of the elements of the algebra (therefore the overall structure of the variational circuit), but not the possible and theoretically proposed simplifications of CNOTs. The reason for this anomaly lies in the properties of the matrix algebra under permutation via 2-cycles (or transpositions) and gives rise to specific simplifications for this case. Secondly, a novel CNOT-reduced scaling scheme is discovered and implemented from  $n \geq 3$ , leading to new gate count formulas; it makes use of a Gray-Code-type ordering and the properties of the binary representation to find and define the scalable scheme of the simplifications of CNOT gates. Indeed, in the 2-qubit case, other simplifications that cannot be incorporated into this new scalable scheme occur to reach the optimal number of CNOTs. For  $n \geq 6$ , the fraction of simplified gates resulting from this new scalable scheme is not yet suitable for practical use of the QNN, but it is a solid starting point to reach the optimal depth in the scalable SRBB-based synthesis algorithm, leveraging the link between VQCs and parameterized unitary operators. Thirdly, with the aim of developing a Python library useful for verifying the algebraic properties that guarantee the effectiveness of the approximation as for future developments, a revised version of the recursive algorithm that constructs the SRBB is derived, thus simplifying the management and manipulation of high cardinality algebras (exponential growth). The revision concerns the particular ordering, only partially increasing, of the matrix elements for the second and third methods of construction of the algebra; this detail allows to clearly match the properties under permutation to the algebra sub-groupings, thus structuring scalability from an implementation perspective.

The scalable CNOT-reduced VQC has been implemented using the PennyLane library and the tests have been performed using the simulator provided by the same library; some simple tests with 2 qubits are performed on IBM real hardware to assess the algorithm's usability. The QNN has been tested for different numbers of qubits, from 2 to 6, and with only one single layer of approximation; first with predefined circuits designed by us and then with dense random  $SU(2^n)$  matrices.

The network has been trained using two different optimizers, Adam and Nelder Mead, while the performance has been evaluated with different loss functions, like trace distance, fidelity, and Frobenius norm, each with a different application based on the specific metric criterion inside their definition. In general, the algorithm achieved a low value of the loss up to 5 qubits. As expected, the precision decreases when the number of qubits increases, meaning probably a too complex parametric landscape with additional local minima. Furthermore, the performance worsens when using random matrices, meaning the simpler approximation of sparse matrices or matrices with a specific pattern. Furthermore, while the Nelder-Mead optimizer can achieve a high level of approximation, the Adam optimizer results in worse performance but requires significantly less execution time. Moreover, the trained network has been tested on real IBM hardware to approximate a CNOT gate, achieving a high level of fidelity as measured by the Hellinger distance.

In the future, the proposed framework could be tested for both state preparation and classification tasks. In state preparation, the objective is to achieve a specific quantum state, and the proposed VQC could generate an approximated matrix capable of reaching each desired state. Similarly, in classification tasks, this framework could be used to discover the appropriate unitary matrix to maximize the probability of finding the correct classes. Besides, it would be interesting to use this algorithm in Hamiltonian simulation with the aim to automate the design of a versatile simulator of machine-learned quantum evolutions. As the number of qubits increases, the depth and the number of gates in the QNN increase rapidly, leading to overly deep circuits and significantly longer training times. Therefore, an important improvement would be to find a way to reduce the number of rotations in the VQC, still maintaining the scalability.

## Acknowledgment

We thank Rohit S. Sarkar and Bibhas Adhikari for helpful discussions regarding the mathematical aspects of their algorithm on the SRBB. Giacomo Belli and Michele Amoretti acknowledge financial support from the European Union - NextGenerationEU, PNRR MUR project PE0000023-NQSTI. This research benefits from the High Performance Computing facility of the University of Parma, Italy (HPC.unipr.it) and also from IBM Quantum Credits awarded to Michele Amoretti - project Crosstalk-aware Quantum Multiprogramming.

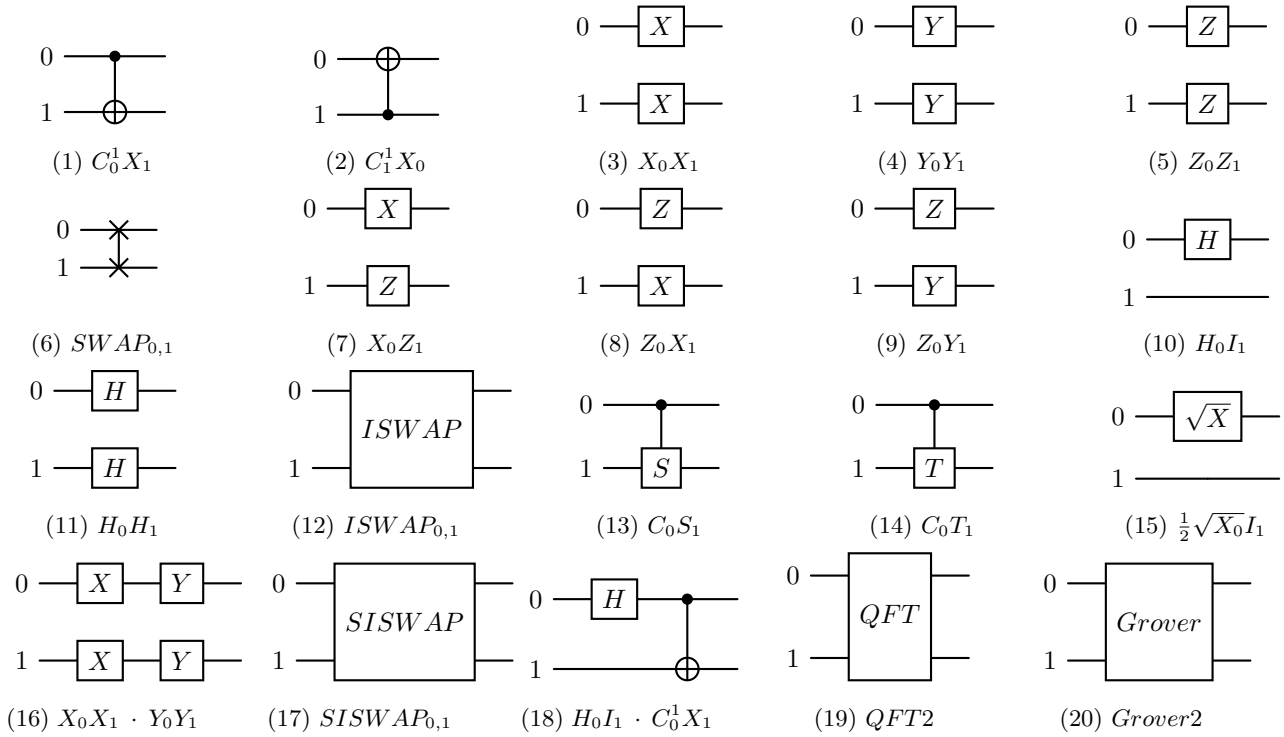
## References

- [1] Maria Schuld and Francesco Petruccione. *Supervised learning with quantum computers*, volume 17. Springer, 2018.
- [2] Marco Cerezo, Andrew Arrasmith, Ryan Babbush, Simon C Benjamin, Suguru Endo, Keisuke Fujii, Jarrod R McClean, Kosuke Mitarai, Xiao Yuan, Lukasz Cincio, et al. Variational quantum algorithms. *Nature Reviews Physics*, 3(9):625–644, 2021.
- [3] Vedran Dunjko and Peter Wittek. A non-review of quantum machine learning: trends and explorations. *Quantum Views*, 4:32, 2020.
- [4] Marcello Benedetti, Erika Lloyd, Stefan Sack, and Mattia Fiorentini. Parameterized quantum circuits as machine learning models. *Quantum Science and Technology*, 4(4):043001, 2019.
- [5] Vivek V Shende, Igor L Markov, and Stephen S Bullock. Minimal universal two-qubit controlled-not-based circuits. *Physical Review A—Atomic, Molecular, and Optical Physics*, 69(6):062321, 2004.
- [6] Vivek V Shende, Stephen S Bullock, and Igor L Markov. Synthesis of quantum logic circuits. In *Proceedings of the 2005 Asia and South Pacific Design Automation Conference*, pages 272–275, 2005.
- [7] Ville Bergholm, Juha J Vartiainen, Mikko Möttönen, and Martti M Salomaa. Quantum circuits with uniformly controlled one-qubit gates. *Physical Review A—Atomic, Molecular, and Optical Physics*, 71(5):052330, 2005.
- [8] Mikko Möttönen and Juha J Vartiainen. Decompositions of general quantum gates. *Trends in quantum computing research*, page 149, 2006.
- [9] Farrokh Vatan and Colin Williams. Optimal quantum circuits for general two-qubit gates. *Physical Review A—Atomic, Molecular, and Optical Physics*, 69(3):032315, 2004.
- [10] Juha J Vartiainen, Mikko Möttönen, and Martti M Salomaa. Efficient decomposition of quantum gates. *Physical review letters*, 92(17):177902, 2004.
- [11] Vadym Kliuchnikov, Alex Bocharov, Martin Roetteler, and Jon Yard. A framework for approximating qubit unitaries. *arXiv preprint arXiv:1510.03888*, 2015.
- [12] Neil J Ross. Algebraic and logical methods in quantum computation. *arXiv preprint arXiv:1510.02198*, 2015.
- [13] Vadym Kliuchnikov, Dmitri Maslov, and Michele Mosca. Fast and efficient exact synthesis of single qubit unitaries generated by clifford and t gates. *arXiv preprint arXiv:1206.5236*, 2012.
- [14] Stephen S Bullock and Igor L Markov. Smaller circuits for arbitrary n-qubit diagonal computations. *arXiv preprint quant-ph/0303039*, 2003.
- [15] Jiaqing Jiang, Xiaoming Sun, Shang-Hua Teng, Bujiao Wu, Kewen Wu, and Jialin Zhang. Optimal space-depth trade-off of cnot circuits in quantum logic synthesis. In *Proceedings of the Fourteenth Annual ACM-SIAM Symposium on Discrete Algorithms*, pages 213–229. SIAM, 2020.
- [16] Yifan Kang and Henry Ma. Cnot-optimal circuit synthesis. 2023.
- [17] Mikko Möttönen, Juha J Vartiainen, Ville Bergholm, and Martti M Salomaa. Quantum circuits for general multiqubit gates. *Physical review letters*, 93(13):130502, 2004.
- [18] Anna M Krol, Aritra Sarkar, Imran Ashraf, Zaid Al-Ars, and Koen Bertels. Efficient decomposition of unitary matrices in quantum circuit compilers. *Applied Sciences*, 12(2):759, 2022.
- [19] Christopher M Dawson and Michael A Nielsen. The solovay-kitaev algorithm. *arXiv preprint quant-ph/0505030*, 2005.
- [20] Adriano Barenco, Charles H Bennett, Richard Cleve, David P DiVincenzo, Norman Margolus, Peter Shor, Tycho Sleator, John A Smolin, and Harald Weinfurter. Elementary gates for quantum computation. *Physical review A*, 52(5):3457, 1995.

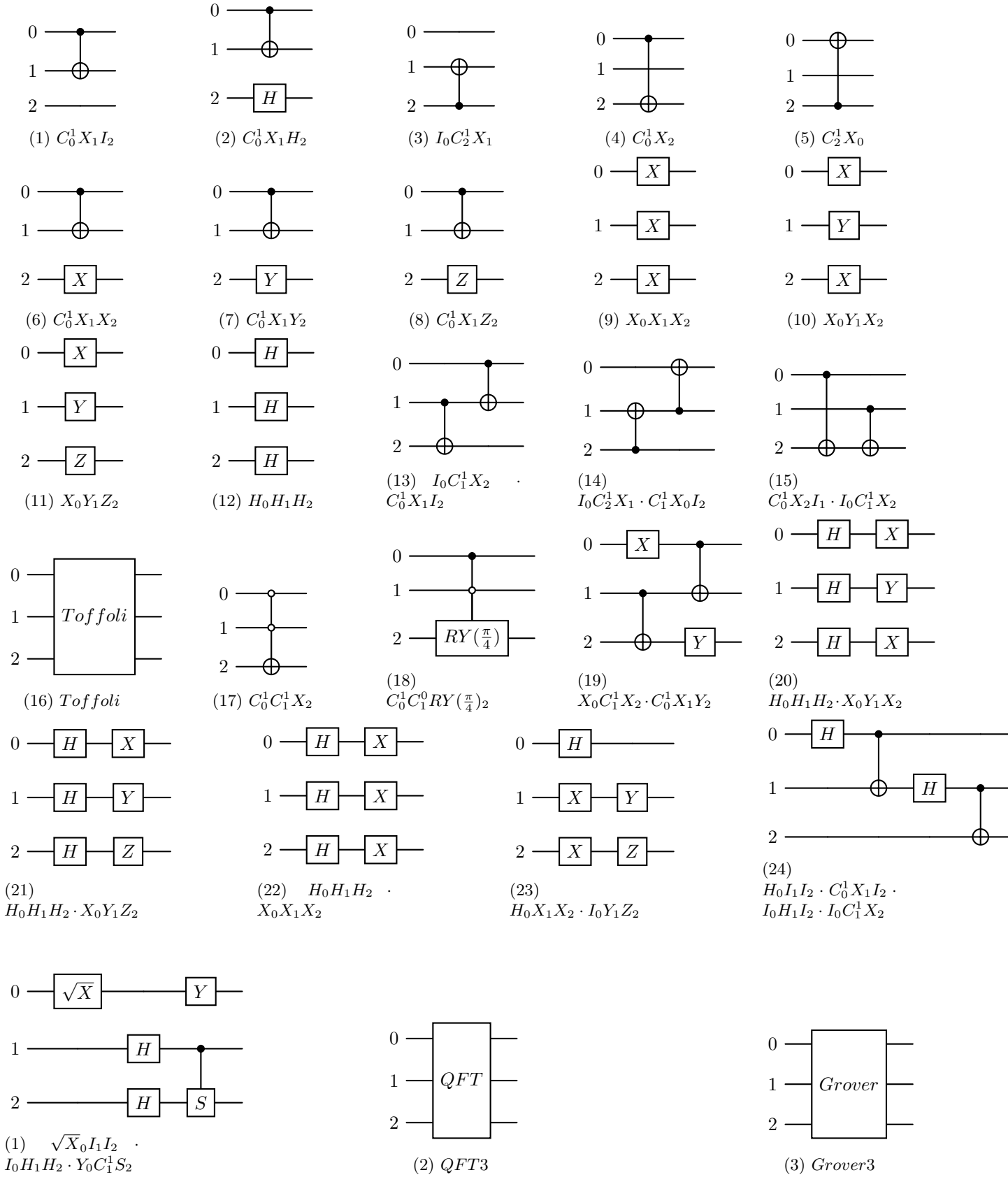
- [21] Tien Trung Pham, Rodney Van Meter, and Dominic Horsman. Optimization of the solovay-kitaev algorithm. *Physical Review A—Atomic, Molecular, and Optical Physics*, 87(5):052332, 2013.
- [22] Y Zhiyenbayev, VM Akulin, and Aikaterini Mandilara. Quantum compiling with diffusive sets of gates. *Physical Review A*, 98(1):012325, 2018.
- [23] Vadym Kliuchnikov, Dmitri Maslov, and Michele Mosca. Asymptotically optimal approximation of single qubit unitaries by clifford and t circuits using a constant number of ancillary qubits. *Physical review letters*, 110(19):190502, 2013.
- [24] Peter Selinger. Efficient clifford+ t approximation of single-qubit operators. *arXiv preprint arXiv:1212.6253*, 2012.
- [25] Neil J Ross. Optimal ancilla-free pauli+ v approximation of z-rotations. *arXiv preprint arXiv:1409.4355*, 2014.
- [26] Vadym Kliuchnikov, Dmitri Maslov, and Michele Mosca. Practical approximation of single-qubit unitaries by single-qubit quantum clifford and t circuits. *IEEE Transactions on Computers*, 65(1):161–172, 2015.
- [27] Neil J Ross and Peter Selinger. Optimal ancilla-free clifford+ t approximation of z-rotations. *Quantum Inf. Comput.*, 16(11&12):901–953, 2016.
- [28] Liam Madden and Andrea Simonetto. Best approximate quantum compiling problems. *ACM Transactions on Quantum Computing*, 3(2):1–29, 2022.
- [29] Liam Madden, Albert Akhriev, and Andrea Simonetto. Sketching the best approximate quantum compiling problem. In *2022 IEEE International Conference on Quantum Computing and Engineering (QCE)*, pages 492–502. IEEE, 2022.
- [30] Ed Younis, Koushik Sen, Katherine Yelick, and Costin Iancu. Qfast: Quantum synthesis using a hierarchical continuous circuit space. *arXiv preprint arXiv:2003.04462*, 2020.
- [31] Ed Younis, Koushik Sen, Katherine Yelick, and Costin Iancu. Qfast: Conflating search and numerical optimization for scalable quantum circuit synthesis. In *2021 IEEE International Conference on Quantum Computing and Engineering (QCE)*, pages 232–243. IEEE, 2021.
- [32] Rohit Sarma Sarkar and Bibhas Adhikari. Scalable quantum circuits for n-qubit unitary matrices. In *2023 IEEE International Conference on Quantum Computing and Engineering (QCE)*, volume 1, pages 1078–1088. IEEE, 2023.
- [33] Rohit Sarma Sarkar and Bibhas Adhikari. A quantum neural network framework for scalable quantum circuit approximation of unitary matrices. *arXiv preprint arXiv:2405.00012*, 2024.
- [34] Alexander A Kirillov. *An introduction to Lie groups and Lie algebras*, volume 113. Cambridge University Press, 2008.
- [35] Ville Bergholm, Josh Izaac, Maria Schuld, Christian Gogolin, Shahnawaz Ahmed, Vishnu Ajith, M Sohaib Alam, Guillermo Alonso-Linaje, B AkashNarayanan, Ali Asadi, et al. PennyLane: Automatic differentiation of hybrid quantum-classical computations. *arXiv preprint arXiv:1811.04968*, 2018.
- [36] IBM Quantum. Ibm brisbane quantum system. [https://quantum.ibm.com/services/resources?system=ibm\\_brisbane](https://quantum.ibm.com/services/resources?system=ibm_brisbane), 2024. Accessed: 2024-11-14.
- [37] IBM Quantum. Ibm fez quantum system. [https://quantum.ibm.com/services/resources?system=ibm\\_fez](https://quantum.ibm.com/services/resources?system=ibm_fez), 2024. Accessed: 2024-11-14.
- [38] Guifre Vidal and Christopher M Dawson. Universal quantum circuit for two-qubit transformations with three controlled-not gates. *Physical Review A*, 69(1):010301, 2004.

# A Tested Circuits

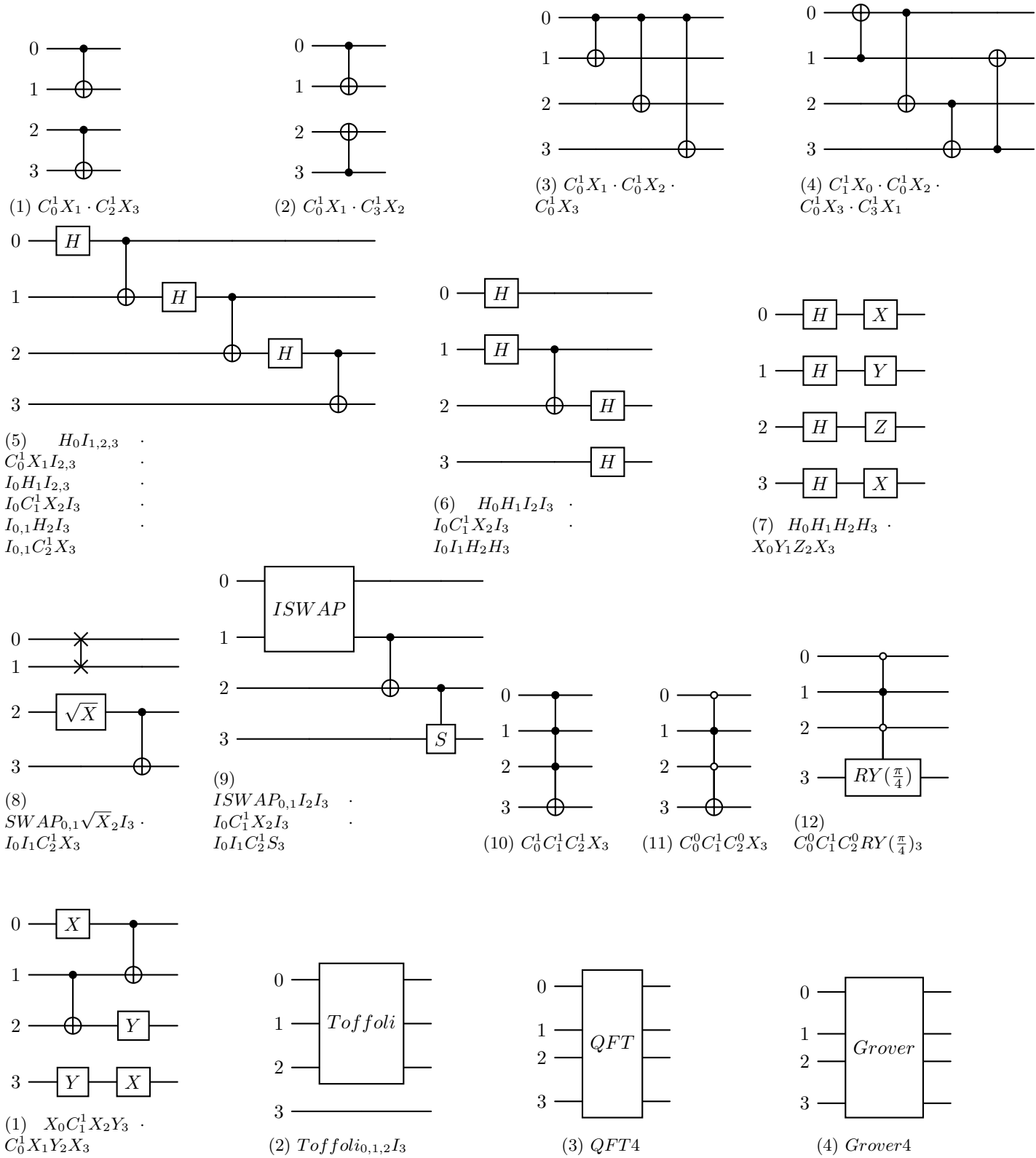
## A.1 List of tested circuits for $n = 2$



## A.2 List of tested circuits for $n = 3$

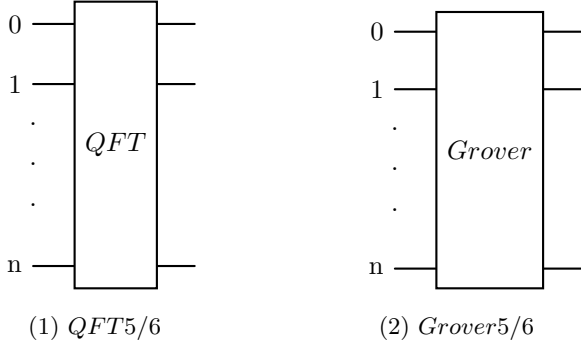


### A.3 List of tested circuits for $n = 4$





## A.4 List of tested circuits for $n = 5, 6$



## B Example of resulting matrices

### B.1 QFT2

Ideal  $QFT_2$ :

$$\begin{bmatrix} 0.5 + 0j & 0.5 + 0j & 0.5 + 0j & 0.5 + 0j \\ 0.5 + 0j & 0 + 0.5j & -0.5 + 0j & 0 - 0.5j \\ 0.5 + 0j & -0.5 + 0j & 0.5 + 0j & -0.5 + 0j \\ 0.5 + 0j & 0 - 0.5j & -0.5 + 0j & 0 + 0.5j \end{bmatrix}$$

Approximated  $QFT_2$  with Frobenius loss:

$$\begin{bmatrix} 0.5001 + 0.00124j & 0.50034 + 0.00034j & 0.49992 - 0.00065j & 0.49964 + 0.00004j \\ 0.49992 + 0.00058j & 0.00006 + 0.49964j & -0.5001 + 0.00131j & -0.00036 - 0.50034j \\ 0.49999 + 0.00211j & -0.49989 - 0.00065j & 0.49999 - 0.00071j & -0.50012 - 0.00053j \\ 0.49999 + 0.00074j & -0.00046 - 0.50012j & -0.49999 + 0.00209j & 0.00058 + 0.49989j \end{bmatrix}$$

Approximated  $QFT_2$  with fidelity loss:

$$\begin{bmatrix} 0.5 + 10^{-5}j & 0.5 + 0j & 0.5 + 0j & 0.5 + 10^{-5}j \\ 0.50001 + 0j & -10^{-5} + 0.5j & -0.49999 + 0j & -0 - 0.5j \\ 0.49999 + 0j & -0.5 - 10^{-5}j & 0.5 + 0j & -0.5 + 10^{-5}j \\ 0.5 + 0j & -0 - 0.5j & -0.50001 + 0j & -0 + 0.5j \end{bmatrix}$$

Approximated  $QFT_2$  with trace distance loss:

$$\begin{bmatrix} 0.49956 + 0.00033j & 0.49994 + 0.00015j & 0.50081 - 0.00151j & 0.49968 - 0.00084j \\ 0.50113 + 0.00061j & -0.00076 + 0.50015j & -0.4997 - 0.00017j & -0.00041 - 0.49902j \\ 0.49954 - 0.00048j & -0.49995 - 0.00091j & 0.50009 - 0.00025j & -0.50042 + 0.00115j \\ 0.49976 + 0.00112j & 0.00125 - 0.49995j & -0.4994 + 0.00005j & 0.00061 + 0.50088j \end{bmatrix}$$

### B.2 Frobenius loss random matrix

Ideal random matrix:

$$\begin{bmatrix} -0.29584 + 0.229j & -0.04615 + 0.15104j & -0.17965 - 0.05721j & 0.88599 + 0.1207j \\ 0.60385 - 0.21653j & -0.1687 - 0.347j & 0.49773 + 0.1392j & 0.40585 + 0.08832j \\ 0.08131 - 0.03817j & -0.77354 - 0.04134j & -0.46739 + 0.41132j & -0.06164 - 0.02057j \\ -0.56843 + 0.34255j & -0.29486 - 0.37306j & 0.53784 + 0.14295j & -0.09534 - 0.12097j \end{bmatrix}$$

Approximated random matrix:

$$\begin{bmatrix} -0.29592 + 0.22861j & -0.04634 + 0.15084j & -0.17981 - 0.05736j & 0.8859 + 0.12175j \\ 0.60394 - 0.21609j & -0.16906 - 0.34673j & 0.49789 + 0.13962j & 0.40561 + 0.08859j \\ 0.0818 - 0.03893j & -0.7735 - 0.03856j & -0.46708 + 0.41182j & -0.06188 - 0.02029j \\ -0.56897 + 0.34176j & -0.29565 - 0.37295j & 0.53712 + 0.144j & -0.09522 - 0.12115j \end{bmatrix}$$

### B.3 Fidelity loss random matrix

Ideal random matrix:

$$\begin{bmatrix} -0.16928 - 0.26816j & 0.76479 - 0.14228j & -0.07799 + 0.53619j & -0.02627 + 0.00328j \\ -0.01908 + 0.21297j & -0.04915 - 0.38823j & -0.65553 - 0.00019j & 0.58473 + 0.17177j \\ -0.07927 + 0.06076j & 0.33226 - 0.12021j & -0.03272 - 0.4948j & 0.11523 - 0.77846j \\ -0.34491 - 0.85134j & -0.32301 - 0.11193j & -0.12928 - 0.11863j & 0.0702 - 0.06068j \end{bmatrix}$$

Approximated random matrix:

$$\begin{bmatrix} -0.2166 - 0.20012j & 0.77381 - 0.12037j & -0.09693 + 0.53626j & -0.05025 - 0.0164j \\ -0.11102 + 0.17193j & -0.08947 - 0.37078j & -0.66499 + 0.00496j & 0.58424 + 0.17046j \\ -0.08118 + 0.07857j & 0.31621 - 0.1384j & -0.02304 - 0.50683j & 0.12519 - 0.77137j \\ -0.3595 - 0.8539j & -0.32064 - 0.1389j & -0.04184 - 0.04047j & 0.03412 - 0.12229j \end{bmatrix}$$

### B.4 Trace distance random matrix

Ideal random matrix:

$$\begin{bmatrix} -0.54567 - 0.69544j & 0.00628 + 0.03428j & 0.33735 - 0.26454j & 0.05243 - 0.17569j \\ -0.43366 - 0.02622j & -0.03354 - 0.02404j & 0.04403 + 0.8673j & -0.15501 + 0.17713j \\ -0.15789 + 0.01538j & -0.42342 - 0.18806j & -0.21585 + 0.02265j & 0.82598 + 0.17559j \\ 0.06695 - 0.01476j & -0.8375 - 0.28464j & 0.0952 - 0.07683j & -0.43968 - 0.06774j \end{bmatrix}$$

Approximated random matrix:

$$\begin{bmatrix} -0.54806 - 0.69461j & 0.02581 + 0.02394j & 0.33803 - 0.26225j & 0.05547 - 0.17259j \\ -0.43273 - 0.02469j & -0.01735 - 0.02715j & 0.04159 + 0.86756j & -0.1555 + 0.18033j \\ -0.15529 + 0.00533j & -0.42411 - 0.1861j & -0.21809 + 0.03073j & 0.82615 + 0.17414j \\ 0.06245 - 0.03515j & -0.83762 - 0.28567j & 0.09951 - 0.06444j & -0.43896 - 0.07j \end{bmatrix}$$